IZMIR UNIVERSITY OF ECONOMICS
FACULTY OF ENGINEERING
AEROSPACE ENGINEERING

Autonomous optical and inertial navigation of solar-sail propelled CubeSat class spacecraft during targeting missions to asteroids and minor moons

Authors: Hazal Karaaliler
Yağız Akan
Deniz Lena Demirbağ
İlayda Macit

Supervisor: Dr. Fabrizio Pinto

https://doi.org/10.5281/zenodo.7032367

We would like to thank our supervisor Dr. Fabrizio Pinto for his guidance throughout our project. Also, we gratefully acknowledge Mr. Jon Giorgini/JPL, Navigation & Mission Design Section, Dr. Marc Rayman/JPL, Chief Engineer for Mission Operations and Science, and Dr. Shyam Bhaskaran/JPL, Outer Planet Navigation Group Supervisor for information regarding the state of the art in autonomous navigation.

Contents

Autonomous optical and inertial navigation of solar-sail propelled CubeSat class spacecraft during targeting missions to asteroids and minor moons

Hazal Karaaliler[1], Yağız Akan[1], Deniz Lena Demirbağ[1], İlayda Macit[1]

August 29, 2022

1 Abstract

Traveling through deep space is still an area that needs to be improved and regenerated considering the number of successful interplanetary missions. Furthermore, traveling through distant asteroids or planetary systems requires innovative technologies in propulsion, tracking, maneuvering, etc. Since the spacecraft voyages through deep space, it cannot completely count on ground-based navigation systems and needs to have an on-board, autonomous navigation system to steer itself. Another solid reason to develop an autonomous navigation technology is the overuse of the Deep Space Network which has started to ripen and thus may not be able to deliver as before. Likewise, the propulsion technology needs to be reformed according to the needs of missions. Solar-sailing has branched out in that sense, providing a potential to improve space travel without carrying any engine or conventional propulsion system but utilizing radiation pressure produced by the Sun. Although there are some pioneer missions implementing these technologies, there is not any application that has combined autonomous navigation and Solar-sailing. And, this project intends to prove the concept of a Cube-Sat class, Solar-sail propelled spacecraft with an on-board autonomous optical and inertial navigation system during targeting missions to asteroids and minor moons by modeling a synthetic stellar environment on Mathematica to operate navigation procedures, eventually to estimate the spacecraft's current position.

List of Symbols, Definitions and Abbreviations

accelerometer An accelerometer is a tool that measures proper acceleration. Proper acceleration is the rate of change of velocity of a body in its own instantaneous rest frame. 7, 8, 16

albedo Albedo ('whiteness') is the measure of the diffuse reflection of solar radiation out of the total solar radiation and measured on a scale from 0, corresponding to a black body that absorbs all incident radiation, to 1, corresponding to a body that reflects all incident radiation. 15, 16

angular velocity (ω) Angular velocity or rotational velocity, also known as angular frequency vector, is a vector measure of rotation rate, that refers to how fast an object rotates or revolves relative to another point. 7, 8

aphelion (Q) Aphelion is the point in the orbit of a planet, comet, or other body most distant from the Sun. It is equivalent to the apoapsis of a general orbit. 52

Apollo The Apollo program was the third United States human spaceflight program carried out by the National Aeronautics and Space Administration (NASA), which accomplished landing the first humans on the Moon from 1969 to 1972. 16

apparent magnitude Apparent magnitude (m) is a measure of the brightness of a star or other astronomical object observed from Earth. An object's apparent magnitude depends on its intrinsic luminosity, its distance from Earth, and any extinction of the object's light caused by interstellar dust along the line of sight to the observer. 26, 28

aragument of perihelion (ω) The argument of periapsis/perhelion is the angle from the body's ascending node to its periapsis, measured in the direction of motion. 52

ASTAP Astrometric Stacking Program, astrometric solver and FITS image viewer. 25, 26, 28, 43, 45–47, 59, 60, 63, 64, 87

AU A unit of length effectively equal to the average distance between Earth and the Sun. 24

Auto-Nav Autonomous Onboard Optical Navigation. 10, 12, 13, 85, 87

beacon A beacon is an intentionally conspicuous device designed to attract attention to a specific location. 7, 18–20

B-V color index In astronomy, the color index is a simple numerical expression that determines the color of an object, which in the case of a star gives its temperature. The smaller the color index, the more blue (or hotter) the object is. Conversely, the larger the color index, the more red (or cooler) the object is. 28

C Capacitance is the ratio of the amount of electric charge stored on a conductor to a difference in electric potential. 8

capacitor A capacitor is a device that stores electrical energy in an electric field. It is a passive electronic component with two terminals. 8

CCD A charge-coupled device is an integrated circuit containing an array of linked, or coupled, capacitors. Under the control of an external circuit, each capacitor can transfer its electric charge to a neighboring capacitor. 11, 15, 29, 31, 41, 56

coma The coma is the nebulous envelope around the nucleus of a comet, formed when the comet passes close to the Sun on its highly elliptical orbit; as the comet warms, parts of it sublimate. This gives a comet a "fuzzy" appearance when viewed in telescopes and distinguishes it from stars. 15, 16

covariance It is a measure of the joint variability of two random variables. The sign of the covariance shows the tendency in the linear relationship between the variables. 11–13

CubeSat A CubeSat (U-class spacecraft) is a type of miniaturized satellite for space research that is made up of multiple cubic modules. 10, 85

DS1 Deep Space 1 was a NASA technology demonstration spacecraft which flew by an asteroid and a comet. 15, 16, 85

DSLR A digital single-lens reflex camera (digital SLR or DSLR) is a digital camera that combines the optics and the mechanisms of a single-lens reflex camera with a digital imaging sensor. 31

DSN The Deep Space Network is a worldwide network of spacecraft communication ground segment facilities, located in the United States, Spain, and Australia, that supports interplanetary spacecraft missions. 7, 9, 10, 87

eccentricity (e) The orbital eccentricity of an astronomical object is a dimensionless parameter that determines the amount by which its orbit around another body deviates from a perfect circle. A value of 0 is a circular orbit, values between 0 and 1 form an elliptic orbit, 1 is a parabolic escape orbit, and greater than 1 is a hyperbola. 52

ephemeris In astronomy and celestial navigation, an ephemeris is a book with tables that gives the trajectory of naturally occurring astronomical objects as well as artificial satellites in the sky, i.e., the position (and possibly velocity) over time. 7, 9, 10, 18, 20, 67, 68, 70

focal length The focal length of an optical system is a measure of how strongly the system converges or diverges light; it is the inverse of the system's optical power. 20

FOSS Free and open-source software (FOSS) is software that is both free software and open-source software where anyone is freely licensed to use, copy, study, and change the software in any way, and the source code is openly shared so that people are encouraged to voluntarily improve the design of the software. 18

FOV Field of view is the maximum area of a sample that a camera can image. 17, 18, 20, 45

G The gravitational constant, G, is an empirical physical constant involved in the calculation of gravitational effects in Sir Isaac Newton's law of universal gravitation and in Albert Einstein's general theory of relativity. 24

GEO A geostationary orbit is a circular geosynchronous orbit 35,786 kilometres in altitude above Earth's Equator and following the direction of Earth's rotation. 7

GMAT The General Mission Analysis Tool (GMAT) is a space trajectory optimization and mission analysis system developed by NASA and private industry in the spirit of the NASA Vision. 68, 70

gnuplot gnuplot is a command-line and GUI program that can generate two- and three-dimensional plots of functions, data, and data fits. 26

gyroscope A gyroscope is a device used for measuring or maintaining orientation and angular velocity. 7, 16, 23

heliocentric coordinate system Heliocentric coordinates express the true spatial position of a feature in physical units from the center of the Sun. 19

heliocentric ecliptic frame The origin is the Sun's center, the plane of reference is the ecliptic plane, and the primary direction (the x-axis) is the vernal equinox. 19

IPS An ion propulsion system is a form of electric propulsion used for spacecraft propulsion. It creates thrust by accelerating ions using electricity. 15

inclination (i) Orbital inclination measures the tilt of an object's orbit around a celestial body. It is expressed as the angle between a reference plane and the orbital plane or axis of direction of the orbiting object. 52

JPL The Jet Propulsion Laboratory (JPL) is a federally funded research and development center and NASA field center in the city of Pasadena in California, United States. 18, 85

Julian Days The Julian day is the continuous count of days since the beginning of the Julian period, and is used primarily by astronomers, and in software for easily calculating elapsed days between two events. 69

Jupyter Notebook The Jupyter Notebook is a web-based interactive computing platform. 33, 42, 56, 66, 87

Kalman Filter It is an algorithm that uses a series of measurements observed over time, including statistical noise and other inaccuracies, and produces estimates of unknown variables that tend to be more accurate than those based on a single measurement alone, by estimating a joint probability distribution over the variables for each timeframe. 12, 33, 68, 83–85, 87

Least Squares method The method of least squares is a standard approach in regression analysis to approximate the solution of overdetermined systems by minimizing the sum of the squares of the residuals made in the results of each individual equation. 15

Levenberg-Marquardt algorithm In mathematics and computing, the Levenberg-Marquardt algorithm, also known as the damped least-squares method, is used to solve non-linear least squares problems. These minimization problems arise especially in least squares curve fitting. Applied to artificial neural network training, a Levenberg-Marquardt algorithm often converges faster than first-order backpropagation methods. 15

longitude of the ascending node (Ω) The longitude of the ascending node is the angle from a specified reference direction, called the origin of longitude, to the direction of the ascending node, as measured in a specified reference plane. 52

LOS A straight line along which an observer has unobstructed vision. 12, 15–20, 80

LRGB LRGB, short for Luminance, Red, Green and Blue, is a photographic technique used in amateur astronomy for producing good quality color photographs by combining a high-quality black-and-white image with a lower-quality color image. 32

$M_\odot$ The solar mass is a standard unit of mass in astronomy, equal to approximately 2×10^{30} kg. It is approximately equal to the mass of the Sun. 24

magnetic field (B) Angular velocity or rotational velocity, also known as angular frequency vector, is a vector measure of rotation rate, that refers to how fast an object rotates or revolves relative to another point. 8

Markov process A Markov process is a random process in which the future is independent of the past, given the present. Thus, Markov processes are the natural stochastic analogs of the deterministic processes described by differential and difference equations. 12

Mathematica Wolfram Mathematica is a software system with built-in libraries for several areas of technical computing that allow machine learning, statistics, symbolic computation, manipulating matrices, plotting, etc. 11, 18, 33, 56, 68, 74, 76, 87

mean anomaly (M) It is the fraction of an elliptical orbit's period that has elapsed since the orbiting body passed periapsis, expressed as an angle which can be used in calculating the position of that body in the classical two-body problem. It is the angular distance from the pericenter which a fictitious body would have if it moved in a circular orbit, with constant speed, in the same orbital period as the actual body in its elliptical orbit. 52

mean motion (n) Mean motion is the angular speed required for a body to complete one orbit, assuming constant speed in a circular orbit which completes in the same time as the variable speed, elliptical orbit of the actual body. 52

minor-moon A minor-planet moon is an astronomical object that orbits a minor planet as its natural satellite. 7

NASA The National Aeronautics and Space Administration is an independent agency of the U.S. federal government responsible for the civilian space program, as well as aeronautics and space research. 11, 18, 85

Newton-Raphson method In numerical analysis, Newton's method, also known as the Newton-Raphson method, named after Isaac Newton and Joseph Raphson, is a root-finding algorithm which produces successively better approximations to the roots (or zeroes) of a real-valued function. 15

parallax Parallax is a displacement or difference in the apparent position of an object viewed along two different lines of sight, and is measured by the angle or semi-angle of inclination between those two lines. 9, 18

perihelion (q) The position of closest approach, i.e. the shortest distance between the Sun and the planet, is known as the perihelion. At this point in the orbit, the planet is moving at its maximum speed (Keplerâ€™s Second Law). The perihelion refers specifically to orbits around the Sun, and is equivalent to the periapsis of a general orbit. 15, 16, 52

period (T) The orbital period (also revolution period) is the amount of time a given astronomical object takes to complete one orbit around another object. 52

pixel In digital imaging, a pixel is the smallest addressable element in a raster image, or the smallest addressable element in an all points addressable display device. 11, 15, 17, 20, 28, 29, 31, 56–60

Point Spread Function (PSF) The point spread function (PSF) describes the response of an imaging system to a point source or point object. A more general term for the PSF is a system's impulse response, the PSF being the impulse response of a focused optical system 33, 41, 42, 56

pulsar A celestial object, thought to be a rapidly rotating neutron star, that emits regular pulses of radio waves and other electromagnetic radiation at rates of up to one thousand pulses per second. 7

RA/Dec The right ascension (RA), α, measures the angular distance of an object eastward along the celestial equator from the vernal equinox to the hour circle passing through the object. The declination (Dec), δ, measures the angular distance of an object perpendicular to the celestial equator, positive to the north, negative to the south. 18, 45, 46, 49, 53, 55, 59, 60, 65, 67, 69, 80, 82, 87

RGB The RGB color model is an additive color model in which the red, green, and blue primary colors of light are added together in various ways to reproduce a broad array of colors. The name of the model comes from the initials of the three additive primary colors, red, green, and blue. 32

semi-major axis (a) The semi-major axis is the longest semidiameter or one half of the major axis, and thus runs from the centre, through a focus, and to the perimeter. In astronomy, the semi-major axis is one of the most important orbital elements of an orbit, along with its orbital period. For Solar System objects, the semi-major axis is related to the period of the orbit by Kepler's third law. 52

sextant A sextant is a doubly reflecting navigation instrument that measures the angular distance between two visible objects. 16, 17

SIMBAD SIMBAD is an astronomical database of objects beyond the Solar System. It is maintained by the Centre de donnÃ©es astronomiques de Strasbourg, France. 41, 42

solar-sail Solar sails are a method of spacecraft propulsion using radiation pressure exerted by sunlight on large mirrors. 23, 24, 85, 87

spectrometer A spectrometer is a scientific instrument used to separate and measure spectral components of a physical phenomenon. 15

SPK SPK file is typically a tar file with standard files and structure. 18

star catalog A star catalog is an astronomical catalog that lists stars. In astronomy, many stars are referred to simply by catalogue numbers. 10, 17

Stellarium Stellarium is a free open source planetarium for your computer. It shows a realistic sky in 3D, just like what you see with the naked eye, binoculars or a telescope. 25, 26, 28, 49, 64, 65, 71, 72

telemetry Telemetry is the in situ collection of measurements or other data at remote points and their automatic transmission to receiving equipment (telecommunication) for monitoring. 7

topocentric Measured from, or as if observed from a particular point on the earth's surface. 71

Δv The change in velocity. 23

"A preliminary draft and conclusions about our work were provided in an oral presentation at the 1st Workshop on Open Source Space Mission Design Tools hosted online on 1 March 2022 by the Department of Aerospace Engineering of the Izmir University of Economics in Izmir, Türkiye" [1]

2 Introduction

The increase in the growth of space missions both in numbers and improvements started to require replacing the conventional navigation systems with onboard systems. Historically, spacecraft navigation has been done by ground-based antennas, radars, telemetry, and similar tracking methods. The procedure in obtaining the current position and velocity is to demand information from the Deep Space Network, which is now indicated to be overused and inadequate to supply each incoming request. Considering an interplanetary mission, relying on the DSN makes it even poorer in terms of sturdiness and reliability. Therefore, autonomous/onboard navigation systems need to be introduced to the spacecraft in need of persistent information and/or traveling to far off asteroids, planets, and minor-moons in deep space.

As introduced by D. Wang, et al. (2021), autonomous navigation includes four different branches: inertial navigation, autonomous optical navigation, autonomous navigation based on pulsars, and navigation based on artificial beacons [2].

Pulsar-based autonomous navigation utilizes a pulsar's ephemeris position to extract the information as an initial signal estimation. Then, this first measurement is compared with a specified reference location to obtain a phase offset between the reference point and the spacecraft in the route of the pulsar [3].

Artificial beacons or active landmarks are devices that help the involved object, generally air/spacecraft, robots, or ships, to find its direction to the beacon by transmitting radio signals. They can be benefited in geostationary (GEO) and inclined orbit satellites [4], and not applicable for a satellite traveling deep space. We are left with two autonomous navigation methods, optical and inertial, which are the interests of this project.

2.1 Autonomous inertial navigation system

The inertial navigation system can be expressed as a method to obtain the current orientation and velocity of the object relative to a reference point, using the onboard accelerometers and gyroscopes. Generally, an inertial navigation system contains gyroscopes and accelerometers which are responsible for measuring angular velocity (ω) and linear acceleration respectively, which is then integrated to determine position.

An accelerometer works with the forces caused by vibration and elasticity which can be created with a spring-mass system, and because of a certain movement or the forces introduced into the system, the proof mass would displace by moving between two parallel plates of the capacitor. Capacitive accelerometers work with the change in electrical capacitance caused by acceleration. Meaning that, the capacitor's plates change their position due to the acceleration, which also affects the capacitance, C since it is calculated by,

$$\mathrm{C} = \epsilon_0 \frac{A}{s} \tag{1}$$

where A is the area of the plate, and s is the distance between the plates. These two plates create two air gaps that increase or decrease with respect to the direction of motion and alter the capacitance proportional to acceleration. The amount of acceleration can tell if the device is moving, how it is moving, is it falling, or at which angle it is moving. Obtaining the tilting angle of a device relative to the Earth can be determined by a dynamic accelerometer which essentially measures the gravitational pull. It is possible to obtain the linear acceleration of a spacecraft in the inertial reference frame by processing its current angular velocity (ω) and linear acceleration, measured with respect to the spacecraft. Considering the initial conditions, integrating the inertial accelerations in the equation of motion would give the inertial velocities. And, the second integration would give the inertial position by using the original position as initial conditions [5].

However, the inertial navigation system cannot serve for long periods (cruise) but only for shorter periods (maneuvers), since uncertainty in the measurement of acceleration would create a bias on the velocity and a deflection on the position [6]. In order to have control over each direction, at least three accelerometers need to be introduced in an inertial navigation system, therefore to be able to face all directions. Because of the existence of electricity between the parts, a magnetic field ($\mathbf{B}$) occurs to perceive the alteration in moving parts. Thus, the inertial measurement unit can estimate the current position and velocity of the object with physical occurrences. And, the current velocity and position of the spacecraft are the essentials for navigation and control. Other than the fact that inertial navigation systems are autonomous and conductible in various environments without needing any ground-based tracking systems, it may also increase the total cost of the mission or may cause drastic errors in the case of a poorly executed operation [7].

2.2 Autonomous optical navigation system

The optical navigation plays a more crucial role in this project since it needs to be in charge for a longer time in the mission. The optical navigation system is an image-based measuring method, collaborating with an inertial navigation system, and possibly the DSN, which acquires the needed data from the attached cameras on the spacecraft, and ephemeris information.

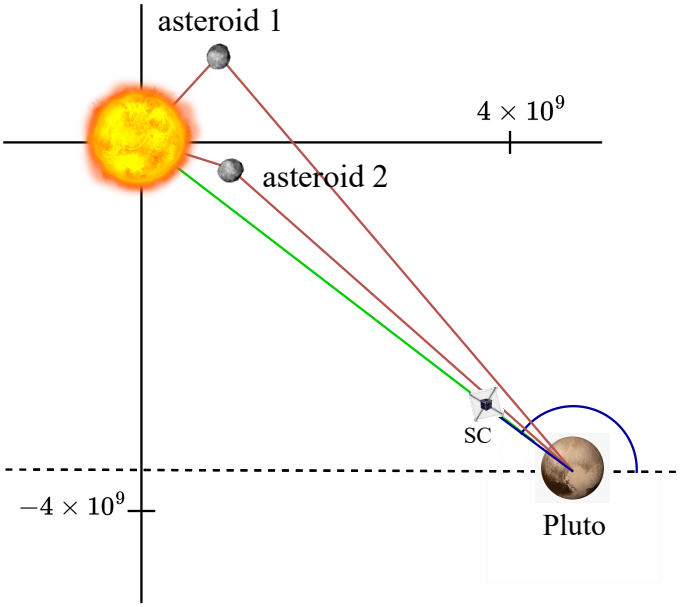

Figure 1: Measurement geometry, sketched via diagrams.net

Cameras are responsible for providing photographs of a celestial body or an asteroid placed against a star whose coordinates are known. Then, processing this image and determining the trigonometric relationship, parallax, shown in Fig. 1 which is sketched according to our results presented in Sec. 7.5, between the spacecraft and the celestial object produces an optical correlation to be used in navigation.

M. Paluszek, et al. (2010) presented a flexible optical navigation system for deep space missions, and they listed the observables that can be used in optical measurement, see Fig. 1 in Paluszek [8]. For our case, we are interested in the angle between a celestial body (an asteroid), and its distance to the Sun which can be acknowledged as the center of coordinates [8].

Another important fact that needs to be considered is the capacity of the cameras used for the mission. It is very tough to obtain excellent optics when the camera automatically gets micro or nano-proportional to the size of the spacecraft. Optics restrict the number of distinguishable celestial objects, which may cause a tremendous amount of error in the measurement. But with the great improvements in nanotechnology, engineers are able to produce according to intentions, and autonomous optical navigation has become possible also for micro/nanosatellites with micro/nano cameras attached.

The presence of Auto-Nav greatly increases the possibilities to improve the mission capabilities without completely trusting on the DSN. Building an independent CubeSat-class spacecraft does not only benefits the mission requirements and demands but also advances the mission itself by reducing the size and weight, creating more space for additional components, instruments, or technologies, and diminishing the mission cost caused by total payload.

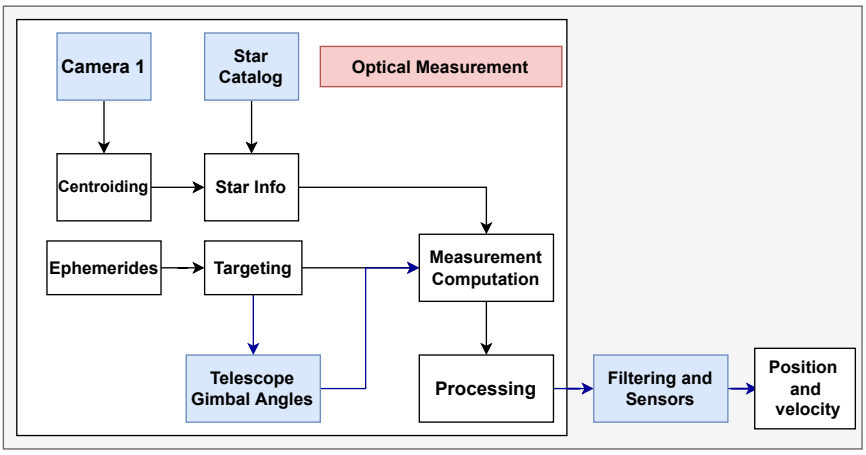

Figure 2: Autonomous optical navigation block diagram. (Adapted from Ref. [8], sketched via diagrams.net)

Fig. 2, shows a conceptual block diagram for the workflow of the autonomous optical navigation system. This hypothetical system utilizes a camera as an acquisition sensor to capture the objects present in the environment. Then identifying the information/ID of the observed stars using a star catalog. The position of the celestial objects is determined with the help of ephemeris, which is crucial for targeting and affects the inertial measuring accordingly. Combining and processing the information coming from optical and inertial navigation systems produce the current position and velocity of the spacecraft.

2.3 Image acquisition

The essential tool to produce an image to process for navigation is a CCD camera which is one of the most trivial technologies utilized in modern optics. CCD cameras allow to produce photographs with a strong resolution, dynamic range and a great acquisition speed compared to other technologies, which would be the number one reason to implement them into high technology/cost missions [9].

Before diving into capturing a picture, the camera needs to be calibrated in order to produce a correctly distorted image. Camera calibration (a.k.a camera re-sectioning) is an estimate of the lens parameters and image sensor. Adjusting these parameters according to the desired lens distortion allows us to measure the real size of captured objects, or determine the location of the camera itself corresponding to its environment [10].

After the camera is correctly calibrated, the image processing procedure can be initialized, which plays the leading role in navigation since it is the part where one extracts information out of that frame. Image processing can be classified as a branch of signal processing where an image is an input instead of a signal. The output can be either a better quality image or any other information that can be extracted out of that image. Hence, for navigation systems, pixels are utilized to be turned into digital data. In this project, we use Mathematica as the operating system for creating synthetic stars and processing the obtained data thoroughly, which is declared in Sec. 4 with details.

3 Literature Review

3.1 N. B. Stastny, et al. "Autonomous optical navigation at Jupiter: A linear covariance analysis" (2008)

N. B. Stastny and D. K Geller (2008) presented a study on the efficiency of optical measurements of the moons of Jupiter to determine a spacecraft's position and velocity while it's approaching Jupiter and analyzed the outcome using a linear covariance analysis. The covariance of two variables can be expressed as a measure of their combined variability between a reference trajectory and an estimated trajectory. Besides estimating the error covariance about the nominal trajectory, this technique eliminates the need to estimate the system state.

They considered a suitably realistic truth model and simulation to analyze the optical navigation technique and utilized four methods in this sense. First off, is defining moons' positions using the information from NASA archive, as well as the celestial bodies' ephemerides. And by analyzing those positions, the spacecraft position can be determined with scientific tools.

An Auto-Nav system can obtain mission path and position information [11]. Then, it is essential to calculate the gravitational forces from the near planets, since it is important to develop the path and simulate movements of the spacecraft and its trajectory. They have introduced Kalman Filtering as the linear quadratic estimation. Kalman Filtering is a type of algorithm which uses measurements taken over by time and tries converging to the real value using previous measurements. Because of the joint probability distribution for each time frame over the variables, it is one of the best ways to define errors and compare them with previous amounts. They have proceeded with identifying the error sources and stressed the priory covariance, which is the spacecraft's estimated inaccuracy in velocity and position relative to the effect of the gravity force from the near planet. And suggested that it may be fixed by the Earth-based systems or alternative methods of navigation. Unmodeled gravitational or non-gravitational accelerations are represented as process noise in the linear covariance tool (similar to the Kalman Filtering Method), and they show the difference between an elevated onboard gravity model and the actual gravity. White noise is used to represent the process noise. The white noise accelerations' capacity is measured in m^2/s^3, which means that the non-gravitational accelerations produce a velocity variance in m^2/s^2 that grows at a rate of m^2/s^3.

The attitude knowledge errors of the spacecraft, which are modeled from a first Markov process, are straightforwardly estimated as filter elements and powered by white noise. To match the accuracy of a star camera attitude update, a standard deviation of 1 arc-sec per axis was chosen, and 10 arc-sec per axis as an alternative setting. The misalignment of the camera mounting is directly estimated as a filter element. With a priory uncertainty of 0.01 degrees per axis, the misalignment error is assumed to be constant, and 0.1 degrees per axis is an alternative setting. Even though this parameter is included in the estimation filter, any sensor misalignment is likely to be measured out of any mission. The number of optical navigation cameras, which is expected to be a single camera, the spacecraft's capacity to realign its attitude to point at a new moon, and extra demands on the spacecraft limit the imaging frequency. The nominal imaging frequency is to capture a new moon every two hours to minimize reorientation maneuvers. The other option is to set the timer to six hours. Since the true error direction is unknown, it can be assumed that it is perpendicular to the spacecraft's LOS to the Moon. The result of the standard deviation of the error in the image measurement is:

$$\sigma_{\text{ephem}} = \frac{\Delta r}{r_{sm}} \tag{2}$$

where Δr is the moon's ephemeris knowledge error, and r_{sm} is the range from the spacecraft to the moon.

The location of the moon's center-of-mass (CM) pixel, as contrasted to the target's center of brightness (CB), must be determined from captured photos. Image processing faults can be approximated as a percent of the moon's diameter for errors in the CM pixel position. As they have stated "When the imaged moon is relatively close to the spacecraft, errors in CM pixel position will dominate. When the image's moon is further away, the image center-finding bias becomes insignificant and is dominated by measurement noise [11]." Center finding errors may directly cause position errors since it is dependent on the center and expected point. Therefore, the camera most possibly produces some noise because of the environment's continuous work. They have finalized their study by stating that the autonomous algorithm uses the results/images obtained from the camera, to design or create a simple model. When image processing is used in combination with the analysis, a basic model describing the uncertainty in Auto-Nav's moon measurement can be provided [11].

3.2 Gerald M. Levine, "A method of orbital navigation using optical sightings to unknown landmarks" (1966)

Estimating the velocity and position of a spacecraft has been studied for a long time. Although this paper may be classified as ancient, it is worth to be reviewed since the navigation systems are also old enough to rely on. Gerald M. Levis (1966) conducted a study on orbital navigation using optical sightings. The paper introduces estimations of the position and speed of the spacecraft and compares them with the values obtained from actual measurements. The correctly calculated angles between the considered celestial bodies allow the Auto-Nav system to operate. This navigation system produces the desired information as a result of the operations to be performed with two images taken from the same location [12].

Comparison between the estimated and measured values leads us to determine the speed and position of the spacecraft. Error transition matrix, W, is used so that the obtained measurement data can be included in the process efficiently. The reason for not using the covariance matrix is that it is difficult to maintain the positive covariance matrix during long space missions. Therefore, the error transition matrix is used rather than the covariance matrix. The essentials for the navigation procedure to be used and the landmarks to be detected from the spacecraft are assumed to be the optical instrument, the inertial platform, and a computer. They have presented the unknown-landmark orbital navigation procedure as follows:

Looking at a landmark at time t_0, the unit vector measured from the spacecraft to the landmark is defined as $\mathbf{u_0}$. When the landmark point is targeted, it is assumed that the key is pressed and the t_0 and $\mathbf{u_0}$ values are automatically saved in the computer's memory.

Of course, a single measured value is useless. The spacecraft re-targets the same landmark a few seconds later, and a second sight $\mathbf{u_1}$ is obtained and stored again. A plane is created from points $\mathbf{r_0}$ to $\mathbf{r_1}$, and the velocity vector of the spacecraft, between these two points, does not have a component perpendicular to the generated plane, which can be called the normal point, $\mathbf{r}$. Let θ be the angle between $\mathbf{r_0}$ and $\mathbf{r_1}$, and the angle between $\mathbf{r_0}$ and r be ϕ. Then, solving the Kepler's equation, allows us to obtain the conic position $\mathbf{r_1}$ at time t_1 from the position and velocity estimates, $\mathbf{r_0}$ and $\mathbf{v_0}$ at t_0. And, determining the angle ϕ from,

$$\theta = \frac{\tan^{-1}(|\mathbf{r_0} \times \mathbf{r_1}|)}{(\mathbf{r_0}^{\mathbf{T}}\mathbf{r_1})} \tag{3}$$

$$\phi = \frac{\theta}{2} + 2\tan^{-1}\left[\frac{1-(r_0/r_1)^{1/2}}{1+(r_0/r_1)^{1/2}\tan\frac{\theta}{4}}\right] \tag{4}$$

Then, calculating the estimated time t, that the spacecraft was at the normal point by using the angle θ and Kepler's equation. Use the position estimate of the $\mathbf{r_1}$ to convert $\mathbf{u_1}$ to $\mathbf{u_1'}$ to account the Earth's rotation as well. Integrating the values of $\mathbf{r_0}$ and $\mathbf{v_0}$ into time, t, to get the $\mathbf{r'}$ and $\mathbf{v'}$ values. Let $\mathbf{n}$ be the unit vector in the direction of $\mathbf{u_0} \times \mathbf{u_1'}$. Accordingly, see Fig. 1 in Levine, the geometry vector is given by, $b = \begin{pmatrix} 0 \\ 0 \\ 0 \\ n \end{pmatrix}$. Taking $\mathbf{n}$ as a measured quantity, the measured value $\mathbf{Q'}$ is zero, and the estimated value $\mathbf{Q''}$ is $\mathbf{n^T v'}$. Therefore, subtracting the measured from the estimated gives:

$$\mathbf{Q'} - \mathbf{Q''} = -\mathbf{n}^T\mathbf{v'} \tag{5}$$

Finally, calculating the new estimates $\mathbf{r}$ and $\mathbf{v}$, and the updated error transition matrix, W, allow to proceed from time t, which concludes the basis of Levine's method of orbital navigation using optical sightings to unknown landmarks [12].

3.3 S. Li, et al. "Image processing algorithms for deep-space autonomous optical navigation" (2013)

S. Li, et al. presented a study in 2013 on image processing algorithms for spacecraft traveling through deep-space, stressing the fact that image processing is quite crucial for autonomous optical navigation systems since they rely on extracting observables from an image. They have introduced three new image processing algorithms. The first one is the multiple-image pre-processing which intends to prepare the image before the actual processing by eliminating uninteresting areas to widen the interest area without extra information, and the Canny edge detection algorithm which aims to determine the edges of target bodies to eliminate the

possible false edges by reducing the noise and accurately positioning the edge points. Then, they presented two limb profile fitting algorithms which are essentially established from the Least Squares method and the Levenberg-Marquardt algorithm, presuming that the celestial body completes an elliptical shape on the image plane. Using the Least Squares method, they represented the elliptic section as an implicit quadratic equation and designed a solution numerically by using Newton-Raphson method. On the other hand, using the Levenberg-Marquardt algorithm, they minimized the non-linearity of the function. Finally, they have obtained the LOS vector from the spacecraft to the centroid of the body corresponding to the ellipse equation of the fitted limb profile, which is acknowledged as the navigation measurement observable and introduced to the algorithm as an input to determine the current position of the spacecraft.

To obtain a more explicit result, they have tested the algorithms both on real images and on synthetically created images. Both of the tests have given an accurate and satisfactory output by successfully extracting the observables from images.The error of the LOS vector came up less than 1.67×10^{-4} radians, and the maximum ellipse fitting errors were less than 3 pixels which support the deep-space autonomous navigation needs and prove the accomplishment of this study [13].

3.4 L. A. Soderblom, et al. 'Observations of comet 19P/Borrelly by the miniature integrated camera and spectrometer aboard Deep Space 1" (2002)

Deep Space 1 (DS1) mission is the first ion-propulsion (IPS) spacecraft that traveled through deep-space. During the mission, a spectrometer and a miniature integrated camera worked on finding and collecting visible-wavelength images and short-wavelength infrared spectra [14]. This article specifically examines the sunlight that appears on the left of the image frame.

During the DS1 mission, a CCD camera was assigned to take images of the comet 19b/Borelly. However, DS1 failed in the main mission which was detecting its current position, instead, it noticed this comet, and DS1 visited the comet in 2001. On May 28th, 2015, the comet passed through perihelion (q) (nearest approach to the Sun), and it is calculated to do it again on February 1, 2022. From 3,400 kilometers distant, DS1 captured images of the comet's core. It was the best quality image of a comet ever seen, at 45 meters per pixel. The miniature integrated camera produced such images that, "The surface of Borelly's nucleus was covered by dark material, having an average geometric albedo of only 0.03 ± 0.005, with darker spots ranging down to ~ 0.01 [14]." Dark areas near the boundary suggest a very slight phase change, which is a feature of the coma. With solar phase angle, the dark areas centered in the illuminated end of the nucleus alter in brightness. And, the topographic model they introduced shows that those spots are around 45° from the subsolar point.

They found that the albedo ranges from ~ 0.01 to ~ 0.035, which is generally accepted as 0.04 in studies, with a factor of 3 between the darkest and the brightest areas. It is possible that the darkest albedo spots are made up of various materials or have various particle measurements and compaction effects.

Borrelly always demonstrated a conspicuous sunward asymmetry in its coma. The coma elongates in the direction of the Sun as a consequence of this fact. As they state "During the approach, the coma's sunward asymmetry was reduced to a broad dust beam, just a few kilometers wide at its base, arising from the nucleus broad central basin. This jet-like dust feature, which we call the α jet, was canted about 30° from the direct Sun line [14]." And, they observed in the DS1 images that it ranges to 100 kilometers where its brightness goes out of the detection limit. Fig. 8(A) in Soderblom, includes the image captured with a range of $\sim 13,130$ km, resolution of 173 m/pixel, phase angle of $\sim 79.6°$, and (B) with a range of ~ 4825 km, resolution of 63 m/pixel, phase angle of $\sim 62.5°$. The major jet of Borrelly has been spotted several weeks earlier to the encounter. Images were taken 11 to 34 hours before the collision contain enough detail to demonstrate that the main jet's orientation is within around 5 degrees of what was seen at the encounter. Consequently, the main jet was reported to be stagnant for longer than the 26 hour period. They determined that the main jet is almost parallel to the nucleus' rotation axis. During perihelion (q) passage, the subsolar latitude is 60° N, and the pole receives continual sunshine. The direction of the pole is adaptable with the steady rotation of the nucleus along its shorter axis. The almost on-axis main jet's non-gravitational forces then have a negligible influence on this stable rotational state [14].

3.5 David G. Hoag, "The history of Apollo onboard guidance, navigation, and control" (1983)

The control systems used in Apollo mission were covered by David G. Hoag in 1983. In Apollo mission they used "a space sextant to make periodic navigation angle measurements between pairs of celestial objects". Similar to the Mars probe but more improved space sextant has been used to operate the autonomous navigation measurements. They included two-single axis gyroscopes and an accelerometer for angle and velocity change measurements. Satisfactory sextant design as a result of long studies was fixed along "the axis of penetration of the spacecraft hull" and affiliated with "the Earth or the Moon side of the navigation". "The other line-of-sight (LOS) associated with the reference star was split from the first and tipped away by an articulating mirror in a way that the navigation angle could be successfully measured in any plane. The angle of tilt of the mirror, in conventional sextant fashion, was the desired measurement and was encoded for use by the computer navigation and alignment algorithms [15]."

To maintain the power of the spacecraft, the inertial system had to be shut down for most of its mission, so various optical systems were developed and tested. Afterward, a sextant study was performed that corrected its angle with respect to the stars and prevented the inertial measurement unit shift in orientation once or twice a day periodically, and problems caused by a small field of view diffused sunlight. In this work, the sextant were used gimbal angles to orient the star line to the targeted star. The gyro drift of the star in the sextant FOV was small enough that it always appeared bright. The image needs to be centered with the data needed to realign the inertial unit. This ensured correct inertial alignment throughout the mission. Also, the computer can orient the spacecraft to targets specified by the onboard crew. Despite the scattered light problem they have encountered with targets, the scanning telescope provided a good tracking tool for navigational observations of the Earth and Moon in low orbit around these objects. The crew measured the LOS to the surface target, then the navigation angle with the scanning telescope, using the inertial measurement unit that had been pre-aligned by the computer. Orientation relationships between the inertial unit and optical sight lines, both instruments designed a common mounting bracket inside to ensure the stability of the alignment between these instruments.

The joint mounting bracket, called the navigation base, was designed in a lightweight but rigid structure then fastened to the spacecraft by kinematic mounting to isolate the spacecraft strains. Automated star tracker and accompanying sextant designed to solve the Earth and the Moon navigational compatibility issues. After these were removed for cost and confusion, the images of the Earth horizon were reexamined for navigation use and a simulator with photometric accuracy was designed. And, a locator could be selected on the blurred horizon, which could be replicated with remarkable accuracy [15].

4 Methodology

4.1 Position of a celestial body in the reference frame of a spacecraft

The captured image will demonstrate the stellar field of the spacecraft's current location. The initial step is determining the positions of the stars appearing in that image. Since stars do not emerge as dots but as scattered pixels in an image, determining the x and y coordinates of that disc shape is not deceptive yet possible. The origin of the x and y coordinates of the disc is called "centroid", and finding the center of the star is called "centroiding". Once we obtain the center of the star, coordinates of each star in that stellar field can be identified by using a star catalog, and "Astrometry.net" can be benefited in this sense since it is an extremely accurate and strong astrometric calibration service.

After identifying the centroids of the stars, the asteroids in that stellar field can also be identified using the ephemeris, which is the step where NASA's "Horizons System" introduces itself. Horizons System is a FOSS and a highly-accurate ephemeris computation service designed and constantly updated by JPL's Solar System Dynamics group who are responsible for the Mission Design and Navigation section. The website provides physical parameters and motions mainly of natural planets, satellites, and asteroids [16]. The fundamental intention of this project is setting RA/Dec of the spacecraft, and obtaining the RA/Dec of a certain asteroid to build the trigonometrical relationship and calculate the parallax according to the movement of the spacecraft over a period of time while observing a certain stellar field from the spacecraft's location. Our supervisor, Dr. Fabrizio Pinto reached out to the developers of Horizons, and we sadly found out from Mr. Jon Giorgini who is in charge of the Horizons system and radar astrometry section at JPL, that "An asteroid's RA/Dec can be obtained with respect to a spacecraft but the spacecraft must be pre-defined in Horizons with an SPK file." And, he stressed that "Users cannot manually input a single state and get RA/Dec relative to the spacecraft." which is essentially what we intend to perform.

4.1.1 Elements of autonomous optical navigation

As introduced earlier in Sec. 2.2, the operational concept behind the optical navigation system initializes with capturing an image of a stellar field, and processing that image to acquire data from the targeted celestial body through an optical imaging sensor (camera). Then, associating the identified asteroid with the ephemeris information to calculate the trigonometric relationship (parallax) between the spacecraft and the asteroid in order to autonomously determine the position, therefore the velocity of the spacecraft.

According to D. Wang and others, data for navigation can be determined with center-point, edge-point, and feature-point information [2]. This project intends to follow the center-point method which can be expressed as determining the RA/Dec of the centroid of the celestial body to incorporate with the spacecraft's attitude to determine its position and velocity information through a filtering algorithm which is planned to be executed by Mathematica.

Celestial bodies in the FOV of the spacecraft can be used as navigational beacons if their ephemeris information is known. For an accurate operation, the beacons need to be chosen carefully. D. Wang and others present a three-step path-way for this issue:

1. Select m number of beacons from the ephemeris as initial possibilities.
2. Then, select n number of beacons from the initial m possibilities to observe if they are in the LOS and observable.

3. Finally, designing the observing stage as efficient as possible by initializing from the starting attitude, and observing the n number of beacons with maneuvering and arriving to the starting attitude at the end of the whole observing stage.

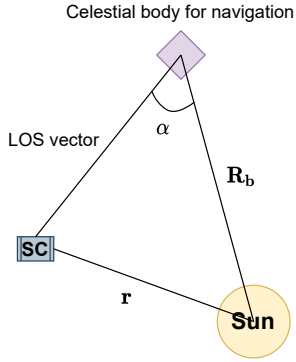

Figure 3: Optical autonomous navigation based on LOS. (Adapted from Ref. [2], sketched via diagrams.net)

Considering a similar sketch as Fig. 1, Fig. 3 displays the geometric relationship between the spacecraft and the target object based on LOS direction information, where $\mathrm{R^b}$ is the position vector of the beacon relative to the Sun. The solar phase angle, α, the angle between the Sun and the spacecraft relative to the center of the celestial object, can be calculated as,

$$\alpha = \arccos\left[\frac{(\mathrm{r_a} - \mathrm{r}) \cdot \mathrm{r_a}}{||\mathrm{r_a} - \mathrm{r}|| \cdot ||\mathrm{r_a}||}\right] \tag{6}$$

where in Eq. 6, $\mathrm{r_a}$ is the position of the celestial object in a heliocentric ecliptic frame and $\mathrm{r_a}$ is the position of the spacecraft in the heliocentric coordinate system. If α is equal to 180°, light coming from the Sun would enter the camera directly which is not ideal, and needs to be avoided in order to obtain a useful image of the stellar field.

Referring back to Fig. 3, set $\mathrm{n^c}$ as the LOS direction of navigation beacon expressed in the camera frame, $\mathcal{F}_c$, and $\mathrm{n^n}$ as expressed in the navigation frame, $\mathcal{F}_n$.

$$\mathrm{n^c} = \mathbf{C}_n^c \mathrm{n^n} + \nu \tag{7}$$

where in Eq. 7, $\mathbf{C}_n^c$ is the attitude transformation matrix from $\mathcal{F}_n$ to $\mathcal{F}_c$, and ν is the observation noise caused by the camera. Then,

$$\mathrm{n^n} = \frac{\mathbf{R}_b^n - \mathbf{r}^n}{||\mathbf{R}_b^n - \mathbf{r}^n||} \tag{8}$$

Combining Eq. 8 and Eq. 7, the measurement equation based on LOS direction information can be determined as,

$$\mathrm{n^c} = \mathbf{C}_n^c \frac{\mathbf{R}_b^n - \mathbf{r}^n}{||\mathbf{R}_b^n - \mathbf{r}^n||} + \nu \tag{9}$$

Therefore, if $\mathbf{R}_b^n = 0$, then the targeted celestial object is the beacon whose the measurement is LOS direction, which would occur in the approaching and orbiting phases. Rewriting Eq. 9 according to that would result to,

$$\mathrm{n^c} = -\mathbf{C}_n^c \frac{\mathbf{r}^n}{||\mathbf{r}^n||} + \nu \tag{10}$$

However this project investigates the case of, $0 < R_b^n < \infty$, and $\mathbf{R}_b^n$ is known by ephemeris. Meaning that the beacon is a large distant object such as asteroids, and the type of flight may be a deep-space transferring or orbiting. Also, if the camera has a large FOV, it may detect more than one LOS which would decrease the errors in attitude determination. Considering the given case, Eq. 9 can be rewritten as,

$$\theta_{12} = \arccos(\mathbf{n}_1^n \cdot \mathbf{n}_2^n) + \nu = \arccos\left(\frac{\mathbf{R}_{b,1}^n - \mathbf{r}^n}{||\mathbf{R}_{b,1}^n - \mathbf{r}^n||} \cdot \frac{\mathbf{R}_{b,2}^n - \mathbf{r}^n}{||\mathbf{R}_{b,2}^n - \mathbf{r}^n||}\right) + \nu \tag{11}$$

where θ_{12} is the angle between the two LOS directions, $\mathbf{R}_{b,1}^n$ and $\mathbf{R}_{b,2}^n$ are the position vectors of the two beacons expressed in the navigation frame, $\mathcal{F}_n$ [2].

4.1.2 Image analysis

As introduced in Sec. 2.3, the onboard camera produces images in pixels form which is a two-dimensional smallest element of an image, which allows us to write a measurement equation with x and y axes. Fig. 4 shows a sketch of the measurement basis of an optical imaging camera, where $x_c y_c$ is the plane of the image and z_c is the axis of the focal length. Implementing the camera frame into the sensor coordinate system [2],

$$\mathrm{n^c} = \frac{1}{\sqrt{x_c^2 + y_c^2 + f^2}} \begin{bmatrix} -x_c \\ -y_c \\ f \end{bmatrix} \tag{12}$$

where f is the focal length of the camera.

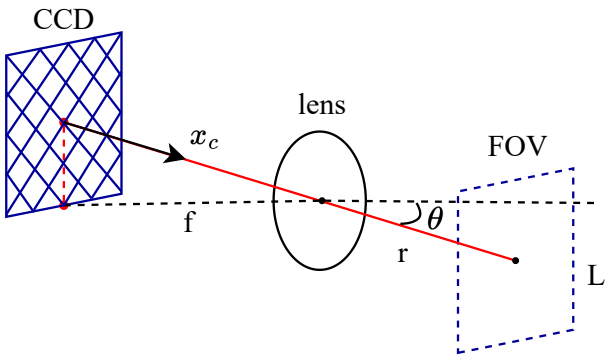

Figure 4: Measurement basis of optical imaging sensor. (Adapted from Ref. [17], sketched via diagrams.net)

Writing $\mathbf{R}_b^n$ and $\mathbf{r}^n$ as:

$$\begin{aligned} \mathbf{R}_b^n &= [x_d, y_d, z_d]^T \\ \mathbf{r}^n &= [x, y, z]^T \end{aligned} \tag{13}$$

Yields to,

$$\frac{\mathbf{R}_b^n - \mathbf{r}^n}{||\mathbf{R}_b^n - \mathbf{r}^n||} = \frac{1}{\sqrt{(x_d - x)^2 + (y_d - y)^2 + (z_d - z)^2}} \begin{bmatrix} x_d - x \\ y_d - y \\ z_d - z \end{bmatrix} \tag{14}$$

Then, substituting Eq. 12 and Eq. 14 into Eq. 9 without considering the measurement noise,

$$\begin{aligned} x_c &= -f \frac{a_{11}(x_d - x) + a_{12}(y_d - y) + a_{13}(z_d - z)}{a_{31}(x_d - x) + a_{32}(y_d - y) + a_{33}(z_d - z)} \\ y_c &= -f \frac{a_{21}(x_d - x) + a_{22}(y_d - y) + a_{23}(z_d - z)}{a_{31}(x_d - x) + a_{32}(y_d - y) + a_{33}(z_d - z)} \end{aligned} \tag{15}$$

where $a_{ij} (i = 1, 2, 3; j = 1, 2, 3)$ are the corresponding elements in the direction of attitude transformation matrix, C_n^c. The projection coordinates of the imaging point on the focal plane can be assigned as (p, l). And, considering the influence of distortion, (p, l) is given as [2],

$$\begin{bmatrix} p \\ l \end{bmatrix} = \mathbf{k} \begin{bmatrix} x_c \\ y_c \\ z_c \end{bmatrix} + \begin{bmatrix} p_0 \\ l_0 \end{bmatrix} + \begin{bmatrix} \nu_p \\ \nu_l \end{bmatrix} \tag{16}$$

where p_0 is the image element, l_0 is the image line the sensor center, ν_p and ν_l are the measurement noise, and $\mathbf{k}$ is the conversion matrix from Cartesian coordinates to pixels denoted as,

$$\mathbf{k} = \begin{bmatrix} k_x & k_{xy} & k_{xxy} \\ k_{yx} & k_y & k_{yxy} \end{bmatrix} \tag{17}$$

The influence of distortion can be neglected, since the values of k_{xy}, k_{yx}, k_{xxy} and k_{yxy} are very small, which yields to $\mathbf{k} = \begin{bmatrix} k_x & 0 & 0 \\ 0 & k_y & 0 \end{bmatrix}$. Then rewriting Eq. 16,

$$\begin{bmatrix} p \\ l \end{bmatrix} = \begin{bmatrix} k_x x_c \\ k_y y_c \end{bmatrix} + \begin{bmatrix} p_0 \\ l_0 \end{bmatrix} + \begin{bmatrix} \nu_{p,i} \\ \nu_{l,i} \end{bmatrix} \tag{18}$$

Finally, substituting Eq. 18 into Eq. 15 considering the measurement noise would give [2],

$$\begin{aligned} p &= -k_x f \frac{a_{11}(x_d - x) + a_{12}(y_d - y) + a_{13}(z_d - z)}{a_{31}(x_d - x) + a_{32}(y_d - y) + a_{33}(z_d - z)} + p_0 + \nu_p \\ l &= -k_y f \frac{a_{21}(x_d - x) + a_{22}(y_d - y) + a_{23}(z_d - z)}{a_{31}(x_d - x) + a_{32}(y_d - y) + a_{33}(z_d - z)} + l_0 + \nu_l \end{aligned} \tag{19}$$

4.2 Workflow block diagram

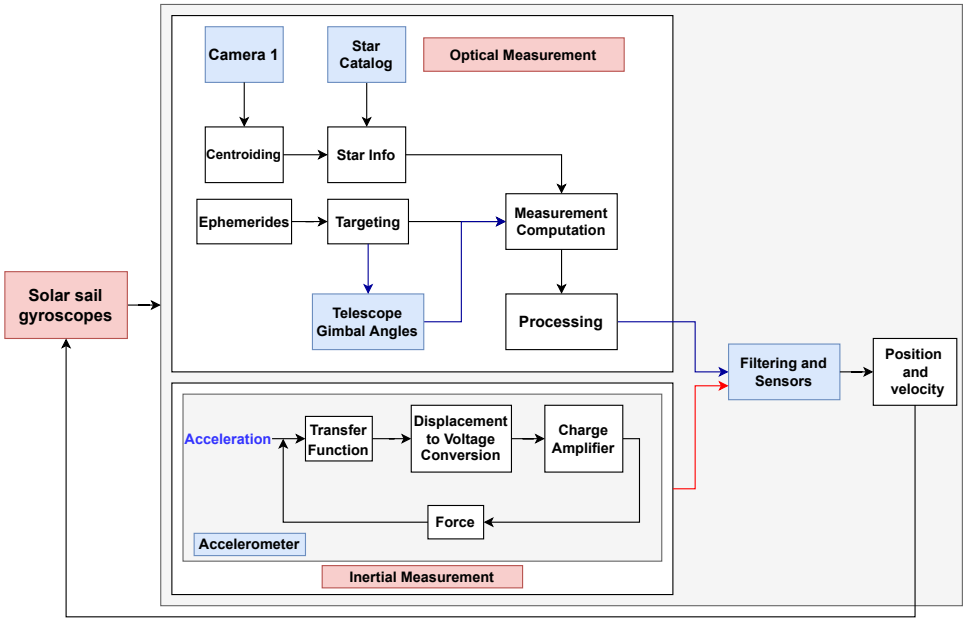

Figure 5: Autonomous navigation block diagram (sketched via diagrams.net)

The general workflow of the procedure is shown in Fig. 5. The basis behind the optical and inertial navigation systems are expressed as block diagrams individually. Combining the information obtained from those two sections and processing them through filtering algorithms with the correct operation would yield the current position and velocity of the spacecraft. Then, the current estimate gets sent to the solar-sail gyroscopes as feedback to use as a previous estimate during the next cycle to reduce the errors in calculation.

4.3 Elements of solar-sailing

A conventional chemical substance burner engine rely on Tsiolkovsky's famous rocket equation, which produces the change in velocity due to the amount of fuel that has been burned throughout. The rocket equation can be written as,

$$\Delta v = v_{\mathrm{e}} \ln\left(\frac{m_{\mathrm{in}}}{m_{\mathrm{fin}}}\right) \tag{20}$$

where Δv is the change in velocity, v_e is the fuel exhaust velocity, m_{in} and m_{fin} are the initial and final mass fo te spacecraft respectively [18]. According to the Eq. 20, as the exhaust velocity gets bigger, the spacecraft performs a greater change in velocity. However, the burning substance limits the exhaust velocity and does not allow the spacecraft to travel through deep-space with a reasonable amount of fuel [19].

On the other hand, solar-sails do not make use of the rocket equation, since they are not propelled with a conventional engine but with solar radiation pressure.

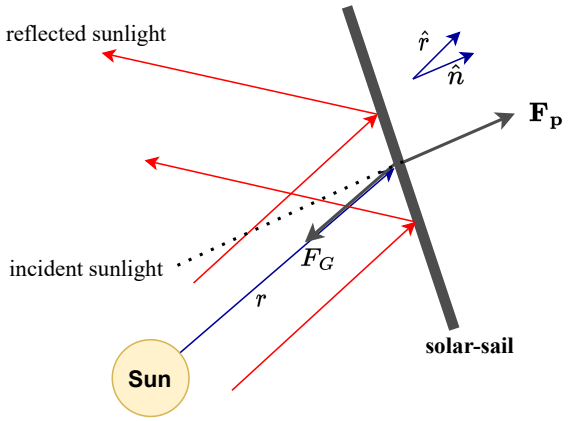

Figure 6: Simplified solar-sail sketch (Adapted from Ref. [19], sketched via diagrams.net)

Fig.6 shows a sketch of a simplified, flat surfaced solar-sail where $\mathbf{F_p}$ is the solar radiation pressure which is normal to the solar-sail, F_G is the gravitational pull facing the Sun which can be neglected for interplanetary missions. Then the solar radiation pressure, $\mathbf{F_p}$ can be written as,

$$\mathbf{F_p} = \frac{2r\cos(\theta_i)\hat{\mathbf{n}} + \alpha\hat{\mathbf{r}}}{c} SA \tag{21}$$

where r is the sail reflectivity across the solar spectrum, α is the coefficient of solar absorptivity, $\cos(\theta_i) = \hat{\mathbf{n}} \cdot \hat{\mathbf{r}}$ is the angle of incidence, $\hat{\mathbf{r}}$ is the radial unit vector in the direction of sunlight, and $\hat{\mathbf{n}}$ is a normal vector to the sail surface. The solar irradiance, S, is equal to $S_{1,\mathrm{AU}}((1\mathrm{AU})^2/r^2)$ where $\mathbf{r}$ is the radial distance between the solar-sail and the center of the Sun [19]. Implementing this into the equation of motion,

$$\frac{\mathrm{d}^2\mathbf{r}}{\mathrm{d}t^2} = -\frac{\mathrm{GM}_\odot}{r^3}\mathbf{r} + \frac{2r(\hat{\mathbf{n}} \cdot \hat{\mathbf{r}}) + \alpha}{c} \frac{(1\mathrm{AU})}{r^2} S_{1,\mathrm{AU}} \frac{A}{m}\hat{\mathbf{n}} \tag{22}$$

where in Eq. 22, $\mathbf{r}$ is the radius vector from the center of the Sun to the solar sail, G and $\mathrm{M}_\odot$ are the gravitational constant and the solar mass respectively.

As the orbit gets smaller the effect of the solar radiation pressure increases, and this increased influence can be used to sail faster, therefore allows to reach the spacecraft to a hyperbolic trajectory with a slingshot maneuver, which is possible at perihelion since the spacecraft is facing towards the Sun, to travel through distant stars/planetary systems [19]. In the case of $\hat{\mathbf{n}} = \hat{\mathbf{r}}$, meaning that $\theta_i = 0$, Eq. 22 can be rewritten as,

$$\frac{\mathrm{d}^2\mathbf{r}}{\mathrm{d}t^2} = -\frac{\mu_{\mathrm{eff}}}{r^3}\mathbf{r} \tag{23}$$

where μ_{eff} is now the effective gravitational parameter and equal to $\mathrm{GM}_\odot - (2r + \alpha)S_{\frac{1,\mathrm{AU}}{c}}(1\mathrm{AU})^2\frac{A}{m}$. Finally, the cruise velocity of the spacecraft can be determined after it reaches to the hyperbolic trajectory,

$$v_\infty \simeq \sqrt{v_0^2 - 2\frac{\mu_{\mathrm{eff}}}{r_0}} \tag{24}$$

where v_0 is the velocity and r_0 is the position of the spacecraft at the perihelion prior the slingshot maneuver [19].

4.4 Proof of concept of centroiding

4.4.1 Astrometry activities

In 1807, astronomer Heinrich Wilhelm Olbers discovered the second largest body in the main asteroid belt, *Vesta*. In 2011, NASA's Dawn spacecraft traveled through the area. Since it has almost a spherical shape, it is practically classified as a dwarf planet. Vesta was the fourth asteroid discovered in history and also one of three bodies which we have samples here on Earth [20]. It has a diameter of 530 kilometers and a mass of 2.67×10^{20} kilograms with an irregular shape and rough surface [21].

Applying the blinking technique to the images that our supervisor Asst. Prof. Fabrizio Pinto provided using a Cannon 5000D, we re-detected the asteroid Vesta using the software ASTAP. Two images of the night sky have been captured on the 19th and 20th of April 2021 and processed through Astrometry.net. Fig. 7 is the night sky captured in 19th of April at $21:00:06$ UT time and the asteroids are annotated. The coordinates measured in ASTAP gave an average uncertainty of $0,000225259$ and $-7,63962 \times 10^5$ in right ascension and declination respectively, compared to Stellarium data.

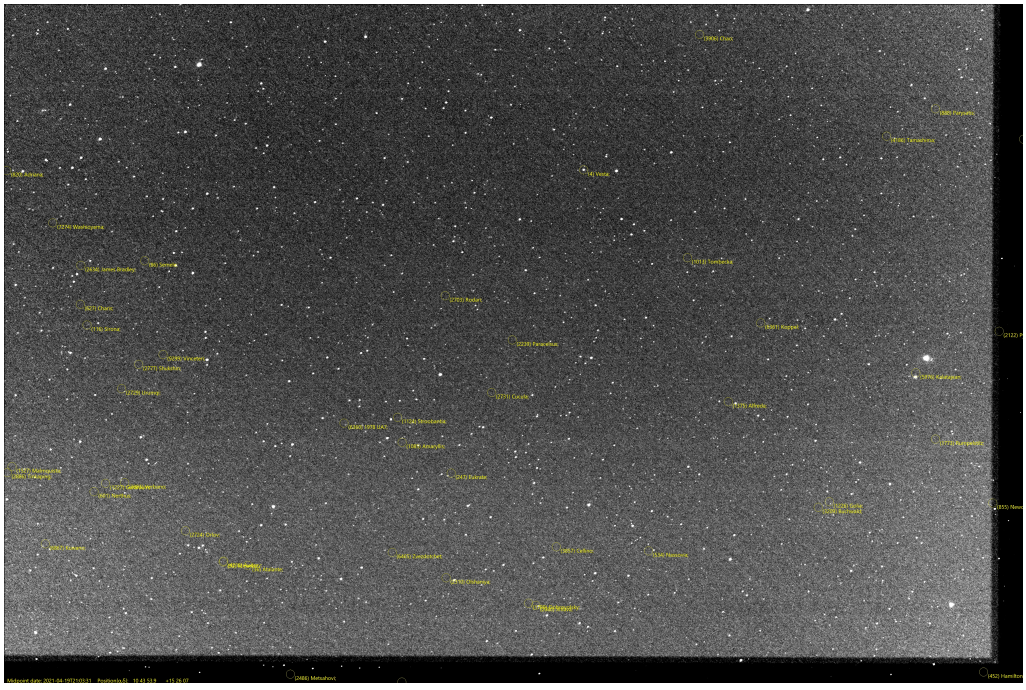

Figure 7: ASTAP frame of April 19th with detected asteroids. (courtesy Fabrizio Pinto)

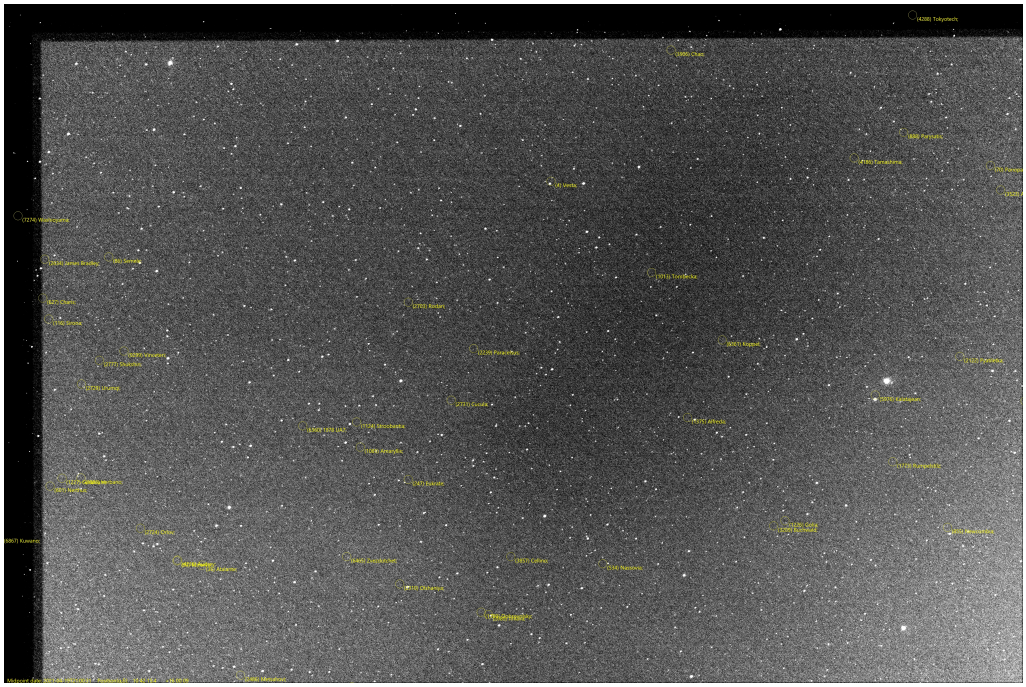

Figure 8: ASTAP frame of April 20th with detected asteroids. (courtesy Fabrizio Pinto)

The same procedure was applied to the image taken on the 20th of April (Fig. 8). The coordinates measured in ASTAP for the 20th of April image resulted in an average uncertainty of 0, 00023639 and −0, 0001067 respectively. Although, the photographs look tilted after turning them into monochromatic form, and they contain pure black parts, ASTAP still provided the features laid in that part and solved the image with a 0.0 offset. Therefore, the error between the ASTAP measurements and the real data from Stellarium is incredibly small as shown in the tables above which proves that ASTAP is a very satisfactory tool for image stacking and solving. Comparing the declination values obtained from Stellarium, we can clearly see that Vesta moved from +18°32′05.8″ to +18°29′35.4″ which corresponds to 0.041777 degrees of difference [22].

Later on, we measured the apparent magnitudes of a stellar field in a specified frame of an image. 58 stars were chosen and investigated through ASTAP and Stellarium. Also, studied the variable star β Lyræ for four different frames, and its variation in magnitude is observed. The average percent errors and differences between the two values were calculated considering the provided Stellarium magnitudes and the measured magnitudes. Finally, both magnitude values are plotted in gnuplot for further investigation.

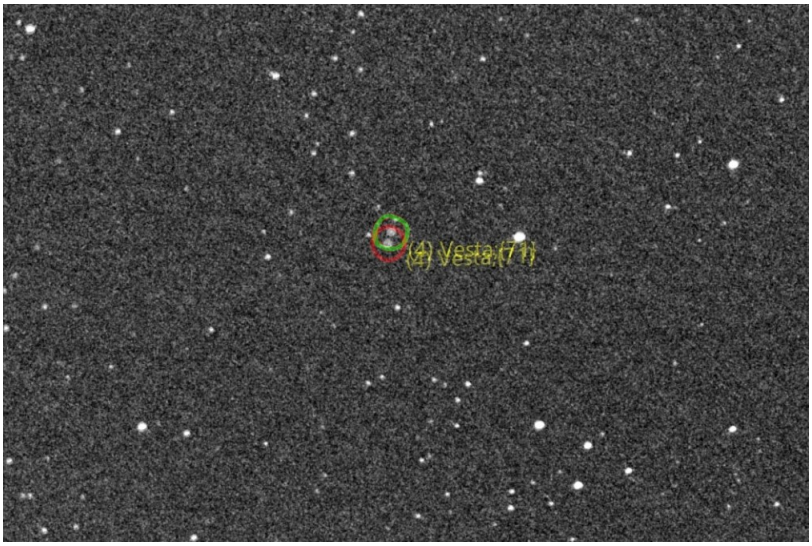

Figure 9: Overlapped photo to observe Vesta's movement (courtesy Fabrizio Pinto)

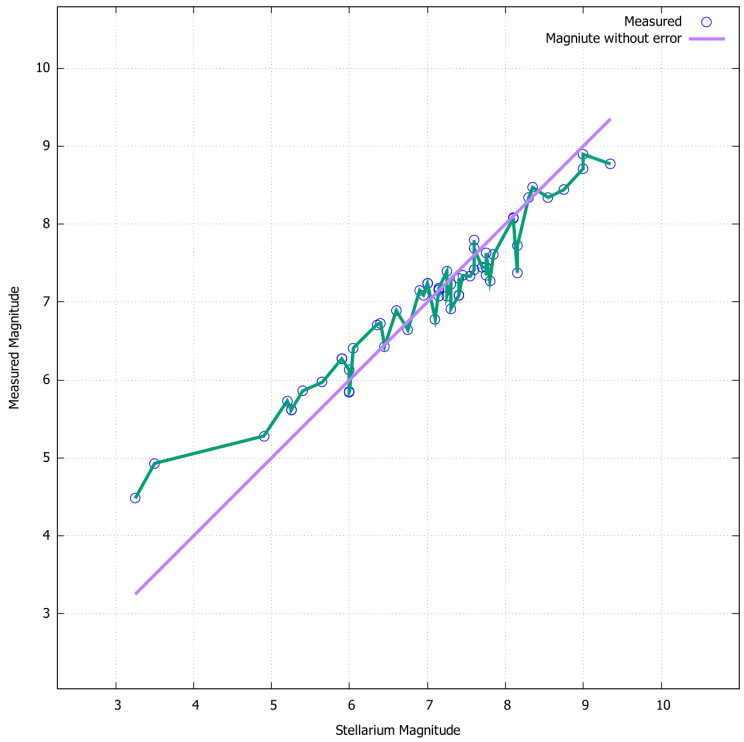

Figure 10: Magnitudes obtained from Stellarium vs ASTAP.

Above Fig. 10 shows the magnitude values obtained from Stellarium versus the magnitude values measured on ASTAP. The purple line indicates the apparent magnitude value without any errors, which is the case of ASTAP measurements assumed to be the same with Stellarium values. The green line demonstrates the measured ASTAP magnitudes with the corresponding values indicated with blue dots. As the graph displays, stars with larger magnitude values resulted in minor errors comparing the stars with less magnitude. In other words, the greatest errors occurred in the measurement of brighter stars, whereas the dimmer ones ended up being more accurate in terms of the measurement of apparent magnitudes.

The average percent error in magnitude and the average difference in magnitude values are calculated as 4.82% and 0.28 respectively. According to Fig. 11, the highest errors occurred in the measurement of the brighter stars, more precisely in our interest, β Lyræ. ASTAP solver shows less accuracy in measuring brighter stars yet respectively higher accuracy in dimmer ones. Although there are some genuinely correct measured stars still, this method does not appear to be a satisfactory approximation to the Stellarium data. The main reason, however, is the difficulty in distinguishing and processing brighter pixels compared to dimmer ones since they may appear more subtle [23].

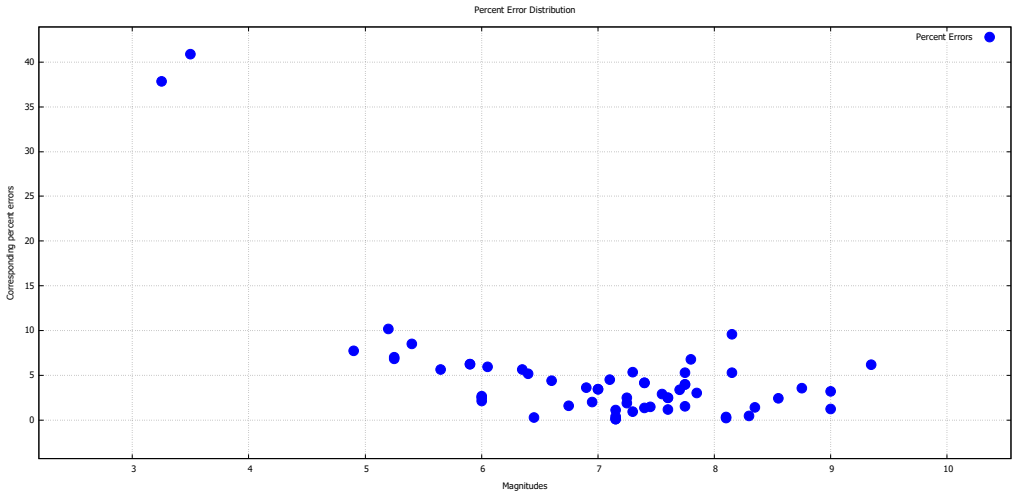

Figure 11: Percent error distribution.

Another crucial parameter is the B-V color index of the star, and it plays a proper role in a star's magnitude. Brighter stars emit more energy, therefore, are hotter than the dimmer ones. If the color indices of two stars are the same and one of them is brighter, this shows that it is smaller in radius compared to the other [24]. Cold stars emerge in red color while the hot ones in blue. And if the star is cold, it has a B-V color index close to +2, whereas the hot stars have negative or close to 0 color index [25].

5 CCDs, PSF Method and Synthetic Star Generation

5.1 Charge-coupled Device (CCD)

The position and movement of celestial bodies are determined by angular differences over a certain time. Photographs are used to determine the coordinates of stars and planets. In addition to these photographs, identification is facilitated with the help of a catalog or atlas of other stars in the surrounding area. By defining several stars with coordinates from the Position and Proper Motion Catalogue, at least three reference stars can be obtained to be used to determine the coordinates of the object. Using as many neighboring stars as possible will increase the precision of the coordinates.

A CCD is a small microchip onto which the light collected by the telescope is focused. The microchip is made up of a vast grid of individual light-sensing devices known as pixels. When light falls on the pixels, electrons are released from the atoms in the pixels and the amount of light falling on each pixel is obtained by counting these electrons. The more exposed the CCD camera is to the sky, the more photons fall on it, allowing objects to be viewed farther away than would normally be seen. Keeping CCD cameras at a low temperature minimizes the effects of thermal noise [29]. CCD devices are also widely utilized in consumer electronic products, as well as medical and scientific applications, to create digital images.

5.1.1 Imaging technique

CCD camera exposures are typically several seconds, with intervals between first and second exposures being measured in seconds also. Secondary exposures are created quickly due to the short intervals needed in universal practice. For faint-looking asteroids, the telescope is held at stellar speed by making a series of short exposures to the required area [30]. The resulting star images can be stacked on top of each other to stabilize as a dot view, while asteroid images can be stacked on top of each other to stabilize the stars as a row of dot views. The dot-like sequence for the asteroid location can then be measured from the image. The telescope lens collects the light emitted from the stars at a single point at the focal length which is then found by the projection to the center point of the light beam of the point, where the star is displayed.

- Image calibration

Dark Frames, also known as "thermal frames," are utilized to compensate for the dark current received by the detector. The effects of the electrical charge delivered to the detector before the exposure are removed by bias frames.

If one is utilizing a dark frame scaling approach, they will need to apply a second bias frame. Flat field frames compensate for uneven lighting in the field. Before one attempts to align data frames for stacking, each of the calibration frames must be applied, otherwise the pictures will be altered from their original orientation, resulting in the dark, bias frames, and flat field frames not having the desired impact [31].

• **Dark frames:** Dark frame subtraction is a technique used in digital photography to minimize picture noise in images captured with longer exposure times, high ISO sensor sensitivities, or at high temperatures. It takes the use of two imaging noise components that are constant from shot to shot, dark current and fixed-pattern noise. Heated pixels, which light up brighter than surrounding pixels, are a part of the image sensor noise. The method works by capturing a picture with the shutter closed and then removing it from the original shot with the noise. An image captured with the sensor in complete darkness is known as a dark frame. A dark frame is simply an image of sensor noise. To adjust for fixed-pattern noise, a dark frame, or an average of multiple dark frames, can be removed from succeeding images. Since the brightness of fixed pixel noise is based on both, it's critical for dark frames to be captured at the same ISO sensitivity and exposure period as the original photo. A single dark frame can be removed from several shots taken at these settings, saving time by providing noise reduction for stacked star trail shots that do not permit interruption [31].

• **Bias frames:** A bias frame is an image created from an optoelectronic image sensor with no real exposure time in digital photography. The imagery obtained only comprises undesirable signals related to the electronics that develop the sensor data, not an unwanted signal from carrier concentration within the sensor. A bias frame is similar to a dark frame, which has the same charge integration time as a bias frame but it is dark. Because a dark frame contains unwanted signal such as a repaired noise component, some of which relates to the bias frame and some of which is owing to dark current and is proportional to the exposure period. Subtracting a bias frame from a dark frame yields an image that only represents the dark-current component. When multiplied by a factor based on exposure duration and then added back to the bias frame, the resultant image allows for the creation of an 'artificial' dark frame [31][32].

• **Flat-field frames:** Flat-field correction is a method for improving digital imaging quality. It removes the impacts of visual artifacts produced by differences in the detector's pixel-to-pixel sensitivity and optical path distortions. It's a typical and commonly-used calibration method, from personal digital cameras to huge telescopes. The technique of correcting for varying gains and dark currents in a detector is known as 'flat fielding'. A uniform signal will provide a uniform output once a detector has been flat-fielded properly.

This indicates that any subsequent signals are attributable to the phenomena being discovered rather than a systematic mistake [33]. A flat-field picture is created by imaging an evenly lighted screen, resulting in a color and brightness image that is consistent across the frame. A sheet of paper held at arm's length can serve as a screen for handheld cameras, but a telescope will often photograph a clean area of the sky during twilight when the lighting is consistent and there are few if any, stars seen. Processing can begin after the photos have been obtained. A flat field is made up of two integers for each pixel: gain and dark current (or dark frame). The gain of a pixel is the variation in the quantity of signal provided by the detector as a function of the amount of light (or equivalent). Because the gain is nearly always a linear quantity, it is easily expressed as the ratio of input and output signals. When there is no incident light, the dark current is the amount of signal put out by the detector. This can be a function of time in various detectors; for example, with astronomical telescopes, it is usual to capture a dark frame at the same time as the scheduled light exposure. Using a series of neutral density filters to provide input/output signal information and a least-squares fit to acquire the values for the dark current and gain for optical systems, the gain and dark-frame may also be determined [31].

$$C = \frac{(R - D) \times m}{(F - D)} = (R - D) \times G \tag{25}$$

where C is the corrected image, R is the raw image, F represents the flat-field image, D is the dark field or dark frame, m is the image-averaged value of (F – D) and G is the gain, $G = \frac{m}{(F-D)}$. To obtain a light frame, an astrophotographer must set a light source over the imaging instrument's objective lens, ensuring that the light source is equally distributed through the user's optics. When looking at the histogram of the image, the photographer must change the exposure of their imaging device (CCD) or digital single-lens reflex camera (DSLR) such that a peak reaches roughly 40–70% of the imaging device's dynamic range (maximum range of pixel values). The photographer usually captures 15–20 light frames and uses median stacking to combine them. After obtaining the necessary light frames, the objective lens is covered to prevent light from entering, and 15–20 dark frames of equal exposure are captured. Then, the objective lens is covered to prevent light from entering, and 15–20 dark frames, each with the same exposure duration as the light frames, are shot which are called dark-flat frames [31]. D. Jacobsen (2016) provides a list of actions to summarize the calibration procedure [31],

1. Acquire data frames,
2. Acquire dark frames,
3. Acquire bias frames if using scalable darks,
4. Acquire flat-field frames,
5. Acquire dark frames for flat field frames of the same exposure time as flat-field frames,
6. Create master dark frames,
   a. For master dark frames of the same exposure time as the data frames, make a median combined master dark frame.
   b. If using scalable darks,
   I. First, create a master bias frame by median combining the individual bias frames,
   II. Subtract the master bias from each dark frame,
   III. Median combine all dark frames to create a scalable dark frame.
7. Create master flat-field frames,
   a. Median combines the matching dark frames to create a master flat-field dark frame,
   b. Subtract the master flat-field dark frame from each of the individual flat-field frames,
   c. Median combine all calibrated flat-field frames to create a master flat-field frame.
8. Apply the master bias frames created in step 6bI above to each data frame if using scalable dark frames,
9. Apply master dark frames to each data frame,
10. Apply the master flat field to each data frame,
11. Align all data frames,
12. Stack data frames by adding, averaging, median combining,
13. Perform final image processing.

- Calibration of RGB data: The processes for calibrating raw RGB or LRGB data frames are almost identical to those for monochrome photos. If scalable dark frames are utilized (a reason to generate scaled dark frames) or if each of the sub-exposure times via the appropriate color filter is similar, the dark and bias master frames can be used for each color set. Otherwise, a distinct set of dark frames are needed for each of the sub-frame sets for each color filter and each exposure duration. If you're using LRGB, you'll need to make a distinct set of master flat-field frames for each color and the luminance frame [31].

5.1.2 Synthetic CCD-frame generation, Point Spread Function (PSF) and centroiding

The framed pages below are generated from the Jupyter Notebook provided by our supervisor Asst. Prof. Fabrizio Pinto, which includes Mathematica codes for synthetic CCD-frame generation, Point Spread Function (PSF) and centroiding [26]. Below notebook introduces a simulation of a star image using the Point Spread Function (PSF). The images generated by a point light source spreads to several pixels, therefore differs from their original shape. In other words, it develops a diffused image from a single point light source. It is an aspect of optical systems and generated by a Point Spread Function (PSF) in the below notebook [28].

It is examined in detail by passing through many sources of telescopes that make sky surveys over the world. While examining the images obtained from the telescope, the necessary and ideal conditions may not be provided due to the turbulence events caused in the atmosphere, visual noises and the problems due the telescope mechanisms. In order to reach the original state of the images, a system called adaptive optics is utilized which allows to correct and filter out the distorted images. Another purpose of adaptive optics is to determine the position of the stars and the surrounding objects by taking that star as a reference [34].

Various mathematical methods can be applied to minimize the image distortions. With Gaussian pattern matching, the center of mass of the reference star is calculated which can also be supported by the Kalman Filtering method. The most common and the most effective method used so far in finding the center of mass of a star is Point Spread Function (PSF). To date, Point Spread Function (PSF) has been used to improve and finalize previously acquired images.

fabrizio-pinto-feng-group-1-PSF

May 29, 2022

1 Synthetic CCD-frame generation, Point Spread Function (PSF) and centroiding

Fabrizio Pinto

1.1 Natural constants

[1]:
```
cLight = 2.997925 10^8 ;
hBar = 1.054 10^(-34) ;
```

1.2 Flux calibration

Assume an arbitrary number of photons striking an infinite sensor during the exposure time

[3]:
```
NTotalPhotons = 10^7;
```

1.3 Point Spread Function (PSF)

[4]:
```
PSF[xcmth01_, ycmth01_, x_, y_, Gammax_, Gammay_] = Exp[-(((x - xcmth01)^2)/((2␣
 ↪Gammax)^2))- (((y -ycmth01)^2)/((2 Gammay)^2))]
```

[4]:
```
                      2       2                2          2
 -(1/4) (x - xcmth01) /Gammax  - (y - ycmth01) /(4 Gammay )
E
```

[6]:
```
PLOT3D1 = Plot3D [PSF[50, 50, x, y, 15, 15],{x,1,100},{y,1,100},PlotRange->All,
 ColorFunction -> Function[{x, y, z}, Hue[.65 (1 - z)]],PlotPoints->{200,200}]
```

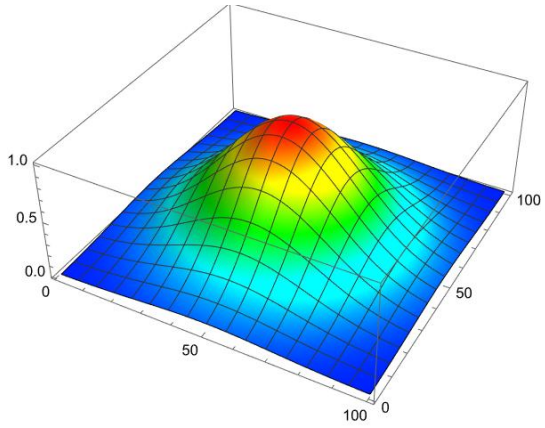

We now integrate over the entire plane to obtain the normalization constant corresponding to the total number of photons:

[8]:
```
PSFInt[xcmth01_, ycmth01_, Gammax_, Gammay_] := NIntegrate[
 PSF[xcmth01, ycmth01, x, y, Gammax, Gammay], {x, -\[Infinity], \[Infinity]},␣
 ↪{y, -\[Infinity], \[Infinity]},
 Method -> {"GlobalAdaptive", "MaxErrorIncreases" -> 10000,
   Method -> "GaussKronrodRule"}, MaxRecursion -> 20,
 WorkingPrecision -> 18]
```

Creating a particular case as $(50, 50)$ is the coordinates of the centroid, and $(15, 15)$ is the spread of the function.

[10]:
```
PSFInt[50, 50, 15, 15]
```

[10]:
```
2827.43338820896789
```

The caibration constant can be written as:

[11]:
```
Intensity0 [xcmth01_, ycmth01_, Gammax_, Gammay_]:= NTotalPhotons/
 ↪PSFInt[xcmth01, ycmth01, Gammax, Gammay]
```

Then, we calibrate by defining the intensity based on the number of photons that we are assuming are being hit.

The calculation is numerically more effective if specific values are chosen:

[13]:
```
Int0 = Intensity0 [50, 50, 15, 15]
```

[13]:
```
3536.77651318055642
```

We can now check that the integral over the infinite plane yields back the total number of photons.

[14]:
```
CCDIntensity [x_, y_]:= Int0 PSF[50, 50,x, y, 15,15]
```

[15]:
```
CCDIntensity [1, 1]
```

[15]: 17.0374769860012622

[16]:
```
Plot3D [CCDIntensity[x, y],{x,1,100},{y,1,100},PlotRange->All,
 ColorFunction -> Function[{x, y, z}, Hue[.65 (1 - z)]],PlotPoints->{200,200}]
```

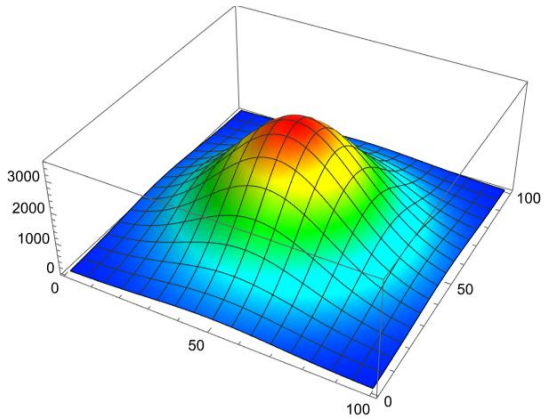

[17]:
```
PLOT1 = Plot3D [CCDIntensity[x, y],{x,21,80},{y,21,80},PlotRange->All,
 ColorFunction -> Function[{x, y, z}, Hue[.65 (1 - z)]],PlotPoints->{200,200}]
```

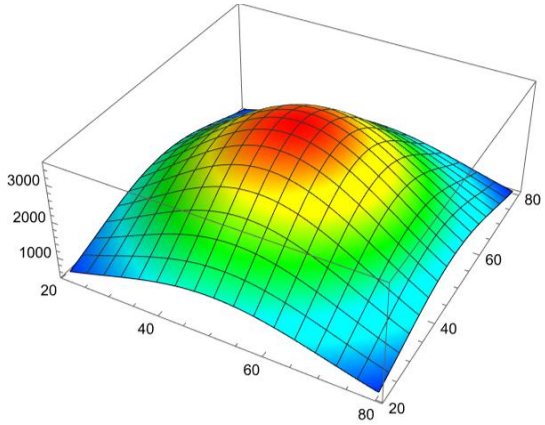

Now, we have this function which describes an artificial star which is centered in the field. And, assuming that each of the squares on the plot are pixels, although it cannot be true since they are not separated by unit length. What needs to be investigated is the amount of radiation that is going through each of those squares, which we can calculate as a continuous number, yet still won't be enough since the number of photons is not a real number but an integer. And, it is also managed by Poisson distribution which generates random numbers out of that distribution. But still, the average output would give the expected result with the given intensity.

[14]:
```
NIntegrate[ CCDIntensity[x, y], {x, -\[Infinity], \[Infinity]}, {y,␣
↪-\[Infinity], \[Infinity]},
Method -> {"GlobalAdaptive", "MaxErrorIncreases" -> 10000,
  Method -> "GaussKronrodRule"}, MaxRecursion -> 20,
WorkingPrecision -> 18]
```

[14]:
```
                        7
1.00000000000000000 10
```

1.4 Synthetic count (ADU) per pixel

Now we shall populate every pixel with a number of photons randomly extracted from a Poisson distribution consistent with the chosen PSF. For example, we calculate the expected number of photons, which must be rounded to an integer:

[21]:
```
Round[NIntegrate[CCDIntensity[x, y], {x, 70, 71}, {y, 50, 51}]]
```

[21]: 2216

We are integrating between $x = 70$, $x = 71$, and $y = 50$, $y = 51$. We are calculating the number of photons that falls into that square, which came out as 2216. This result is the expected value based on the intensity of the CCD.

Drawing from a Poisson distribution (check that clicking in the cell you get different, pseudorandom values):

[47]:
```
RandomVariate[PoissonDistribution[Round[NIntegrate[CCDIntensity[x, y], {x, 70,␣
↪71}, {y, 50, 51}]]],1][[1]]
```

[47]: 2253

Let us populate a table corresponding to a small square area in the center of a larger CCD sensor:

[54]:
```
xmin = IntegerPart[80] ;
xmax = IntegerPart[180] ;
ymin = IntegerPart[80] ;
ymax = IntegerPart[180] ;

CCDGain = 1.0 ;
```

Since we will writing the results to simulate a TIFF Mono-16 file, we divide the results by 2^{16}:

[59]:
```
2^(16)
```

[59]: 65536

Now, we are creating a table by choosing pixels and calculating the number of photons present in each pixel based on the Poisson distribution.

[72]:
```
OBDspotSyntheticPixels1 =␣
↪Table[RandomVariate[PoissonDistribution[Round[NIntegrate[CCDIntensity[x, y],␣
↪{x, i, i+1}, {y, j, j+1}]]],1][[1]]/(2^(16)),  {j, 21, 80}, {i, 21, 80}];
```

[73]:
```
OBDspotSyntheticImage1 = Image[OBDspotSyntheticPixels1]
```

It is the 3x3, 16 bit picture which is going to be filled with a synthetic star.

[74]:
```
xmin = 1
xmax = ImageDimensions[OBDspotSyntheticImage1][[1]]
ymin = 1
ymax = ImageDimensions[OBDspotSyntheticImage1][[2]]
Max[ImageData[OBDspotSyntheticImage1][[ymin ;; ymax, xmin ;; xmax ]]]
```

[74]:
```
1
60
1
60
0.0555878
```

[79]:
```
PixelThreshold = 0.0 ;
```

[80]:
```
OBDspotSyntheticImageRenorm1 =␣
↪ListContourPlot[ImageData[OBDspotSyntheticImage1][[ymin ;; ymax, xmin ;; xmax␣
↪]]/
  Max[ImageData[OBDspotSyntheticImage1][[ymin ;; ymax, xmin ;; xmax ]]],␣
↪Contours -> Automatic, ContourStyle -> Black,
 ContourShading -> None, InterpolationOrder -> None, PlotRange -> {Full, Full,␣
↪{PixelThreshold, 1.0}}]
```

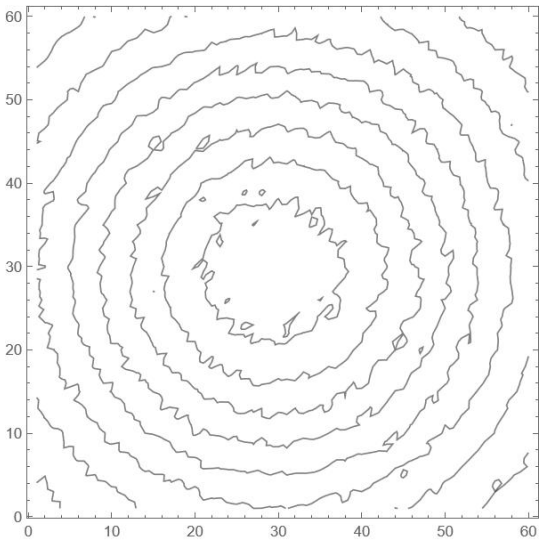

[90]:
```
OBDScience1DP = ListDensityPlot[ImageData[OBDspotSyntheticImage1][[ymin ;; ymax,␣
↪xmin ;; xmax ]]/1, InterpolationOrder -> None, ColorFunction -> GrayLevel,␣
↪PlotRange -> {Full, Full, {0. PixelThreshold  N[(2^12 - 1)/(2^16 - 1)], 1.0␣
↪N[(2^12 - 1)/(2^16 - 1)]}}]
```

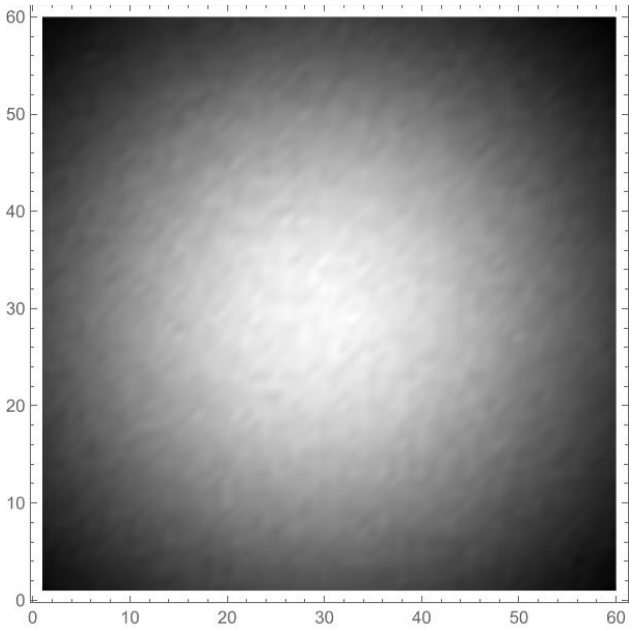

The plot of the star.

[92]:
```
OBDspotxCross = ListPlot[ImageData[OBDspotSyntheticImage1][[50, xmin ;; xmax ]],␣
↪PlotRange -> All]
```

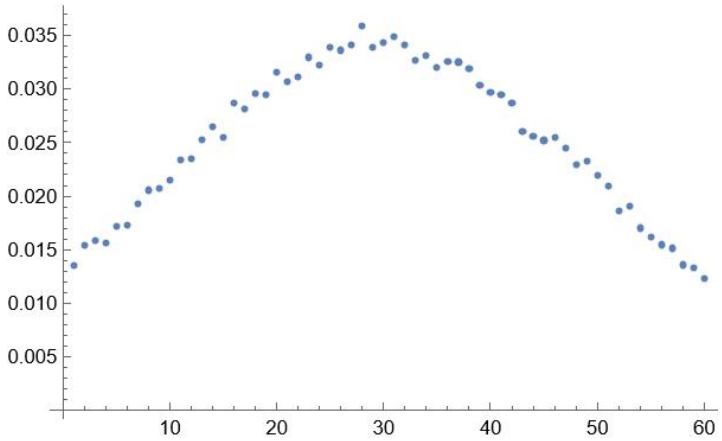

[94]:
```
OBDspotxCross2 = ListPlot3D[ImageData[OBDspotSyntheticImage1][[ymin ;; ymax,␣
↪xmin ;; xmax ]], PlotRange -> All, ColorFunction -> Function[{x, y, z}, Hue[.
↪65 (1 - z)]]]
```

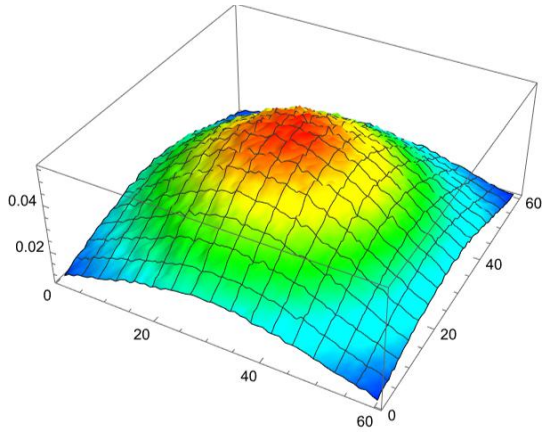

[96]:
```
PLOTALL = GraphicsRow[{PLOT1,OBDspotxCross2}]
```

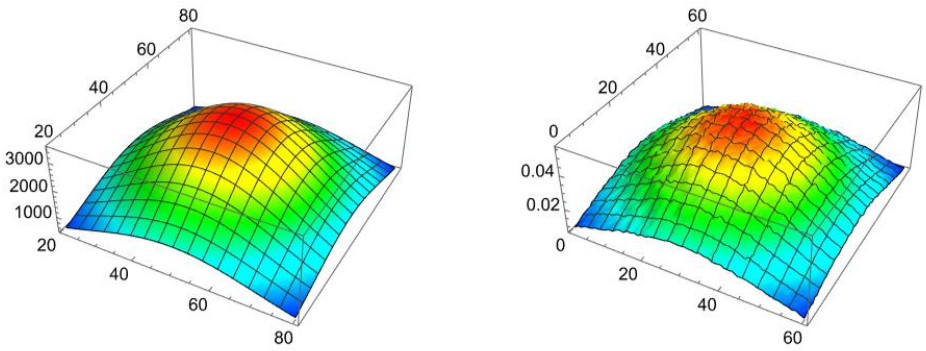

The graph on the left hand side displays the ideal image of the star came out from the ideal distribution of the PSF based on statistics. But, the CCD image produces the one we see on the right hand side with integer numbers and not continuous a function. And, the center of the star produced by the CCD needs to be corrected to the ideal one, meaning that the content of each of these squares should be a random quantitiy with an average equal to what it is determined by the graph on the left, which is not a trivial task since there are such challenges as: the number of bits of the camera, thermal noise, bias and the vibration of the spacecraft itself which may disturb the process.

During sky photography, a small amount of light reaches the camera lens. Therefore, the lens needs to be exposed to more light in order to obtain clearer images. A determined part of the sky needs to be photographed several times with a CCD camera within a certain period of time. During this process, the rotation of the earth must be taken into account and the surface telescope must be positioned accordingly. The images obtained from the telescope must be filtered from atmospheric turbulence, CCD interference, and distortions from the telescope mechanism, regardless of the telescope position. Although, the biggest cause of disturbances is usually atmospheric turbulence. Depending on the telescope's position on Earth, not only atmospheric turbulence but even light from nearby sources can cause distortions. In the images obtained from the telescope with the CCD detector, the dark parts include more noise while the CCD needs to make a long exposure in order to get the best quality shots. The mechanism problems of the telescope are caused by factors such as temperature, wind and precipitation. These are somehow manageable, but the methods for atmospheric turbulence effects are different. Point Spread Function (PSF) comes first among these methods. The distortions in the obtained images can be characterized by the Point Spread Function (PSF) method written as [34],

$$\mu(x, y) = \frac{1}{2\pi\delta} \exp\left[- \frac{(x - X)^2 + (y - Y)^2}{2\delta^2} \right] \tag{26}$$

where δ is the standard deviation and the X and Y values are the coordinates of the center point with the highest value. The image of the same section of the sky is obtained within a certain period of time and these images are used for testing purposes and the resulting Point Spread Function (PSF) is then calculated as a model function. Although the approximate Point Spread Function (PSF) calculation takes a bit of time, this is done only for the reference star and then used to calculate the position of the other stars. The star to be referenced for this calculation is very important. It should be a star that the CCD can detect in the best way and its brightness is as high as possible. If the required brightness is not available, calculations may give incorrect results due to excess noise. If there are more than a dozen stars in the sky section that is imaged as a reference, the desired conditions can be easily met and even automatically realized [34].

5.2 Synthetic asteroid generation

(Further details for this section is publicly available at Ref. [26])

The celestial coordinates of the asteroid Hygiea as seen from the spacecraft which the calculation is introduced in Sec. 7.5.1, is entered into SIMBAD as shown in Fig. 12 below.

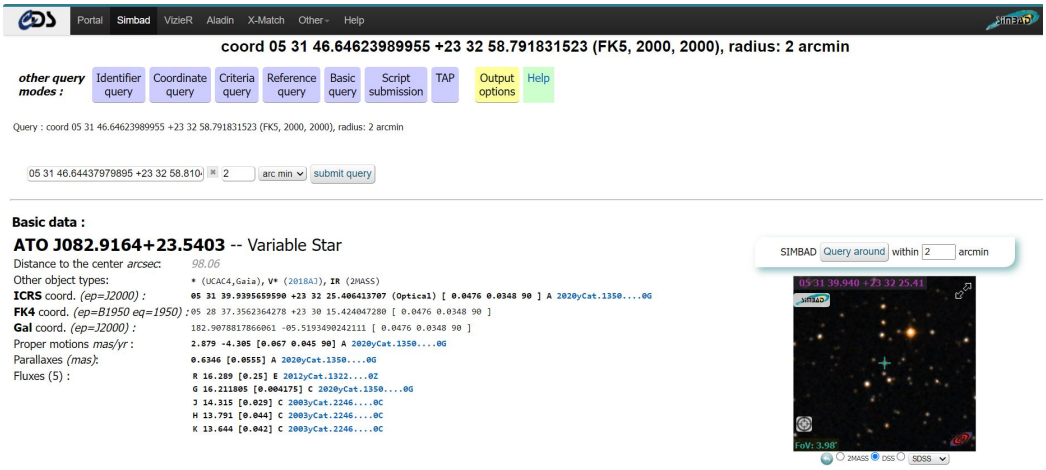

Figure 12: Simbad interface

SIMBAD provides the image of the corresponding frame in the sky where the synthetic asteroid needs to be placed, which is provided by colleague Nida Ocak from the Physics department. She generates the stellar view on SIMBAD, using the celestial coordinates that we provided. The image developed by SIMBAD is then imported into Jupyter Notebook to be overlapped with the synthetic asteroid image which was produced by making the assumption of 10^6 photons striking an infinite sensor during the exposure time where a number of photons randomly extracted from a Poisson distribution consistent with the chosen Point Spread Function (PSF). So by layering the synthetic asteroid image with the one that was obtained from SIMBAD, the fake asteroid is playacted to be in that frame. Hence, for a better accuracy, developing this pretend asteroid for three different time slots is going to allow us to target and apply the optical navigation procedure itself.

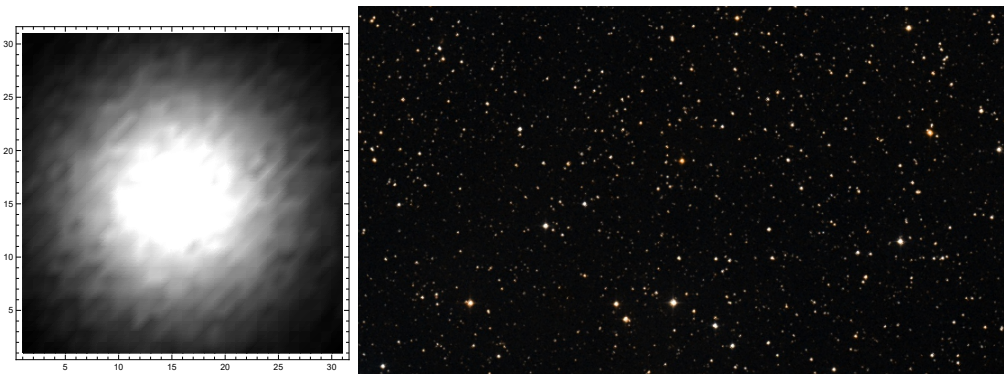

Figure 13: Synthetic star and stellar field [26].

6 Asteroid Detection and Orbit Determination

6.1 Detection of the asteroid 10 Hygiea

Similar to what we have mentioned before in Sec. 4.4.1, another astrometry activity was conducted on a more recent night sky observation, with the intention of studying the motion of the asteroid 10 Hygiea, and calculating its orbital elements. Below Fig. 14, 15 and 16 are captured and provided by Dr. Pinto on April 13th, 14th and 15th, 2022. Photographs were calibrated using ASTAP and processed with Astrometry.net to obtain the calibration information which can be tabulated as follows,

Table 1: April 13th, 14th and 15th, 2022, Astrometry.net calibration information

	April 13th	April 14th	April 15th
Center (Ra, Dec)	(216.650, -18.867)	(215.980, -19.603)	(216.691, -19.482)
Center (RA, hms)	14h 26m 35.884s	14h 23m 55.197s	14h 26m 45.798s
Center (Dec, dms)	-18° 52’ 00.354"	-19° 36’ 11.223"	-19° 28’ 56.592"
Size	8.49 x 6.1 deg	8.28 x 6.15 deg	8.29 x 6.05 deg
Radius	5.228 deg	5.156 deg	5.133 deg
Pixel scale	7.11 arcsec/pixel	7.06 arcsec/pixel	7.05 arcsec/pixel
Orientation	Up is 170 degrees E of N	Up is 183 degrees E of N	Up is 186 degrees E of N

Figure 14: Raw ASTAP frame of April 13th, 2022. (courtesy Fabrizio Pinto [27])

Figure 15: Raw ASTAP frame of April 14th, 2022. (Fabrizio Pinto [27])

Figure 16: Raw ASTAP frame of April 15th, 2022. (courtesy Fabrizio Pinto [27])

The upload page at http://nova.astrometry.net/upload was utilized to determine the calibration information. After converting the .FITS file to .JPG form via ASTAP, the image turns into an ideal uploadable form to Astrometry.net, to identify the stellar objects in the frame and provide the FOV. Although it accepts .FITS format, it would take way too long for it to process since it is a larger file than a .JPG file.

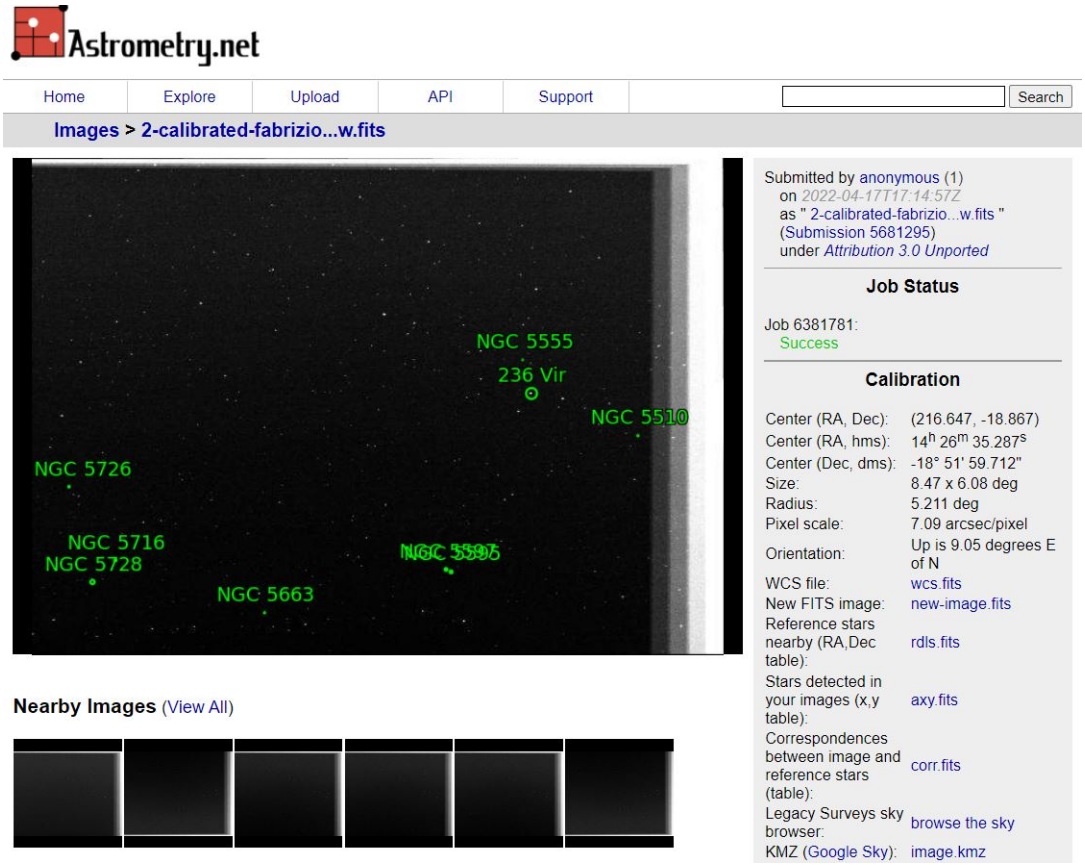

Figure 17: Astrometry.net, results page

Astrometry.net provides the RA/Dec values of the center and field of view size of the image as shown in above Fig. 17, which then to be utilized in ASTAP to solve the image and determine stellar objects. It also provides information about nearby reference stars and the correspondences between the image and the reference stars in .FITS format if needed. Using one astronomical image, Astrometry.net does a great job in producing the orientation, scale, field of view and more to users.

In Fig. 18 below, top left corner of the main page of ASTAP is shown where RA/Dec values of the center of the image obtained from Astrometry.net are entered, α and δ as in right ascension and declination respectively.

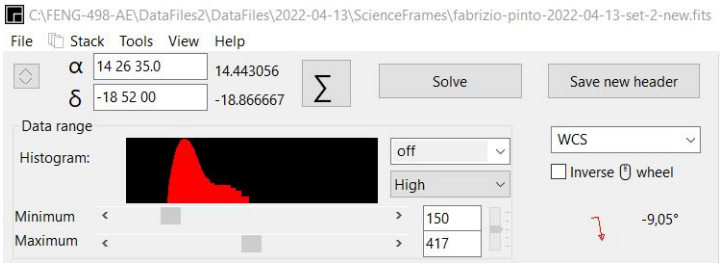

Figure 18: ASTAP, right ascension (α) and declination (δ) values.

Then, going to the section called "Stack" from the top tool bar, we enter the correct alignment information to solve the image. As shown in Fig. 19 below, field of view was obtained from Astrometry.net which is second of the two numbers under the "Size" item. Radius search are is chosen as 20° and H18 star database is used to help ASTAP with many starts for comparison. Finally by clicking "Solve current image", ASTAP solves the image within 0.2 seconds with 0.0″ offset value.

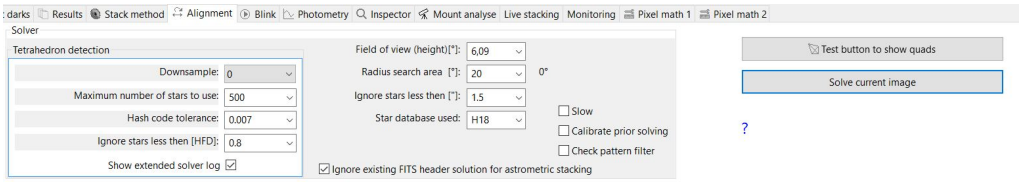

Figure 19: ASTAP, alignment information.

To annotate the stellar objects identified in the field, a large ASCII file called "MPCORB.DAT" is downloaded and entered by going to the section "Tools" and "Asteroid & comet annotation" from the top tool bar as shown in below Fig. 20. Date of observation, obtained as $2022-04-12T23:58:00$ (given in UT time) from the FITS header created after solving process, is entered. Dates of observation for April 14th and 15th are obtained as $2022-04-13T22:56:00$ and $2022-04-14T22:42:00$ respectively. Since FITS header provides the date of observation in UT time, it corresponds to UT+3h in Izmir, Turkey, where the observation was conducted. Finally, the latitude and longitude values of the observation place are entered as 38.3573 and −26.7795 respectively.

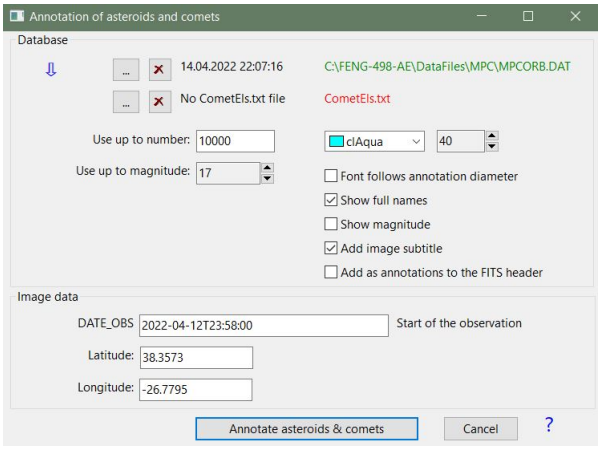

Figure 20: ASTAP, asteroid and comet annotation.

Finally, clicking the annotate button produces the Fig. 21 shown below, which is the main page of ASTAP with the night sky captured on April 13th.

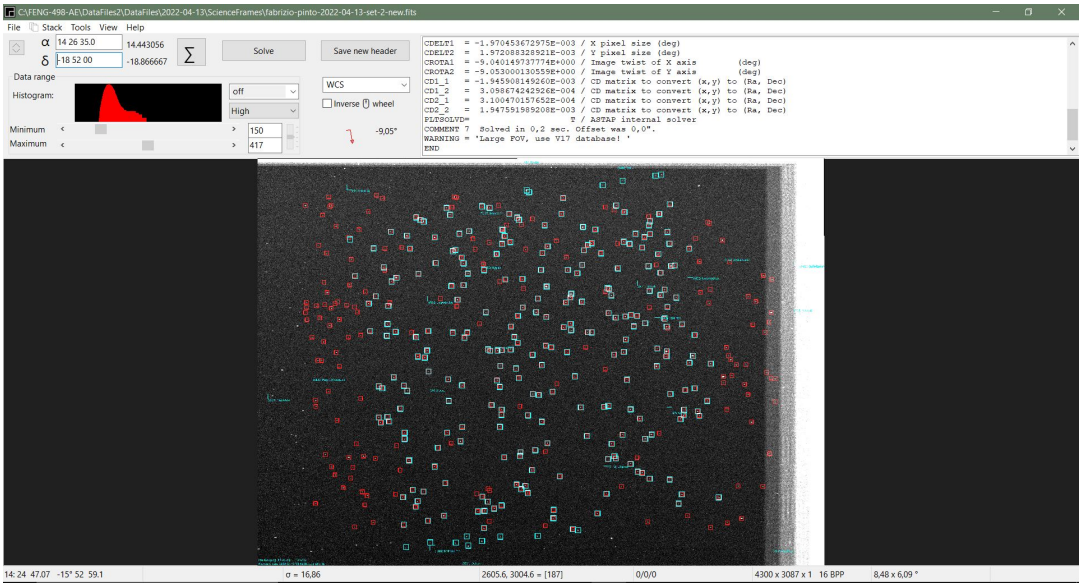

Figure 21: ASTAP, April 13th image solved and annotated.

This whole procedure is also applied to the images captured on April 14th and 15th to calibrate and annotate the stars and asteroids, therefore the blinking method can be conducted to observe the movement of a possible asteriod in the given stellar field. The below Figs. 22, 23 and 24 include the zoomed in view of the asteroid 10 Hygiea, captured on April 13th, 14th and 15th respectively.

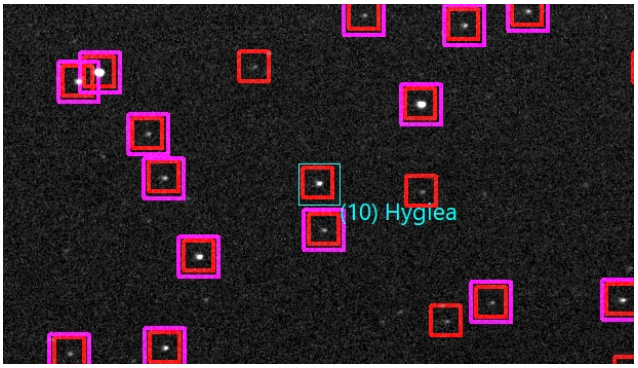

Figure 22: ASTAP frame of April 13th, 2022, with detected asteroids, Hygiea centered. (courtesy Fabrizio Pinto [27])

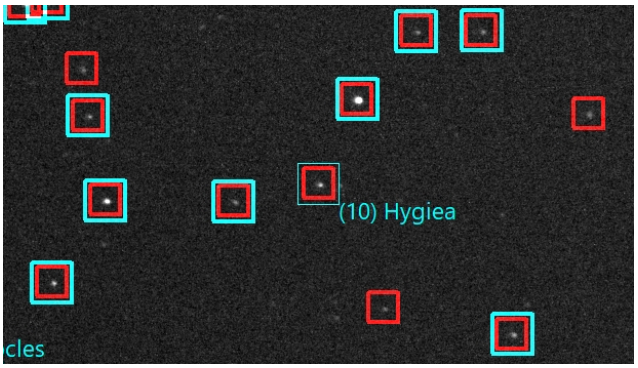

Figure 23: ASTAP frame of April 14th, 2022, with detected asteroids, Hygiea centered. (courtesy Fabrizio Pinto [27])

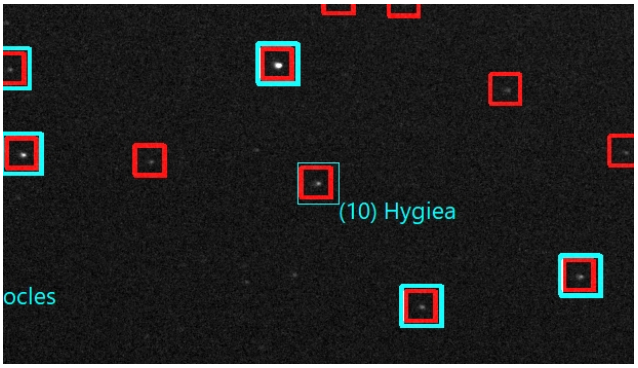

Figure 24: ASTAP frame of April 15th, 2022, with detected asteroids, Hygiea centered. (courtesy Fabrizio Pinto [27])

To measure the RA/Dec values of asteroid, the image was zoomed in to the asteroid Hygiea as much as possible in order to obtain an accurate measurement. The brightest pixel appears at the middle of the scattered pixel view of stars. Hence, putting the cursor onto the brightest pixel gives the center of that object. And, the measurement of the RA/Dec values corresponding to that center is called *centroiding*. Also, measuring the RA/Dec values of fainter surrounding pixels gives us a range of best estimate. Below list shows the center coordinates of Hygiea measured for each day with uncertainties:

- April 13th, RA/Dec (α, δ) = 14h 29m 13.49s ± 1.74 s / −20°26′37.3″ ± 1.9″
- April 14th, RA/Dec (α, δ) = 14h 28m 33.17s ± 2.08 s / −20°23′49.5″ ± 1.9″
- April 15th, RA/Dec (α, δ) = 14h 27m 52.14s ± 1.45 s / −20°20′46.3″ ± 2.6″

Table 2 shows the comparison of the measured RA/Dec values to the real data obtained from Stellarium, including the error between the measurements and the real data in degrees. As the table states, the errors are quite small which allows us to consider these measurements as a success.

Table 2: Comparison of the right ascension and declination values of Hygiea measured on ASTAP and obtained from Stellarium

	RA and Dec			
	ASTAP	**Stellarium**	**Error in RA (deg)**	**Error in Dec (deg)**
13.04.2022	14h 29m 13.49s -20° 26' 37.3"	14h 29m 14.10s -20° 26' 44.7"	$1{,}19645\times10^{-5}$	0,000100754
14.04.2022	14h 28m 33.17s -20° 23' 49.5"	14h 28m 34.49s -20° 23' 55.8"	$2{,}53288\times10^{-5}$	$8{,}57892\times10^{-5}$
15.04.2022	14h 27m 52.14s -20° 20' 46.3"	14h 27m 52.59s -20° 20' 54.0"	$8{,}29611\times10^{-6}$	0,000105168

As mentioned earlier, blinking technique is used to observe if there is any moving object present in the field. To apply, go to "Blink" tab and "Browse" the calibrated .FITS files as shown in Fig. 25 and check them to be aligned while blinking occurs.

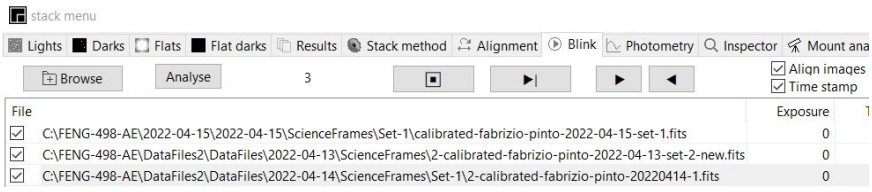

Figure 25: ASTAP, blinking the three images.

Concentrating on the asteroid 10 Hygiea, circled in red and shown in Fig. 26, we can clearly observe its movement from the RA/Dec of 14h 29m 14.10s/−20° 26′ 44.7″ to 14h 28m 34.49s/−20° 23′ 55.8″ in 23 hours, and then to 14h 27m 52.9s/−20° 20′ 54.0″.

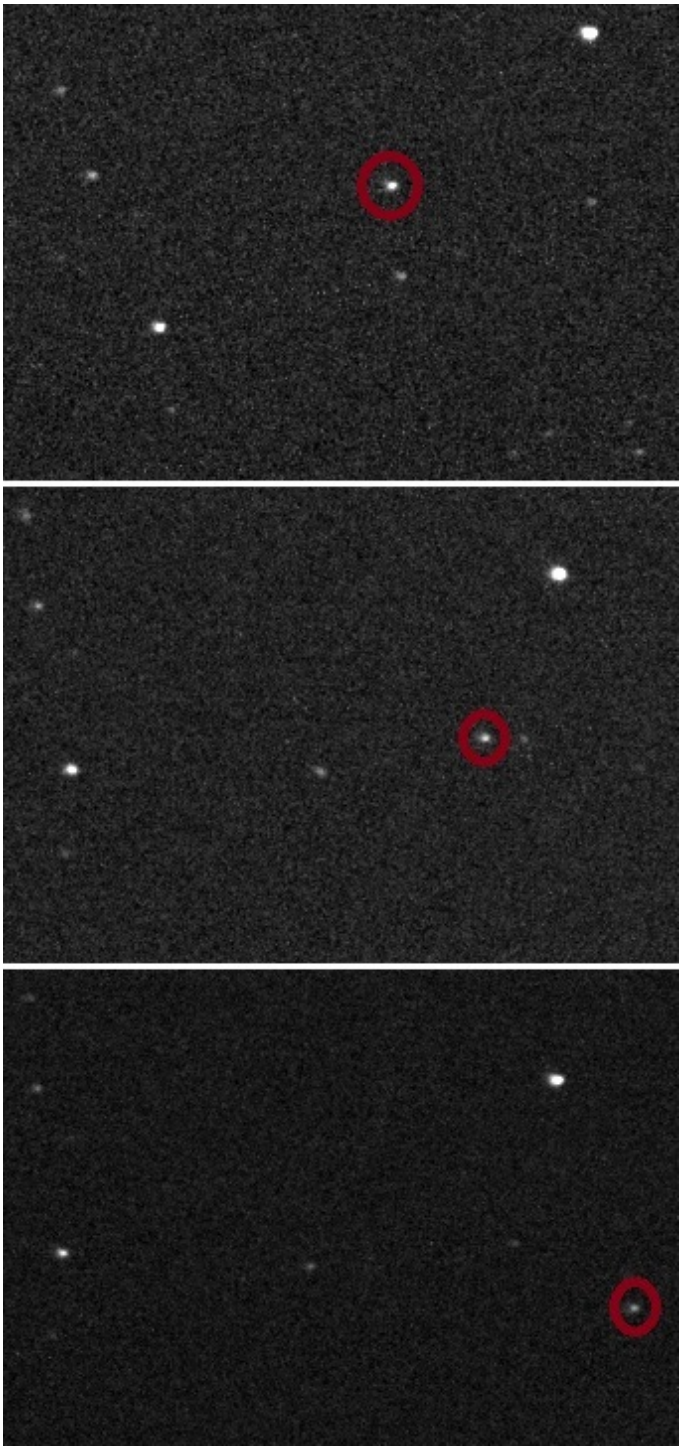

Figure 26: Asteroid 10 Hygiea on April 13th, 14th and 15th [27].

6.2 Orbital elements of the asteroid 10 Hygiea

To calculate the orbital elements of Hygiea, a software called “Find_Orb” is utilized, that is provided by *Project Pluto* which supplies astronomical software, both commercial and freeware, for the use of amateur and professional astronomers. Information regarding the software can be found in the following link: https://www.projectpluto.com/.

Find_Orb calculates the orbital elements with given observational information which are nothing but the right ascension and the declination values of Hygiea that are already been measured and indicated in Table 2. It utilizes the ephemerides provided by NASA JPL. There are several options and the file in the following link is used here: http://andrew-lowe.ca/lnxp1600p2200.405. To make the software obtain an orbit with given information, an ASCII file with a length of 80 characters needs to be created. Detailed information regarding the format for astrometric observations of minor planets is provided by the International Astronomical Union at the following link: https://minorplanetcenter.net//iau/info/ObsFormat.html. Since our observation does not have an International Astronomical Union three letter code, it is designated as 247 and its coordinates must be provided at every line of the ASCII file. This means the observatory device is considered a "rover," that is, an observer not attached to a specific location.

Fig. 27 shows the main page of Find_Orb. To import the ASCII file, go to the option “Select file containing astrometry” and browse the file.

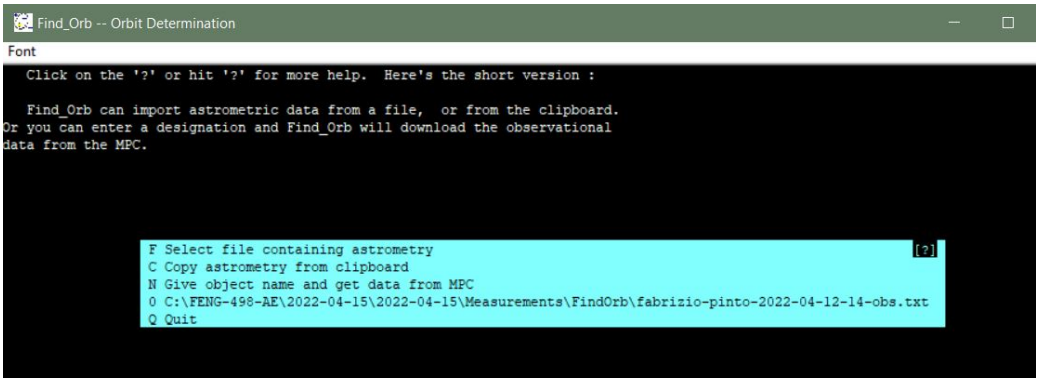

Figure 27: Find_Orb, main page

With the given ASCII file, Find_Orb generates the information shown in Fig. 28 as a .txt file which contains the orbital elements of Hygiea during its revolution around the Sun.

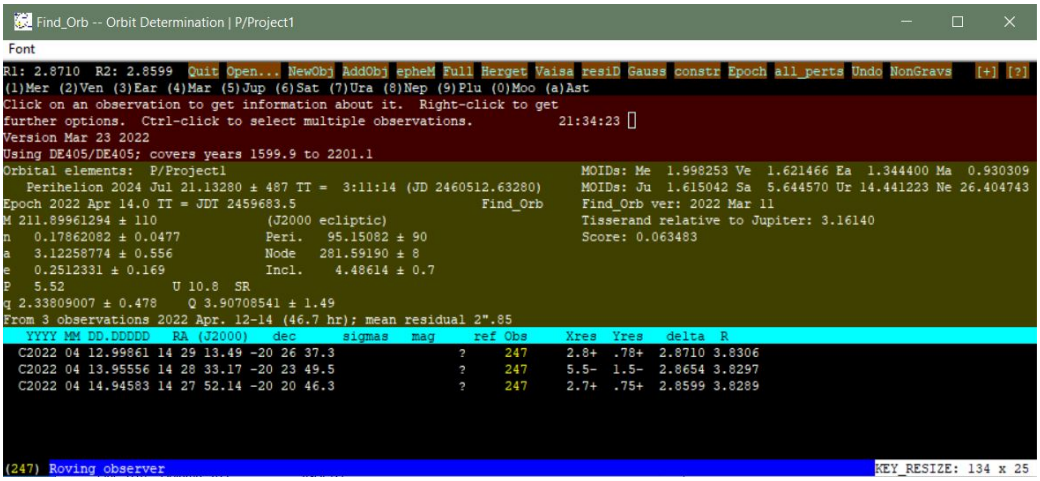

Figure 28: Find_Orb, orbit determination

NASA JPL Small Body Database is used to compare what we have obtained via our calculations with the real data https://ssd.jpl.nasa.gov/tools/sbdb_lookup.html#/?sstr=hygiea.

Table 3: Orbital elements comparison

	Find_Orb	Real Data
eccentricity (e)	0.2512331 ± 0.169	0.11162598
semi-major axis (a)	3.12258774 ± 0.556	3.141867559
perihelion (q)	2.33809007 ± 0.478	2.791153513
inclination (i)	4.48614 ± 0.7	3.830928946
longitude of the ascending node (Ω)	281.59190 ± 8	283.1841897
aragument of perihelion (ω)	95.15082 ± 90	312.493311
mean anomaly (M)	211.89961294 ± 110	328.8968608
period (T)	5.52	5.56916408
mean motion (n)	0.17862082 ± 0.0477	0.176979214
aphelion (Q)	3.90708541 ± 1.49	3.492581605

Considering the uncertainties given in measured data (Find_Orb), most of them fall into the real data range except the aragument of perihelion (ω), mean anomaly (M), and the period (T) with a minimum of 127.342491°, 6.99734786° and 0.04916408 years of error respectively which can be considered relatively small errors acknowledging the fact that only three images with 15 seconds exposure times each were utilized during the process.

7 Centroid pixel coordinate determination and transformation to celestial coordinates

7.1 Photographic Imaging

Introducing the basis of photographic imaging by printing the RA/Dec of a star on the reference plate where the point P shown in Fig. 29 is the imaging point, **F** is the focal length behind the objective, and O represents the center of the camera lens. Considering the coordinate system **u**, **v** and **w**, the vector **e** can be written as [35],

$$\mathbf{e} = \begin{pmatrix} \cos(\delta)\cos(\alpha - \alpha_0) \\ \cos(\delta)\sin(\alpha - \alpha_0) \\ \sin(\delta) \end{pmatrix} \tag{27}$$

which represents the direction of a star located at a RA/Dec (α, δ). Therefore, the vector $\mathbf{e_0}$ is,

$$\mathbf{e_0} = \begin{pmatrix} \cos(\delta_0) \\ 0 \\ \sin(\delta_0) \end{pmatrix} \tag{28}$$

which represents the point (α_0, δ_0) at which the axis of the camera is pointing [35].

The vectors $\mathbf{F} = -\mathrm{F} \cdot \mathbf{e_0}$ and $\mathbf{p} = -\mathrm{p} \cdot \mathbf{e}$ refer to the paths followed by a ray of light from the camera lens to the center of the plate, and to the imaging point P respectively. The angle, φ, in between where,

$$\cos(\varphi) = \mathbf{e_0} \cdot \mathbf{e} = \cos(\delta_0)\cos(\delta)\cos(\alpha - \alpha_0) + \sin(\delta_0)\sin(\delta) \tag{29}$$

Considering the image plane, $\mathbf{e_x}$ and $\mathbf{e_y}$,

$$\mathbf{e_x} = \begin{pmatrix} 0 \\ 1 \\ 0 \end{pmatrix} \quad \text{and} \quad \mathbf{e_y} = \begin{pmatrix} \sin(\delta_0) \\ 0 \\ -\cos(\delta_0) \end{pmatrix} \tag{30}$$

represent a coordinate system on the image plane for measuring the plate which is oriented as North-South and East-West, just like RA/Dec. Recognizing the Standard Coordinates X and Y of point P in terms of the focal length F, **p** can be written as,

$$\mathbf{p} = \mathbf{F} + (\mathrm{F} \cdot \mathrm{X}) \cdot \mathbf{e_X} + (\mathrm{F} \cdot \mathrm{Y}) \cdot \mathbf{e_Y} \tag{31}$$

Combining the equations, we can obtain the relationship between the star's RA/Dec and the coordinates X and Y as,

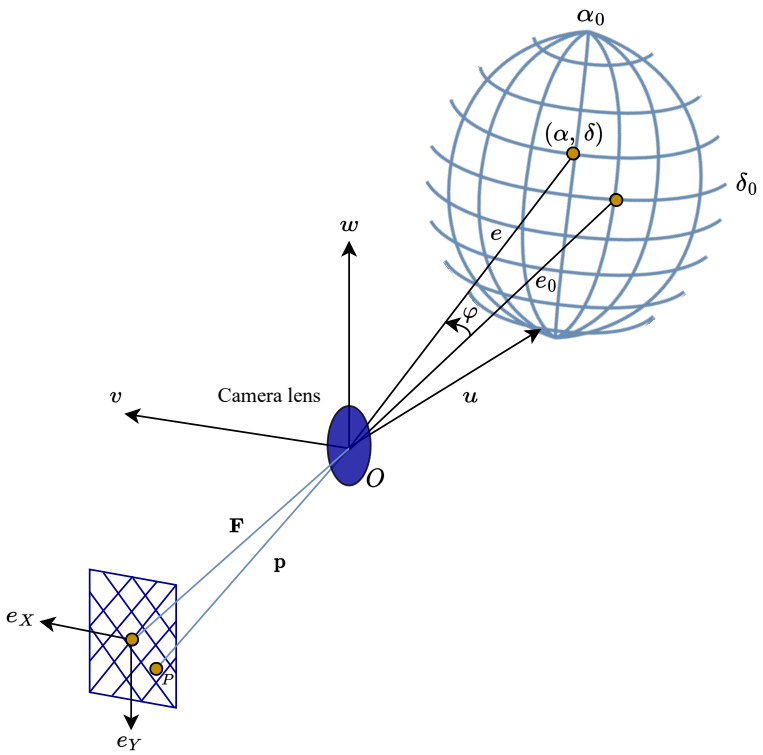

Figure 29: Image formation in photographing a star field, sketched via diagrams.net

$$\begin{aligned} \mathrm{p}\cos(\delta)\cos(\alpha-\alpha_0) &= \mathrm{F}\cos(\delta_0) - \mathrm{FY}\sin(\delta_0) \\ \mathrm{p}\cos(\delta)\sin(\alpha-\alpha_0) &= -\mathrm{FX} \\ \mathrm{p}\sin(\delta) &= \mathrm{F}\sin(\delta_0) + \mathrm{FY}\cos(\delta_0) \end{aligned}$$

where
$\mathrm{p} = |\mathbf{p}| = \mathrm{F}\sqrt{1+\mathrm{X}^2+\mathrm{Y}^2}$
or
$\mathrm{p} = \mathrm{F}/\cos(\varphi) = \mathrm{F}/(\cos(\delta_0)\cos(\delta)\cos(\alpha-\alpha_0) + \sin(\delta_0)\sin(\delta))$.
Finally solving for the spherical coordinates, we determine α, δ as,

$$\alpha = \alpha_0 + \arctan\left(\frac{-\mathrm{X}}{\cos(\delta_0) - \mathrm{Y}\sin(\delta_0)}\right) \tag{32}$$

$$\delta = \arcsin\left(\frac{\sin(\delta_0) + \mathrm{Y}\cos(\delta_0)}{\sqrt{1+\mathrm{X}^2+\mathrm{Y}^2}}\right) \tag{33}$$

Transitioning to $(\alpha, \delta) \rightarrow (\mathrm{X}, \mathrm{Y})$ by taking the inverse,

$$X = -\frac{\cos(\delta)\sin(\alpha - \alpha_0)}{\cos(\delta_0)\cos(\delta)\cos(\alpha - \alpha_0) + \sin(\delta_0)\sin(\delta)} \tag{34}$$

$$Y = -\frac{\sin(\delta_0)\cos(\delta)\cos(\alpha - \alpha_0) - \cos(\delta_0)\sin(\delta)}{\cos(\delta_0)\cos(\delta)\cos(\alpha - \alpha_0) + \sin(\delta_0)\sin(\delta)} \tag{35}$$

which we utilize to solve our direct problem in

7.2 Plate constants

Plate constants are derived by measuring the standard coordinates for at least three reference stars whose RA/Dec are known, hence the Standard Coordinates can be computed. (X, Y) coordinates are positioned according to the coordinate system oriented parallel to the meridian passing through the center [36]. These coordinates are independent coordinates that do not depend on the focal length of the optic. For plate reduction, the (x, y) coordinates must be divided by the focal length. In the case where the origin of the coordinate system does not coincide with the optical axis, it can be matched with the modification created by the equations below [35],

$$X = \frac{x}{F}, \quad Y = \frac{y}{F} \tag{36}$$

$$X = \frac{x}{F} - \frac{\Delta x}{F}, \quad Y = \frac{y}{F} - \frac{\Delta y}{F} \tag{37}$$

Coordinate axes can be rotated by the angle γ, measured relative to the North-South line. The shift that may occur in the coordinate system does not affect the equational relationship between the measured and Standard Coordinates. However, the equations that should be used for possible bending and distortion are,

$$X = \frac{x \cdot \cos(\gamma) - y \cdot \sin(\gamma)}{F} - \frac{\Delta x}{F} \tag{38}$$

$$Y = \frac{x \cdot \sin(\gamma) + y \cdot \cos(\gamma)}{F} - \frac{\Delta y}{F} \tag{39}$$

$$X = a \cdot x + b \cdot y + c \tag{40}$$

$$Y = d \cdot x + e \cdot y + f \tag{41}$$

Six plate constants (a, b, c, d, e, f) are used in the conversion between coordinates [35]. Plate constants are determined using the equatorial coordinates of the predetermining reference stars. When working with a magnification of unknown scale, it is advantageous that the focal length information of the camera optics is not needed. Sec. 7.4.2 below [35].

Coordinate determination can never be completely error-free, so using the maximum number of stars will help to obtain optimum values in this case [37]. Plate constants can be determined by solving two equations with three unknowns and uses the least squares method when the equations cannot be solved any further.

7.3 Sub-pixel centroid coordinate determination

In this section, we introduce the procedure conducted on the Jupyter Notebook provided by our supervisor Dr. Pinto which is publicly available at Ref. [38].

Now, we work on detecting the centroid position of the asteroid Hygiea in the three images. There are two main methods for determining an estimate of the centroid of a star/asteroid: moment analysis and Point Spread Function (PSF) [39], which was briefly introduced in Sec. 5.1.2. Instead, we utilize moment analysis to find the centroid position by calculating the center of mass of the pixels located at the center. Meaning that, the image of a star does not appear as a point but as spread-out pixels, covering some area, which allows us to determine accurate centroiding of sub-pixel level [40]. Whereas, in Point Spread Function (PSF) fitting, a function models the CCD sensor pixels to express the energy flux on the sensor, then the free parameters of the Point Spread Function (PSF) are obtained by best-fitting [34].

7.3.1 Creating a sub-frame

The procedure starts with importing the three images given in Figs. 14, 15 and 16 into Jupyter Notebook. Mathematica does a great job in terms of image adjusting, even supports .FITS files. Initially, the dimensions of each image are extracted to define the size of the palettes in use.

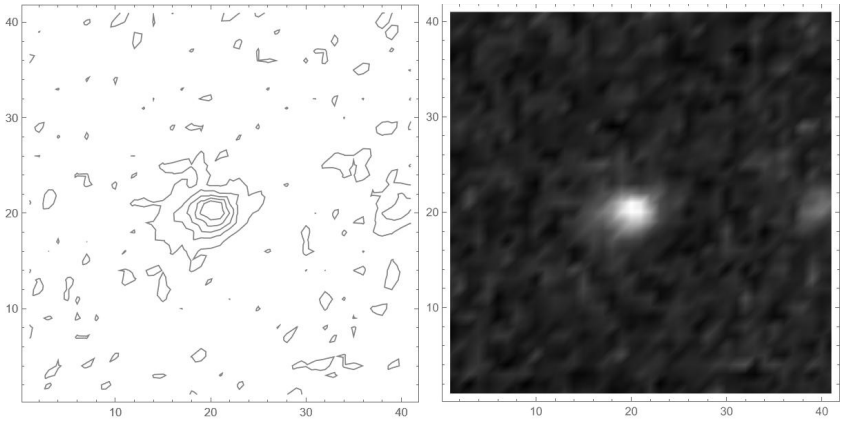

Figure 30: Gray-level and contour sub-frame plots of the image taken on April, 14th.

Since the main focus is the asteroid Hygiea, we want to create a sub-frame with the asteroid centered in it. Then the contour and gray-level plot of the selected sub-frame is obtained as shown in Figs. 28 and 30 for each image. Below Fig. 31, displays the 3D image of the signals covered in that area. The background noise is shown in blue color, and the highest signal in the frame is shown in green, yellow and red color progression which is where the asteroid is located.

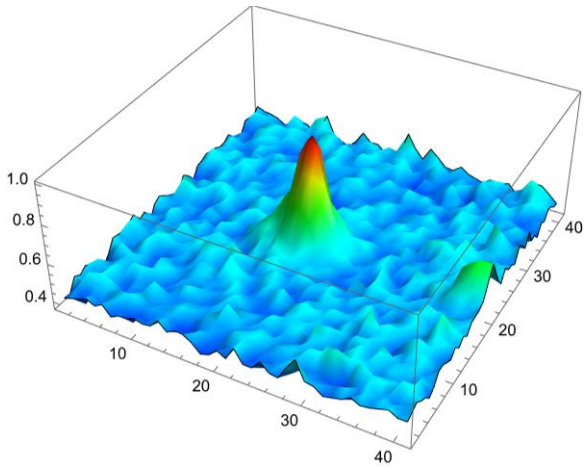

Figure 31: 3D sub-frame plot of the image taken on April, 14th.

A parameter called 'threshold' indicates the fact that there is no pixel without any noise. So, it allows us to eliminate the signals that we do not want to observe and to isolate the image of the asteroid from the background signal created by noise sources. In the 1D plot shown in below Fig. 32, we observe a more stable signal which shows that there is a noisy background, and where the signal peaks, we have the star itself.

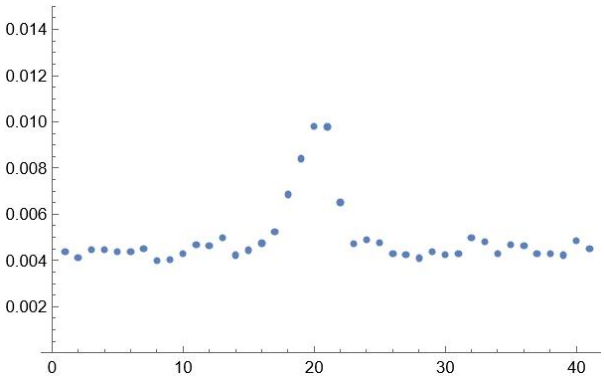

Figure 32: 2D sub-frame plot of the image taken on April, 14th.

7.3.2 Calculating the coordinates of the centroid center of mass (1st moment)

The center of mass can be defined as the point where the weighted relative position of the spread-out mass sums up to zero [41]. The summation of all spread-out mass of the image is,

$$M_{\text{tot}} = \sum_{j,k} M_{jk} \,, \tag{42}$$

where j and k range over all pixel values of the subframe.

The (x, y) coordinates of the center of mass of the centroid of the entire frame are,

$$x_{\text{cm}} = \frac{1}{M_{\text{tot}}} \sum_{j,k} (x_j) M_{jk} \,, \tag{43}$$

$$y_{\text{cm}} = \frac{1}{M_{\text{tot}}} \sum_{j,k} (y_j) M_{jk} \,, \tag{44}$$

where the pixel coordinates are located at the pixel center obtained by subtracting a value of $\frac{1}{2}$.

The uncertainty on the pixel location can be estimated by computing the higher moments of the mass distribution [39],

$$\sigma_x^2 = \sum_{j,k} x_j^2 \, M_{jk} - \frac{1}{M_{\text{tot}}} \left(\sum_{j,k} x_j \, M_{jk} \right)^2 , \tag{45}$$

$$\sigma_y^2 = \sum_{j,k} y_j^2 \, M_{jk} - \frac{1}{M_{\text{tot}}} \left(\sum_{j,k} y_j \, M_{jk} \right)^2 , \tag{46}$$

Then, the whole image's true coordinates of the center of mass can be calculated by adding the corner coordinates of the region of interest, which were previously measured by putting the cursor on an estimated corner. Calculations resulted quite accurately as 1578.11 for x and 1129.98 for y coordinate, which were originally chosen as 1577 and 1129. The uncertainties in x, y coordinates are %0.0704 and %0, 0868 respectively. This calculation was done without any thresholding value, meaning that the background noise was also accounted. The threshold parameter, m_{thr}, can be expressed as,

$$\frac{M_{jk}}{\max\{M_{jk}\}} \geq m_{\text{thr}} \,,$$

If the same calculation is conducted with isolating the star, PixelThreshold = 1.0, we obtain 1577 and 1129 for x and y coordinate respectively which is obviously unrealistic since we only consider the brightest pixel. Fig. 33 shows the centroid position of the asteroid Hygiea on the contour plot.

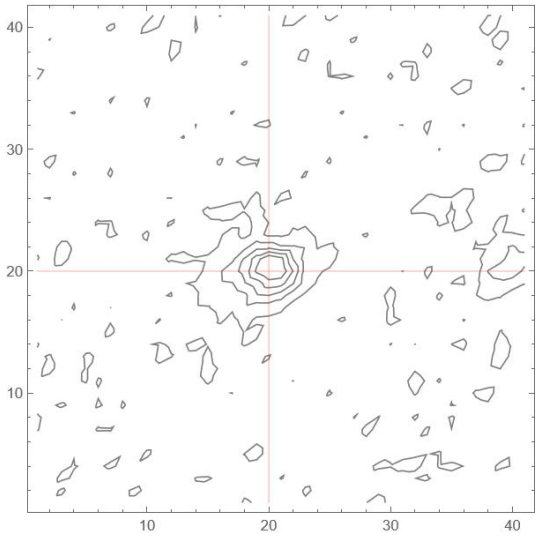

Figure 33: Centroid position of Hygiea on April, 14th.

7.4 From centroid pixel coordinates to celestial coordinates

The main objective is to obtain the celestial coordinates of the centroid using what we have, pixel centroid position, we will make a transition to the celestial coordinates of the centroid in RA/Dec (α, δ), by means of the Plate Constants. The solutions given by Astrometry.net and ASTAP are both considered in this procedure to achieve a better accuracy. Also spherical trigonometry and matrix transformations are used to conduct direct and inverse problems. In our case, the direct problem is defined as transitioning from pixel centroid coordinates to celestial coordinates. Whereas the inverse problem is the opposite, from celestial coordinates to pixel centroid coordinates. Eventually, we would like to obtain the RA/Dec of the spacecraft when all is said and done, using the solution for the inverse problem by transitioning from the celestial coordinates of the asteroid to the sensor frame, which is where the spacecraft is essentially located.

7.4.1 Using Astrometry.net output file

Starting off with the solution given by the Astrometry.net which was computed by using the image taken on April 14th. The extensive log file produces the information given below,

crval = $(214.958, -18.9653)$

crpix = $(2583.8, 1916.74)$

$$\text{CD} = \begin{pmatrix} -0.0019605 & -0.00010009 \\ -9.1251e-05 & 0.0019582 \end{pmatrix}$$

The solution provides two vectors called 'crval' and 'crpix' which represents the (x,y) coordinates of the origin that Astrometry.net chooses to use and RA/Dec of that origin in the real sky respectively. The **CD** matrix indicates the plate constants which describes the transition from the reference frame in pixels in the sky with the origin Astrometry.net chooses.

To conduct the process, we need to introduce three coordinate frames,

1. The sensor reference frame

The sensor reference frame is the the frame that is seen in ASTAP demonstrated by the (X, Y) coordinates. It is assumed that the origin, O_s, of this frame is placed at the top left of the image and its axes are parallel to the sensor main sides where the y-axis aligned downwards. Since the (X, Y) letters generally refer to the Standard Coordinates, we demonstrate the coordinates of the sensor frame by (x, y).

2. The intermediate reference frame

The origin of the intermediate reference frame, O_i with the coordinates of (x_c, y_c) which also correspond to **crpix** vector, located in the O_s frame with the axes parallel to that frame. The coordinates of this frame is demonstrated by (ξ, η). On the other hand, the celestial coordinates of the origin (x_c, y_c) is also indicated by (α_c, δ_c) which corresponds to **crval** vector. To be more clear,

$$x_c = CRPIX1, \quad y_c = CRPIX2$$
$$\alpha_c = CRVAL1, \quad \delta_c = CRVAL2$$

3. The Standard Reference Frame (SRF)

The origin of the SRF is located again at the origin of the intermediate reference frame, $O_{\mathrm{SRF}} = O_i$, with its axes aligned according to the Plate Constants. The celestial coordinates of the origin O_{SRF} are (α_c, δ_c).

- Direct coordinate reference frame transformations

The transformations $O_s \rightarrow O_i$,

$$\xi = x - x_c \ , \tag{47}$$
$$\eta = y - y_c \tag{48}$$

where $\mathbf{r} = (x, y)$ and $\mathbf{w} = (\xi, \eta)$.

Introducing the plate constant matrix:

$$\mathbf{CD} = \begin{pmatrix} CD_{11} & CD_{12} \\ CD_{21} & CD_{22} \end{pmatrix} \tag{49}$$

The transformation $O_i \rightarrow O_{\rm SRF}$ becomes,

$$\mathbf{v} = \begin{pmatrix} X \\ Y \end{pmatrix} = \mathbf{CD}\ \mathbf{w} \tag{50}$$

which can also be expressed as,

$$X = CD_{11}\,\xi + CD_{12}\,\eta\,, \tag{51}$$

$$Y = CD_{21}\,\xi + CD_{22}\,\eta \tag{52}$$

- Inverse coordinate reference frame transformations

The transformation $O_{\rm SRF} \rightarrow O_i$,

$$\mathbf{w} = \mathbf{CD}^{-1}\ \mathbf{v} = \mathbf{CD}^{-1}\ \begin{pmatrix} X \\ Y \end{pmatrix} \tag{53}$$

The transformation $O_i \rightarrow O_s$,

$$x = \xi + x_c\,, \tag{54}$$

$$y = \eta + y_c \tag{55}$$

- Scale factor

The scale factor of the transformation can be calculated by taking the square root of the determinant of the **CD** matrix, which was also provided by the solution given by Astrometry.net.

$$h_{\rm SCp} = |\mathbf{CD}|^{1/2} = 7.06204 \tag{56}$$

- The Standard Reference Frame within the digital image frame

To demonstrate the Standard Reference Frame within the digital image reference frame, we shall solve the equations that will yield to X (where $Y = 0$) and Y (where $X = 0$) axes by using the Eqs. 51 and 52,

Solving for $X = 0$,

$$0 = X = CD_{11}(x - x_c) + CD_{12}(y - y_c)\,, \tag{57}$$

Hence y becomes,

$$y = -\frac{CD_{11}}{CD_{12}}(x - x_c) + y_c \tag{58}$$

Solving for $Y = 0$,

$$0 = Y = CD_{21}(x - x_c) + y_c\,, \tag{59}$$

or,

$$y = -\frac{CD_{21}}{CD_{22}}(x - x_c) + y_c \tag{60}$$

Now, we have the equations to draw the X and Y axes in the image plane as shown in below Fig. 34

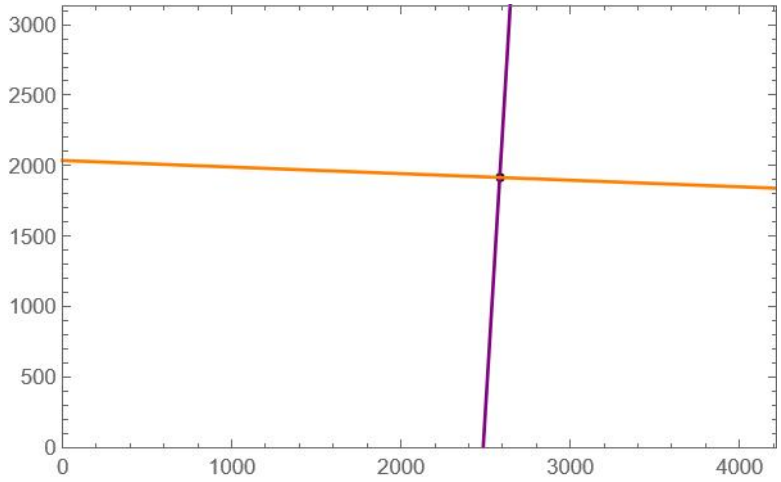

Figure 34: The X and Y axes in the digital image plane

The frame shown above demonstrates only a similar vision of our original image, in other words, this frame may be rotated or reflected in some ways by Astrometry.net. Therefore, it does not demonstrate the image itself. Normally, the X and Y axes should be perpendicular to each other but they look slightly tilted. And, one can calculate the slope of straight lines using the equation,

$$m_Y = -1/m_X$$

where m_Y and m_X are,

$$m_Y = -\frac{CD_{11}}{CD_{12}} \tag{61}$$

$$m_X = -\frac{CD_{21}}{CD_{22}} \tag{62}$$

This requires:

$$-\frac{CD_{11}}{CD_{12}} = +\frac{1}{\frac{CD_{21}}{CD_{22}}} \implies -\frac{CD_{11}}{CD_{12}} = \frac{CD_{22}}{CD_{21}} \implies -\frac{CD_{11}}{CD_{12}}\frac{CD_{21}}{CD_{22}} = 1 \tag{63}$$

Where in our calculation, Eqn. 63 yields to,

$$-\frac{CD_{11}}{CD_{12}}\frac{CD_{21}}{CD_{22}} = 0.91276 \tag{64}$$

Therefore to calculate the angle of rotation of the Y-axis away from the y-axis (vertical sensor axis) and the corresponding angle for the X-axis are, in degrees,

$$\theta_Y = 90^\circ + \arctan \frac{CD_{11}}{CD_{12}} \tag{65}$$

$$\theta_X = \arctan \frac{CD_{21}}{CD_{22}} \tag{66}$$

Above Eqs. 65 and 66 numerically yield to 2.9226° and 2.66802° respectively which proves that these two axes are in fact not perpendicular to each other.

The Eqs. 51 and 52 are approximations of non-linear cases. In other words, we have assumed the relation between the celestial coordinates and the Standard Coordinates is linear. According to R. Buchheim (2007), wide field lenses are affected by field distortions that would demand for more advanced methods to achieve the best fit [42]. Meaning that the axes of the celestial coordinate system may be curves over the plate. Therefore, we need to make the assumption to handle the procedure.

7.4.2 Using the ASTAP best-fit solution

From now on, we are using the best-fit solution provided by ASTAP for the image taken on April 14th, which is more reliable compared to the solution Astrometry.net gives. As shown in Fig. 21, we can see the ASTAP solution on the right-hand corner of the image. Since the two programs do not make the same choices of reference stars, there are differences in signs and certain values. ASTAP stars from the coordinate of the starfield center which Astrometry.net finds blindly. We also use a .JPG file to be solved on Astrometry.net whereas higher quality .FITS file is used in ASTAP which may also create a difference in terms of accuracy.

ASTAP reports:

CRPIX1 = 2.110500000000E+003 / X of reference pixel
CRPIX2 = 1.567500000000E+003 / Y of reference pixel
CRVAL1 = 2.159756776388E+002 / RA of reference pixel (deg)
CRVAL2 = -1.960051075017E+001 / DEC of reference pixel (deg)
CDELT1 = -1.958306637531E-003 / X pixel size (deg)
CDELT2 = 1.959152044370E-003 / Y pixel size (deg)
CROTA1 = 3.135104821469E+000 / Image twist of X axis (deg)
CROTA2 = 3.130121910333E+000 / Image twist of Y axis (deg)
CD11 = -1.955385043129E-003 / CD matrix to convert (x,y) to (Ra, Dec)
CD12 = -1.071472026387E-004 / CD matrix to convert (x,y) to (Ra, Dec)
CD21 = -1.069309109067E-004 / CD matrix to convert (x,y) to (Ra, Dec)
CD22 = 1.956219877704E-003 / CD matrix to convert (x,y) to (Ra, Dec)

Comparing the 'crpix' values, we notice that ASTAP makes different choices for the origin of the Standard Reference Frame. Since both methods use different choices in terms of defining the reference frame, the signs of the plate constant matrix are also different. This usually happens when the image is flipped or reflected, so that the z-axis would come from the right hand rule to x and y axes instead of a left handed system. Therefore, the scale factor comes out to be imaginary. Accordingly, we arranged the signs of the components of the **CD** matrix so to obtain real numbers for the scale.

Conducting the same procedure using the ASTAP solution, we can draw the X and Y axes in the image plane as,

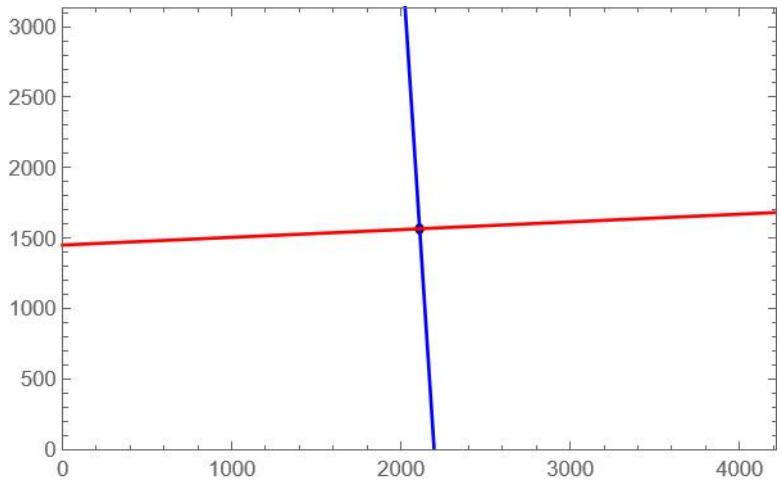

Figure 35: The X and Y axes in the digital image plane using ASTAP solution

Since Astrometry.net and ASTAP do not choose the same origin for the center of the image, we do not obtain any agreement between their outputs. As seen on Stellarium, the Right Ascension increases leftwards, and Declination increases upwards. To determine the correct coordinates, we need to consider the ξ-coordinate as running in the opposite direction than the x-coordinate on the sensor. Comparing our plot with Stellarium, the axes we obtained are parallel to the North-South and East-West directions in Right Ascension and Declination. We can also notice a similar tilt between the axes, and the information regarding the perpendicularity of the axes is given by ASTAP as 'CROTA1' and 'CROTA2' above.

Before going into direct and inverse problem details, we conducted the transformation from sensor coordinates (X, Y) to celestial coordinates (α, δ) according to the calculations given above. In order to obtain,

$$\alpha \pm \Delta\alpha$$

$$\delta \pm \Delta\delta$$

Plugging the values of the centroid coordinates found from the center-of-mass method into the functions given above, we obtain the RA/Dec as 14: 28 31.5157 and −20° 23 50.716 respectively. And $\Delta\alpha$, $\Delta\delta$ as 0.0073783 and 0.00147147 respectively. Considering the real data obtained by Stellarium, the RA/Dec of the asteroid Hygiea on April 14th are given as 14: 28 34.43 and −20° 23 55.8. Therefore, the absolute errors are calculated as 0.0121429 and 0.00141223 respectively.

The direct and inverse problem may be defined otherwise in books but for our case, we refer to the calculation of $(X, Y) \rightarrow (\alpha, \delta)$ as the **inverse problem** and $(\alpha, \delta) \rightarrow (X, Y)$ as the **direct problem**.

- The direct problem

The equations to implement the transition $(\alpha, \delta) \rightarrow (X, Y)$,

$$X = -\frac{\cos\delta \sin(\alpha - \alpha_c)}{\cos\delta_c \cos\delta \cos(\alpha - \alpha_c) + \sin\delta_c \sin\delta} \tag{67}$$

$$Y = -\frac{\sin\delta_c \cos\delta \cos(\alpha - \alpha_c) - \cos\delta_c \sin\delta}{\cos\delta_c \cos\delta \cos(\alpha - \alpha_c) + \sin\delta_c \sin\delta} \tag{68}$$

where (α_c, δ_c) are the coordinates of the origin of the Standard Coordinate Reference Frame.

In conclusion, we aim to calculate the RA/Dec of the spacecraft using the measured RA/Dec values of asteroids. The direct problem to locate an object of known celestial coordinates on the plate is,

$$(\alpha_c, \delta_c) \rightarrow (X, Y) \rightarrow (\xi, \eta) \rightarrow (x, y) \tag{69}$$

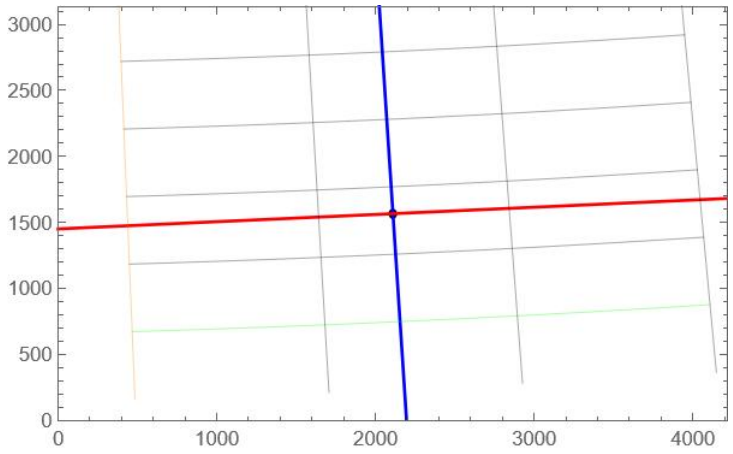

Figure 36: Centroid position viewed in sensor reference frame

After executing the transition $(\alpha_c, \delta_c) \rightarrow (X, Y)$ and obtaining the Standard Coordinates, using the matrix inversion, we can make the transitioning of $(X, Y) \rightarrow (\xi, \eta)$ where we obtain coordinates of the intermediate reference frame. Finally by the procedure of $(\xi, \eta) \rightarrow (x, y)$, we can have the final solution in sensor reference frame as shown in Fig. 36, we also imitated the lines of equal Right Ascension and Declination in the plate for convenience [38].

7.5 On-board optical navigation

Introducing the procedure for optical navigation conducted on the Jupyter Notebook provided by our supervisor Dr. Pinto and is publicly available at Ref. [43]. The elements of optical navigation was introduced by Vertregt in 1956, to determine the position and velocity of a spacecraft using optical measurements and observations made by on-board computers/navigators. A very recent paper by Brum and Schuindt (2022) gives a detailed description and a general formulation of optical navigation and its algorithms [44].

There are two networks in the sky, where the first one pointing to the North star, which is also the north pole of the celestial coordinate system, named equatorial coordinates. The other coordinate system is based on the plane of the orbit of the Earth which is called the ecliptic coordinate system (MJ2000). In Fig. 37 below, the ecliptic coordinates and equatorial coordinates are shown in orange and blue respectively.

Figure 37: Asteroid Hygiea on April 13th, 2037, shown in Stellarium

Accordingly shown in Fig. 38, the triangular plane AB̂S defines the reference plane in conversation. The constellation of Aries, the place where the ascending node of the Sun is located, is the origin of the ecliptic system and the RA/Dec system. The Sun intersects the celestial equator while passing through that node, from negative to positive declination.

The z axis is perpendicular to the plane of the orbit of the Earth where the point in Aries is the origin where we start counting the ecliptical longitudes. Defining the x, y and z axes, where the ecliptic longitude of the spacecraft, λ, is located around the Sun, pointing to Aries and going counterclockwise until it encounters with the projection of the spacecraft. The ecliptic longitude of the beacon asteroid, λ_P, the ecliptic latitudes of the spacecraft and the beacon asteroid are, β and β_P respectively. The latitudes represent the positive or negative inclination that the spacecraft and the beacond have from the ecliptic coordinate plane. Finally, the radius vector, r, of the spacecraft are associated to the rectangular coordinates as [45],

$$\mathrm{x} = r\cos\beta\cos\lambda \tag{70}$$

$$\mathrm{y} = \mathrm{r}\cos\beta\sin\lambda \tag{71}$$

$$\mathrm{z} = \mathrm{r}\sin\beta \tag{72}$$

An optical observation is sketched where point SC is the spacecraft itself, P is the asteroid that is observed and S is the Sun with the direction of ascending node of where the Sun is at the beginning of spring. Since the longitude λ_P, latitude β_P and the radius vector $\mathrm{r_P}$ of the asteroid with respect to Sun is known, using the ephemeris information, the spacecraft can measure the apparent longitude of the Sun, λ'_{Sun}, the apparent longitude of the asteroid, λ'_P and the apparent latitude of the Sun, β'_{Sun}.

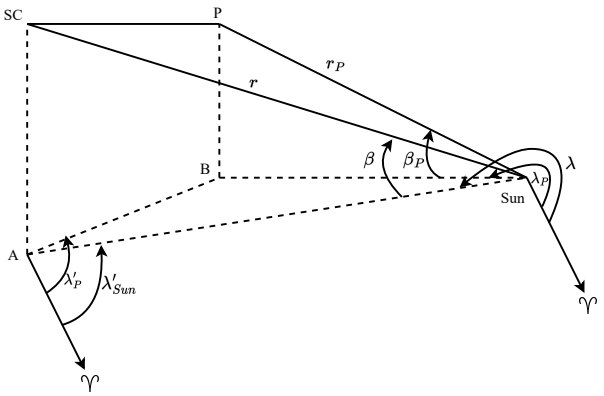

Figure 38: Optical observation sketch (Adapted from Ref. [45], sketched via diagrams.net)

In other words, the spacecraft is suppose to measure the asteroid's position in the ecliptic coordinates that originates from the spacecraft itself.

$$\overline{\mathrm{AS}} = \mathrm{r}\cos\beta\,, \qquad \overline{\mathrm{BS}} = \mathrm{r_P}\cos\beta_P \tag{73}$$

Using the triangle $\mathrm{A\hat{B}S}$ shown in Fig. 38,

$$\frac{\overline{\mathrm{AS}}}{\sin\mathrm{A\hat{B}S}} = \frac{\overline{\mathrm{BS}}}{\sin\mathrm{B\hat{A}S}} \tag{74}$$

$$\frac{\mathrm{r}\cos\beta}{\sin\mathrm{A\hat{B}S}} = \frac{\mathrm{r_P}\cos\beta_P}{\sin\mathrm{B\hat{A}S}} \tag{75}$$

Since,

$$\mathrm{A\hat{B}S} = 360^\circ + \lambda_P - \lambda'_P \tag{76}$$

$$\mathrm{B\hat{A}S} = \lambda'_P - \lambda'_{\mathrm{Sun}} \tag{77}$$

Therefore the distance between the spacecraft and the Sun, which correlates with the solution of the inverse problem for our case, can be found as,

$$\mathrm{r} = r_P \frac{\cos\beta_P \sin(\lambda_P - \lambda'_P)}{\cos\beta_{\mathrm{Sun}} \sin(\lambda'_P - \lambda'_{\mathrm{Sun}})} \tag{78}$$

$$\mathrm{r}\cos\beta\sin(\lambda'_{\mathrm{P}} - \lambda'_{\mathrm{Sun}}) = \mathrm{r_P}\cos\beta_{\mathrm{P}}\sin(360^\circ + \lambda_{\mathrm{P}} - \lambda'_{\mathrm{P}}) \tag{79}$$

Also considering,

$$\lambda = 180^\circ + \lambda'_{\mathrm{Sun}} \tag{80}$$

$$\beta'_P = \arcsin\frac{(\mathrm{z_P} - \mathrm{z})}{\mathrm{r_{VP}}} \tag{81}$$

where in Eq. 81, z_P and z are the position of the spacecraft and the asteroid in the z-axis, and r_{VP} is the spherical distance between them which the expression is available in Ref. [38] and obtained by using Mathematica. The coordinates of the spacecraft as in, r, λ and β at a certain time can be found. Therefore by using Eq. 70, 71 and 72 the rectangular coordinates of x, y and z can be calculated, hence, we can solve for λ'_P, also to compare it with the ephemeris file obtained from GMAT which is provided by Group 3. Also with enough measurements, $\dot{x}$, $\dot{y}$ and $\dot{z}$ can be estimated in time using Kalman Filtering [45].

7.5.1 Conversion from ecliptic coordinates to celestial coordinates

When an astronomical measurement is done by a telescope, people do not aim it according to the ecliptic coordinates but to the celestial coordinates. Since the sky rotates around the axis that goes through the North star, aiming according to celestial coordinates is more common. Therefore, we make the transitioning from ecliptic coordinates to celestial coordinates given by J. Meeus (1998) [46],

$$\tan\alpha = \frac{\sin\lambda\cos\epsilon - \tan\beta\sin\epsilon}{\cos\lambda} \tag{82}$$

$$\sin\delta = \sin\beta\cos\epsilon + \cos\beta\sin\epsilon\sin\lambda \tag{83}$$

where ϵ is *the obliquity of the ecliptic*, defined as:

$$\epsilon = 23^\circ.4457889$$

- Precession corrections (J2000 → to-date)

The direction of the rotational axis of the Earth experience a small change in time, called *precession*, which arises due to the gravitational attraction of the Sun and the unusual movement of the Moon on Earth's equatorial bulge. The northern celestial pole turns around the pole of the ecliptic in ~ 26000 years which corresponds to 50″ per year along the ecliptic. The plane of the ecliptic of the equator and the vernal equinox are the rising points of the two main coordinate systems mentioned in Sec. 7.5 above, the ecliptic and the equatorial coordinate systems. Therefore, even the coordinates of the fixed stars are changing due to precession which is the reason why star catalogs update the RA/Dec values in a certain time, such as 1900.0, 1950.0 and 2000.0 [46]. Thus, we apply the procedure of converting the RA/Dec values in J2000 reference frame to the corresponding values for ecliptic-to-date values. Considering an accurate method, let $(\mathrm{JD})_0$ and (JD) are the Julian Days for initial and final epoch,

$$T = \frac{(JD)_0 - 2451545.0}{36525} \quad , \quad t = \frac{(JD) - (JD)_0}{36525} \tag{84}$$

where t is the interval between the starting and final epoch and T is the intervals between J2000.0 and the starting epoch, in Julian centuries. For accurate reduction of positions from one equinox to other with the starting epoch as J2000.0, therefore $T = 0$ [46],

$$\eta = 47.0029t - 0.03302(t^2) + 0.000060(t^3)$$
$$\pi = 174.876384 - (869.8089/3600)t + (0.03536/3600)(t^2)$$
$$p = 5029.0966t + 1.11113(t^2) - 0.000006(t^3)$$

- Correction due to the aberration of light

The Earth's direction of motion changes as it orbits the Sun and stars move relative to the spacecraft which causes a difference in their position that is called aberration. Suppose an observer on the Earth moves with its moving frame, then the direction of approaching starlight observed from the Earth would be tilted relative to the angle observed in the Sun's frame. In 1725, James Bradley was investigating the position of the star Eltanin which moves in a circular orbit with an angular diameter of approximately 40.5″ and expecting a change in the apparent

position of the star due to parallax by observing it over a year. Bradley tried to observe a shift in the apparent position of a star in different months of a year which the star was expected to change its position following a circular shape. Yet, he observed an unexpected shift that leads him to discover stellar aberration [47][48].

Considering the geometric coordinates of the star as (λ, β),

$$\Delta\lambda = \frac{-\kappa \cos(\lambda_\odot - \lambda) + e\kappa \cos(\pi - \lambda)}{\cos\beta}$$

$$\Delta\beta = -\kappa \sin\beta \Big[\sin(\lambda_\odot - \lambda) - e \sin(\pi - \lambda)\Big]$$

where κ is the constant of aberration ($\kappa = 20.49552''$), $\lambda_\odot$ is the geometric ecliptic longitude of the Sun and e is the eccentricity of the orbit of the Earth.

Direct problem

Now, applying the procedures of the direct problem for the asteroid Hygiea on April, 13th 2037 at 03:18:17.00 UTC. We chose that exact date and time due to the mission simulated on GMAT by Group 3. Since we know the heliocentric position of the spacecraft, $\mathbf{r_{SC}} = (r_{SC}, \lambda_{SC}, \beta_{SC})$, and the heliocentric position of an asteroid, $\mathbf{r_P} = (r_P, \lambda_P, \beta_P)$ at time t, both expressed in ecliptic coordinates, for instance, in the J2000.0 system, we can obtain both the ecliptic coordinates $(\lambda_{P,SC}, \beta_{P,SC})$ and celestial coordinates $(\alpha_{P,SC}, \delta_{P,SC})$ of the asteroid in the reference frame of the observer. In order to generate ephemerides data in the Horizons System, there are some preparation steps that needs to be considered as shown in the Fig. 39 below.

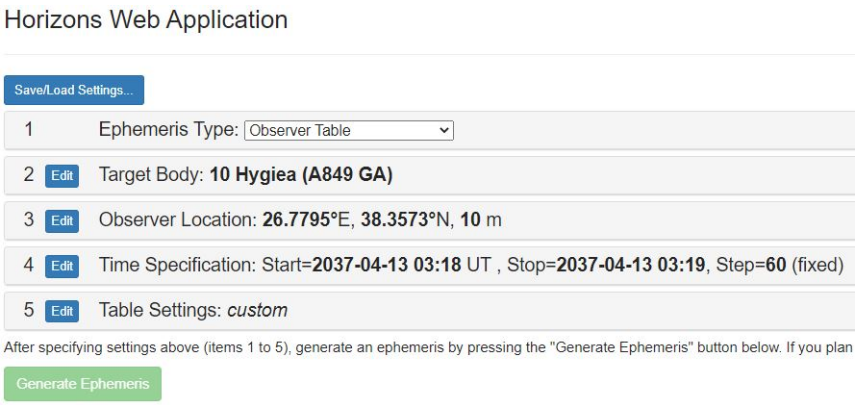

Figure 39: Horizons Web Application

Initially, the ephemeris type can be selected as one of the following: observer table, vector table, osculating orbital elements, small-body SPK file. 'Target Body' is the object that is going to be observed from the specified 'Observer Location'. Target body can be defined as a specific body or using TLEs. The observer location

can be specified by using geodetic or cylindrical coordinates, selecting a location either on Earth or a location in space, and again using TLEs. 'Time Specification' is the time span that we want to generate the ephemerides data. And, finally there is a whole bunch of observer table settings which one can customize according to their needs.

Test 1:

As a first example, we defined the Earth as a target body and selected the Sun as the coordinate center with a starting time on 2037-04-13 03:18 and the stopping time on 2037-04-13 03:19 with a step size of 60 equal intervals and generated the following positions of X, Y and Z.

$$\begin{aligned} \mathrm{X} &= -1.380426541938914 \times 10^{8} \\ \mathrm{Y} &= -5.867896628300961 \times 10^{7} \\ \mathrm{Z} &= 6.116780017375946 \times 10^{3} \end{aligned}$$

Using the Eqs. 70, 71 and 72 given above we calculate the heliocentric ecliptic coordinates λ, β and r as

$$\begin{aligned} \mathrm{r} &= \sqrt{\mathrm{x}^2 + \mathrm{y}^2 + \mathrm{z}^2} = 1.49997 \times 10^{8} \\ \lambda &= \arctan\left(\frac{\mathrm{y}}{\mathrm{x}}\right) = 23.0293 \\ \beta &= \arcsin\left(\frac{\mathrm{z}}{\mathrm{r}}\right) = 0.00233649 \end{aligned}$$

And, the Horizons gives the λ and β on 2037-04-13 03:18:17.00 in J2000.0 as 23.5421159° and -0.0021704° respectively. Double checking using Stellarium, it gives the ecliptic longitude in J2000.0 and to-date as 23.0257° and 23.5422° respectively. And, the ecliptic latitude as -0.0045° and -0.0022°. Comparing the results with the Stellarium data, we obtain 0.0156347% and 48.078% of an error, which the uncertainty in latitude needs to be reconsidered during the procedure but the main reason should be the fact that Horizons equip the ecliptic-of-date coordinates, although we are using the Cartesian heliocentric ecliptic coordinates in the J2000 reference frame. The difference between the data generated by JPL/Horizons ans Stellarium happens due to the difference between their initial assumptions. Keeping in mind that a 10^{-3° of uncertainty yields to $3^{"}$.

Fig. 40 below, shows the topocentric ecliptic longitude and the heliocentric ecliptic longitude in blue and orange colored curves respectively where the blue dot represents the Earth with the direction of the first point of Aries and the ecliptic coordinates coinciding with the $x-$axis.

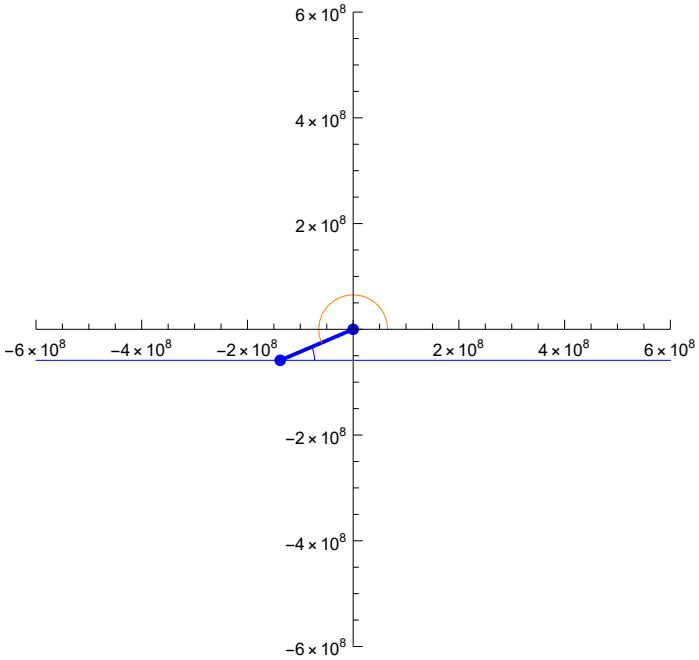

Figure 40: The topocentric and heliocentric longitudes

Conducting the precession correction procedure using Eq. 84 and utilizing the following website provided by NASA [https://heasarc.gsfc.nasa.gov/cgi-bin/Tools/xTime/xTime.pl] to convert the ISO 8601 date and time, 2037-04-13 03:18:17 in this case, to Julian Date which results to 2465161.63769676. Finally, correcting λ and β from J2000.0 to on-date, we obtain 23.5501° and 0.00463922°. Comparing with the real data given in Stellarium, the accuracy in longitude is quite satisfactory while the latitude still has an unreasonably large error.

Test 2:

Applying the same procedure for the asteroid Hygiea.

• **Hygiea - Heliocentric polar and Cartesian ecliptic coordinates:** 10 Hygiea chosen as the target body and the Sun as the coordinate center. Horizons generates,

$$\lambda = 98.4268043^\circ \quad \beta = 0.2711006^\circ$$

$$\begin{aligned} \mathrm{X} &= -7.445637672833471 \times 10^7 \\ \mathrm{Y} &= 5.024188718664897 \times 10^8 \\ \mathrm{Z} &= 2.401538910083234 \times 10^6 \end{aligned}$$

Using these values for the calculations of λ, β and r yield to,

$$r = \sqrt{x^2 + y^2 + z^2} = 5.07912 \times 10^8$$
$$\lambda = \arctan\left(\frac{y}{x}\right) = -81.5704$$
$$\beta = \arcsin\left(\frac{z}{r}\right) = 0.270907$$

Considering the Eq. 80 above,

$$\lambda = 180^\circ + \lambda'_{\text{Sun}} = 98.4296 \tag{85}$$

Comparing the data produced by Horizons, our calculations of the heliocentric ecliptic longitude and latitude result to a pretty accurate measurement. Fig. 41 shows the asteroid Hygiea as seen from the Sun where the orange arc represents the heliocentric ecliptic longitude, λ, of Hygiea.

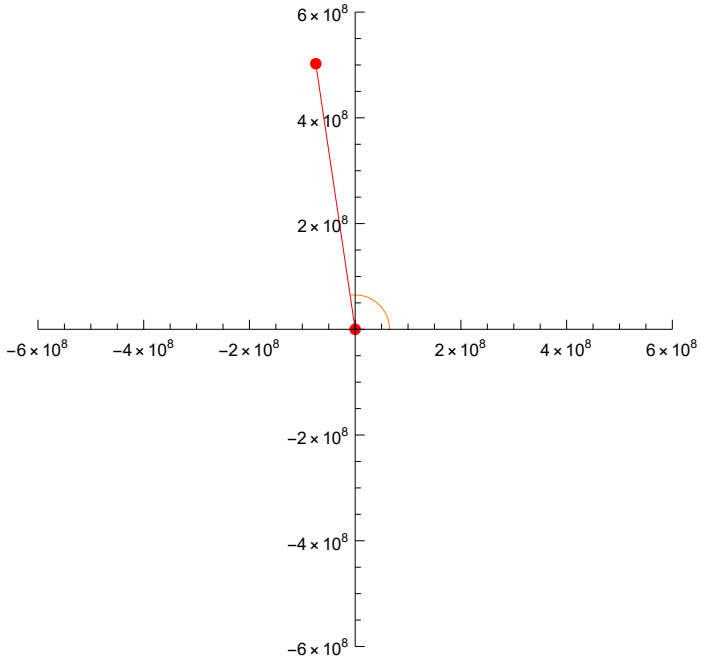

Figure 41: Asteroid Hygiea as seen from the Sun

• **Hygiea - Heliocentric polar ecliptic coordinates ($\lambda_{\text{SC, ast}}$, $\beta_{\text{SC, ast}}$) as seen from the spacecraft (in this case, the Earth observer):** The observer location is chosen as where the asteroid detection was made in the first place, Urla Iskele, 26.7795° E, 38.3573° N, and with a 10 meters of altitude. In this case, we need to determine λ'_P in Eq. 79 above by defining the function, $F_P(\lambda'_P)$ as,

$$F_P(\lambda'_P) = r\cos\beta\sin(\lambda'_P - \lambda'_{\text{Sun}}) - r_P\cos\beta_P\sin(360^\circ + \lambda_P - \lambda'_P) \tag{86}$$

Solving for the ecliptic longitude using Mathematica,

$$F_P(\lambda'_P) = 0$$

We obtain the ecliptic longitude, λ'_P, as 83.5346° and the ecliptic latitude, β'_P, as 0.268574° which Horizons generated as 84.0458431° and 0.2475506° respectively. In the below Fig. 42, the asteroid Hygiea is represented with the black dot on the $(-x, y)$ portion of the graph as seen from the observer located in the given coordinates which is also represented with the black dot on the $(-x, -y)$ portion of the graph. The orange curve indicates the heliocentric ecliptic longitude of the Earth observer and the black curve indicates the observer-centric ecliptic longitude, λ'_P, of Hygiea. Finally, the blue arc is the ecliptic longitude of the Sun as seen from the Earth observer.

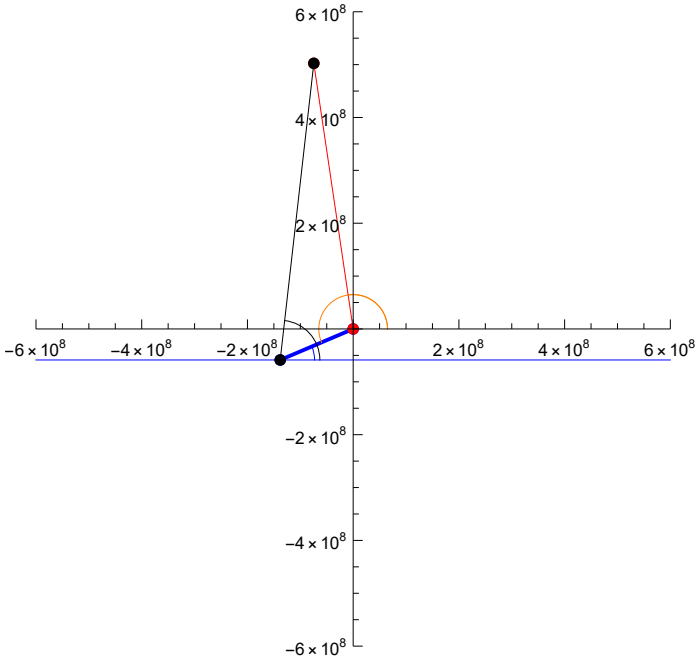

Figure 42: Asteroid Hygiea as seen from the Earth observer

Finally, converting the ecliptic coordinates to celestial coordinates, we obtain $\alpha = 05\text{h}\,31\text{m}\,46.6481\text{s}$ as the right ascension and $\delta = 23^\circ\,32'\,58.7623''$ as the declination.

Test 3:

• **Vesta - Heliocentric polar and Cartesian ecliptic coordinates:** This time, considering the asteroid Vesta as seen from the Sun, the polar and Cartesian coordinates produced by Horizons are,

$$\lambda = 342.3659374^\circ \quad \beta = -6.1139607^\circ$$

$$\begin{aligned} \mathrm{X} &= 3.309611563339154 \times 10^8 \\ \mathrm{Y} &= -1.051812605930014 \times 10^8 \\ \mathrm{Z} &= -3.719972554952545 \times 10^7 \end{aligned}$$

Our calculated values for the ecliptic longitude and latitude are 342.369° and -6.11419° respectively, which are almost the same with the real data. Fig. 43 displays the asteroid Vesta with a blue dot on the $(\mathrm{x}, -\mathrm{y})$ portion of the graph where the blue dot at the origin represents the Sun. The arc shown in orange indicates the heliocentric longitude of the asteroid Vesta and the blue arc is the ecliptic longitude of the Sun.

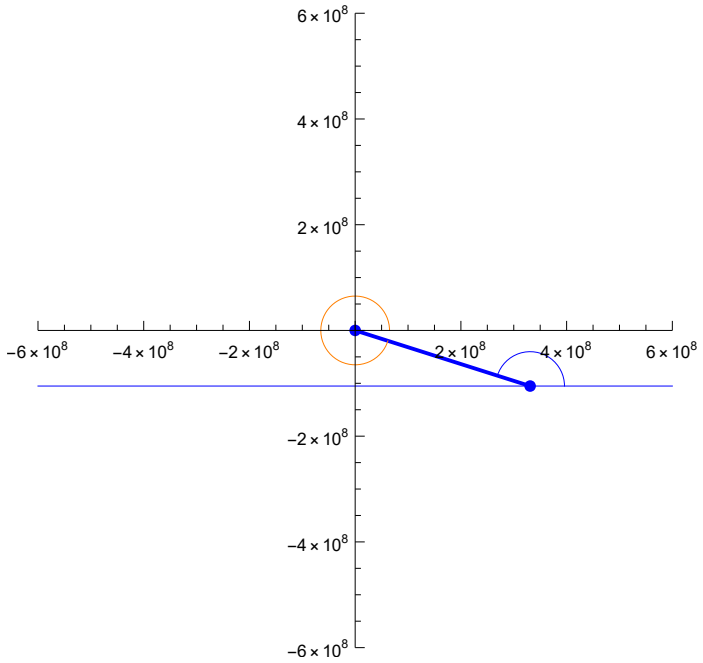

Figure 43: Asteroid Vesta as seen from the Sun

• **Hygiea - Polar and Cartesian ecliptic coordinates as seen from Vesta:** As another example, we assume the asteroid Vesta as our spacecraft which is targeted to the asteroid Hygiea. Entering the target body in Horizons as Hygiea and the observer location as the asteroid Vesta, we obtain the following polar and Cartesian coordinates,

$$\lambda = 123.7072557^\circ \quad \beta = 3.1031669^\circ$$

$$\begin{aligned} \mathrm{X} &= -4.054175172300563 \times 10^8 \\ \mathrm{Y} &= 6.076001883280268 \times 10^8 \\ \mathrm{Z} &= 3.960127406336501 \times 10^7 \end{aligned}$$

The transcendental equation given above as Eq. 78 is now solved again by Mathematica to find the spacecraft-centric longitude and latitude of the asteroid Hygiea which was calculated as $\lambda'_P = 122.851^\circ$. The spacecraft-centric ecliptic latitude can be calculated using $360 - \lambda_{SC}$ and $180 + \lambda_P$ which yield to 342.369° and 95.4296° respectively. Therefore the spacecraft-centric ecliptic latitude is calculated as $\beta'_P = 3.10329^\circ$. We have a decent accuracy considering the real data obtained from Horizons. Although, one reason for slight uncertainties, which is 0.692163% for the longitude in this case, could be the distance, almost 1 billion kilometers, between the asteroids.

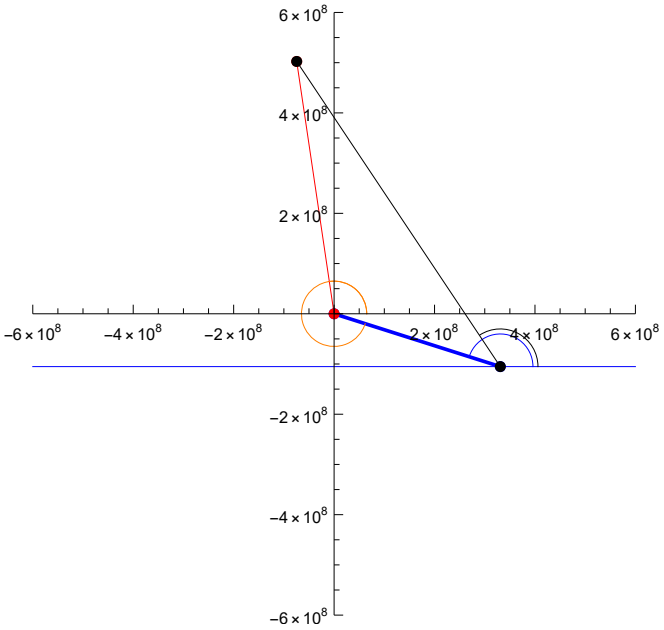

Figure 44: Asteroid Hygiea as seen from the asteroid Vesta

In the Fig. 44 above, the black arc represents the spacecraft-centric ecliptic longitude of the asteroid Hygiea where the black dot on the $(x, -y)$ portion of the graph represent Vesta and the other one is Hygiea itself. The blue angle is the spacecraft-centric ecliptic longitude of the Sun, λ'_{Sun}, and finally, the orange arc represents the heliocentric ecliptic longitude of the spacecraft, Vesta. Converting what we have to celestial coordinates result in $\alpha = 08\text{h}\,23\text{m}\,37.5964\text{s}$ and $\delta = 22^\circ\,32'\,27.635''$, although, there is almost a 4 minutes difference between the right ascension values and 12 minutes of difference between the declination values given in Horizons.

Test 4:

• **Hygiea as seen from our solar-sail spacecraft:** In this test, we use the ephemerides file corresponding to the Pluto mission that Group 3 designs. The ephemerides file produced by GMAT provides the Cartesian ecliptic coordinates in the reference frame of MJ2000 of the solar-sail spacecraft calculated for some arbitrary intervals of time. Therefore, we now use the spacecraft itself as the observer instead of Vesta, the Sun or an Earth-based observer. The Cartesian coordinates on April, 13th, 03:19:10 are given by GMAT are the following,

$$\text{X} = 4.112280615952520 \times 10^9$$
$$\text{Y} = -3.280906185651609 \times 10^9$$
$$\text{Z} = -8.434386640596744 \times 10^8$$

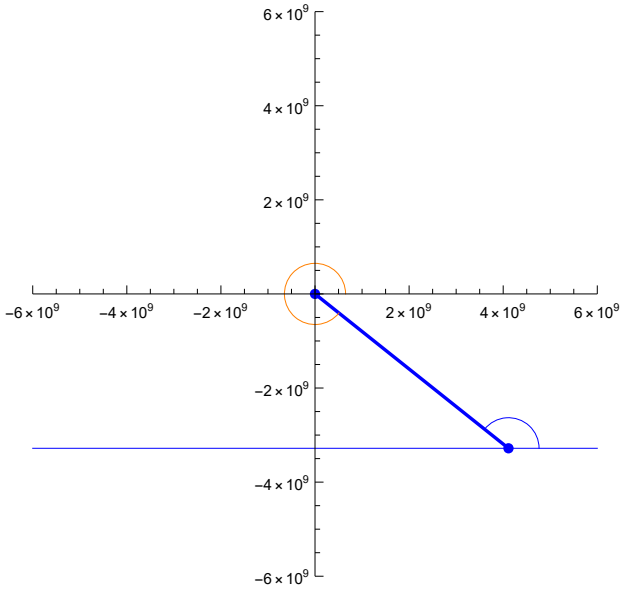

Figure 45: The Sun as seen from the solar-sail spacecraft

Using the Cartesian ecliptic coordinates, the heliocentric ecliptic longitude and latitude of the spacecraft in the J200 system are calculated as, $\lambda_{SC} = 321.416°$ and $\beta_{SC} = -9.10857°$ where the orange arc in the Fig. 45 above represents the heliocentric ecliptic longitude of the spacecraft. Moving onto Horizons again, the heliocentric ecliptic Cartesian coordinates of the asteroid Hygiea on April, 13th, 03:19:10 are given as,

$$X = -7.445718023934111 \times 10^7$$
$$Y = 5.024186977030435 \times 10^8$$
$$Z = 2.401483651916653 \times 10^6$$

Again, the heliocentric ecliptic longitude and latitude are calculated as

$\lambda_P = 98.4297°$ and $\beta_P = 0.270904°$ respectively. The Fig. 46 below shows the asteroid Hygiea orbiting around the Sun and the spacecraft is out of the plotting range since it is arriving to pluto, 6 billion kilometers away from the Sun.

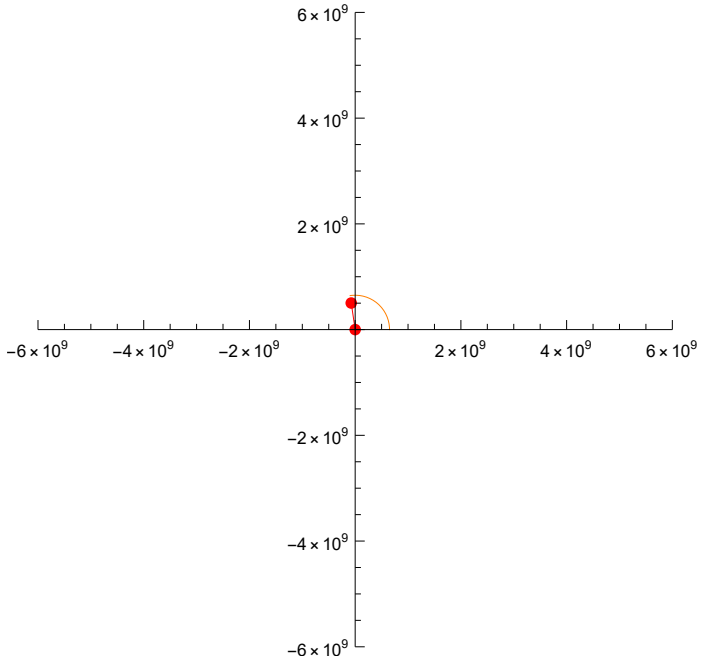

Figure 46: Asteroid Hygiea and the Sun

Finally, the spacecraft-centric ecliptic longitude and latitude of the asteroid are calculated as $\lambda'_P = 145.468°$ and $\beta'_P = 8.52486°$. Transitioning to the celestial coordinates of the asteroid Hygiea as seen from the spacecraft yields to $\alpha =$ 14h 20m 32.2679s and $\delta = 04° 59' 26.0412''$. Fig. 47 shows the asteroid Hygiea, the black dot on top, as seen from the spacecraft, the black dot at the bottom, with the Sun at the center.

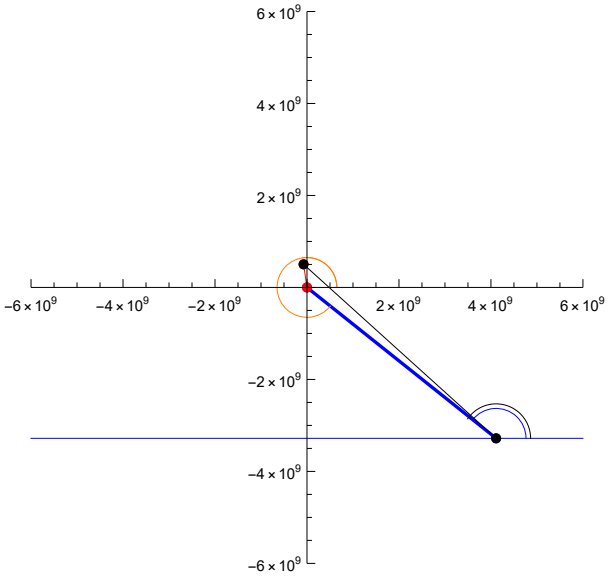

Figure 47: Asteroid Hygiea as seen from the solar-sail spacecraft

• **Vesta as seen from our solar-sail spacecraft:** Same procedure above is applied to the asteroid Vesta. The heliocentric ecliptic latitude and longitude are calculated as $\lambda_{\mathrm{P}} = 162.37°$ and $\beta_{\mathrm{P}} = -6.1142°$ respectively. The spacecraft-centric ecliptic longitude and latitude are calculated as $\lambda'_{\mathrm{P}} = 139.975°$ and $\beta'_{\mathrm{P}} = 9.27304°$.

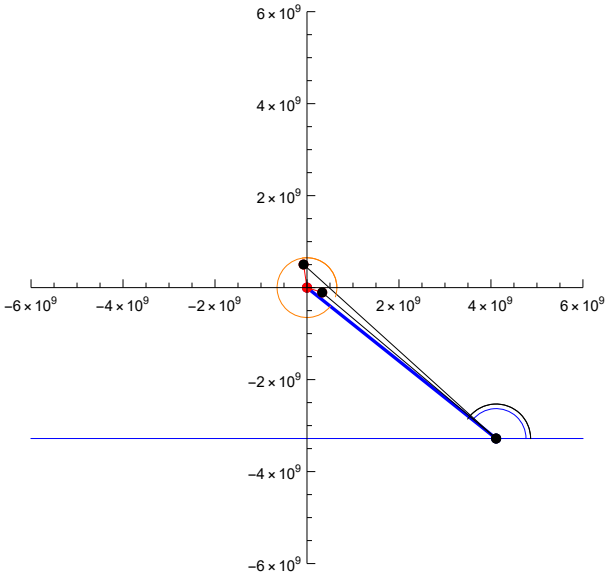

Figure 48: Asteroid Vesta and Hygiea as seen from the solar-sail spacecraft

Transitioning to the celestial coordinates of the asteroid Vesta as seen from the spacecraft yields to $\alpha = 9\text{h}\,42\text{m}\,14.486\text{s}$ and $\delta = 23^\circ\,35'\,53.2621''$. Fig. 48 shows the asteroid Vesta, the black dot on the right-hand side of the Sun, the asteroid Hygiea, the black dot on the left-hand side of the Sun, as seen from the spacecraft, the black dot on the bottom, with the Sun at the center.

• **Pluto as seen from our solar-sail spacecraft:** Since arrival to Pluto is only months ahead at this point, we can also execute the same calculations to Pluto for visual understanding purposes. The Cartesian coordinates of Pluto on April, 13th, 03:19:10 obtained from Horizons,

$$\begin{aligned} \text{X} &= 4.375997733464246 \times 10^9 \\ \text{Y} &= -3.593855513601380 \times 10^9 \\ \text{Z} &= -8.811619203715653 \times 10^8 \end{aligned}$$

In the Fig. 49 above, we can clearly see how our spacecraft is close to Pluto.

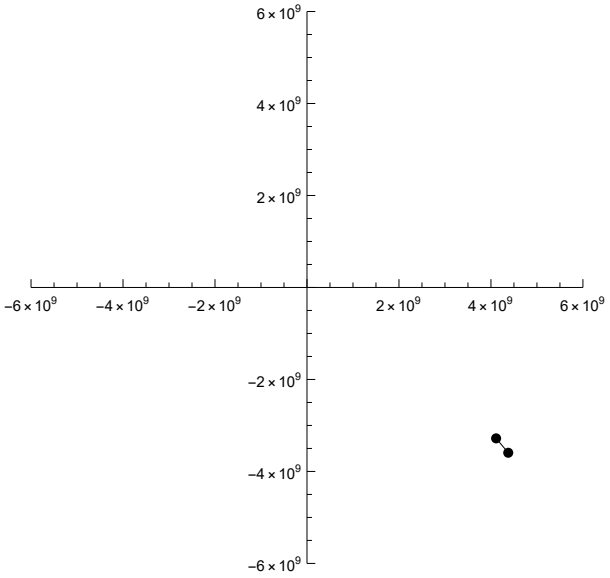

Figure 49: Pluto as seen from the solar-sail spacecraft

The LOS from the spacecraft into the inner solar system is very similar with the LOS of Pluto going into the same direction. The spacecraft-centric ecliptic longitude and latitude of Pluto are calculated as $\lambda'_{\text{P}} = 130.12^\circ$ and $\beta'_{\text{P}} = -5.26647^\circ$. Finally, calculating the RA/Dec of Pluto as seen from the spacecraft, we obtain $\alpha = 08\text{h}\,44\text{m}\,27.917\text{s}$ and $\delta = 22^\circ\,46'\,28.6657''$.

Plotting all of the celestial bodies in conversation and the spacecraft in the same graph to make the process conceivable and for the sake of seeing the bigger picture in Fig. 50

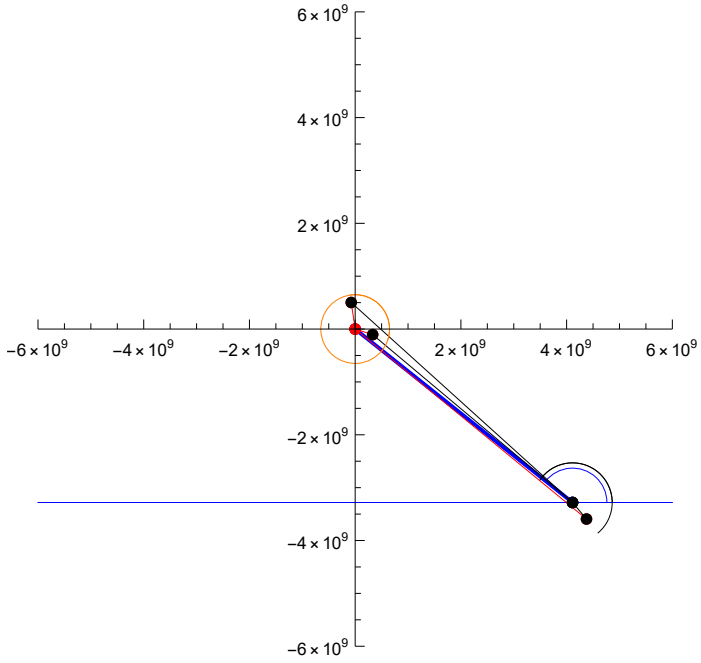

Figure 50: Asteroid Vesta and Hygiea, the Sun, Pluto and the solar-sail spacecraft

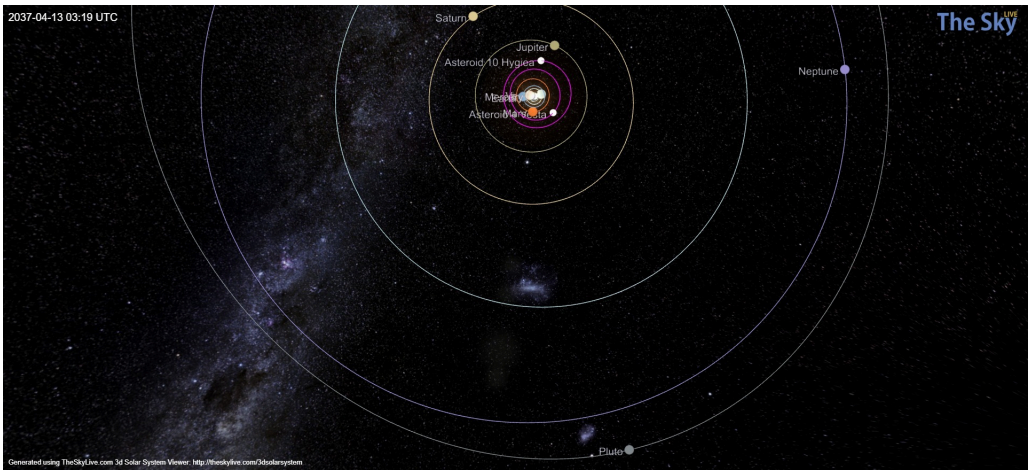

Figure 51: TheSkyLive view of the solar system with Hygiea and Vesta in the LOS of Pluto

2. Inverse problem

Since we have determined the RA/Dec of the asteroid from the observations, we can now obtain the Cartesian ecliptic coordinates of the spacecraft/observer. We also make the assumption that the observer measures the apparent longitude and the apparent latitude of the Sun, $\lambda'_{\rm Sun}$ and $\beta'_{\rm Sun}$, and the apparent longitude of the asteroid, λ'_P.

$$r = r_P \frac{\cos\beta_P}{\cos\beta'_S} \frac{\sin(360^\circ + \lambda_P - \lambda'_P)}{\sin(\lambda'_P - \lambda'_S)} = r_P \frac{\cos\beta_P}{\cos\beta'_S} \frac{\sin(\lambda_P - \lambda'_P)}{\sin(\lambda'_P - \lambda'_S)} \tag{87}$$

$$\lambda = 180^\circ + \lambda'_S \tag{88}$$

$$-\beta = -\beta'_S \tag{89}$$

7.5.2 Conversion from celestial coordinates to ecliptic coordinates

As is obvious from the Direct case, the determination of the centroid coordinates shall provide those quantities in terms of Right Ascension and Declination. On the other hand, the determination of the position of the spacecraft shown above requires knowledge of the centroid of the beacon asteroid in terms of ecliptic coordinates. Therefore the first step is to state the equations needed for such transformations,

$$\tan\lambda = \frac{\sin\alpha\cos\epsilon + \tan\delta\sin\epsilon}{\cos\alpha} \tag{90}$$

$$\tan\beta = \sin\delta\cos\epsilon - \cos\delta\sin\epsilon\sin\alpha \tag{91}$$

Using the Eqs. 78, 79, 80 and 81 provided by A. Roy

Test 1:

• **Ecliptic coordinates of an Earth-based observer:** Considering the again the case of observing Hygiea from our solar-sail spacecraft,

$$\lambda'_P = 139.975^\circ\ , \quad \beta'_P = 9.27304^\circ$$

$$\alpha'_P = 8.74109\ \text{h}\ , \quad \delta'_P = -22.7746^\circ$$

Utilizing above coordinates we obtain the ecliptic longitude and latitude for the inverse case as, $\lambda_{\rm INV} = 141.439^\circ$ and $\beta_{\rm INV} = -4.52259^\circ$ respectively.

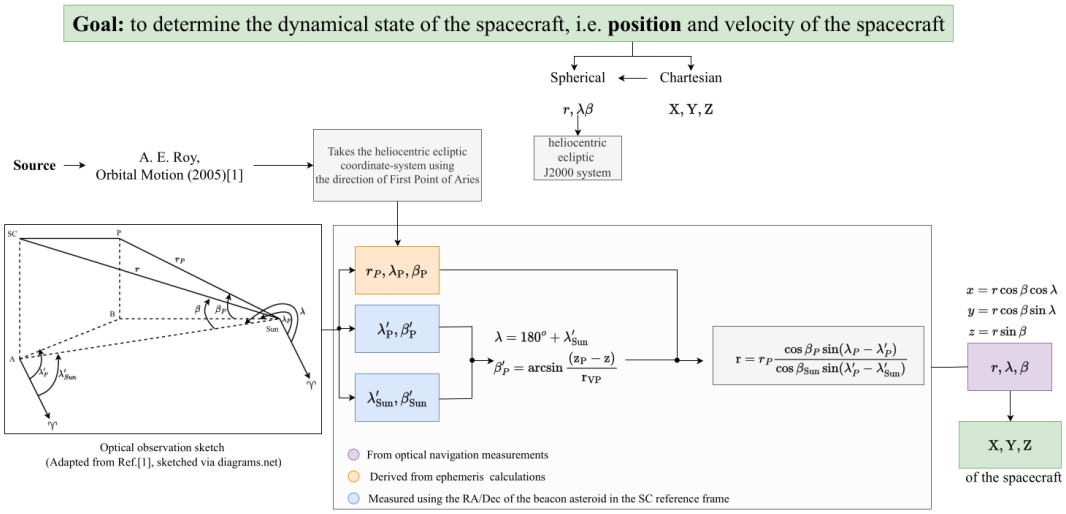

Figure 52: Map of optical navigation

8 Kalman Filter

A Kalman Filter can be used in any situation when you have ambiguous information about a dynamic system and want to make an educated bet about what the system will do next. Even if muddy reality gets in the way of the smooth motion you predicted, the Kalman Filter is usually quite good at figuring out what happened. It can also take advantage of links between bizarre phenomena that you might not have considered utilizing and are also convenient for systems that regularly change. They have the benefit of being memory-light and extremely quick, making them ideal for real-time challenges and embedded devices [49].

Kalman Filtering method is also called Linear Quadratic Estimation. The algorithm uses conceptual and series of calculations measurements spotted over time and contains statistical noises and inaccuracies. Kalman Filter produces approximates of unknown values that tend to be more accurate by estimating the joint probability distribution which is the associated probability dispersion on all possible measurements. The method can be used when it is hard to measure something directly so with the results of indirect measurement, accurate results can be reached eventually. Another way to do that can be the calculation of the results obtained from different measurement methods, results can be classified and specified from the intersection set [49].

Introducing the block diagram of the system and the concept of state observer, K, shown in Fig. 53:

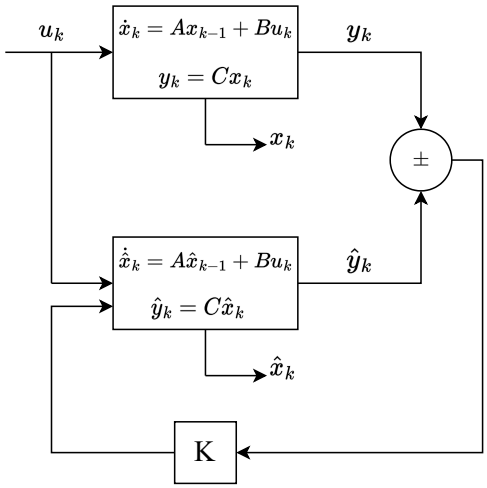

Figure 53: Kalman Filter block diagram (Adapted from Ref. [50], sketched via diagrams.net)

The input of the system is given as u_k and the output is y_k, where we assume to have a single state for simplicity, also noise sources are neglected. The Kalman Filters take place in combining the measurements y_k and $\hat{x}_k$ and making a prediction to find the optimal estimate for the output. The state observer, K, allows us to classify and eliminate the error in the previous calculation.

The effect of Kalman Filtering can be visualized using probability density functions. The estimated position can be anywhere around $\hat{x}_{k-1}$ at the initial time step, $k-1$. In other words, the position will be most likely around the mean of the distribution. In time step k, let's assume that the uncertainty in the estimate increased which causes a larger variance. The measurement y_k is another source of information on the distance in the x direction, where the true position can be anywhere around the mean. Therefore, the prediction and measurement yield an estimation given by their multiplication. Finally, the mean of that function indicates the optimal current estimate for the position. Eventually, the combination of indirect measurements and estimations results in a value that can be reached with better accuracy with a high number of measurements [50].

Now, considering a solar-sail lost in deep space which is in need of navigation with a simplest given state vector of $\vec{x}_k = \begin{bmatrix} \vec{p} \\ \vec{v} \end{bmatrix}$, indicating the position and velocity. Note that the state is simply a list of numbers describing a system's underlying setup; it may be anything. It may be data on the amount of fluid in a tank, the temperature of a car engine, or any number of other things you need to keep track

of. Both position and velocity are assumed to be random and Gaussian distributed in the Kalman Filter. Each variable has a mean value, μ, which is the center of the random distribution, and a variance, σ^2, which is the degree of uncertainty [51],

Position and velocity are uncorrelated, which means that the state of one variable has no bearing on the state of the other. Something more intriguing can be seen in such case that the two variables of position and velocity are intertwined. The possibility of viewing a specific position is determined by the velocity. This type of situation could exist if we're estimating a new location-based on an old one. This relationship is crucial to keep track of since it provides us with more information, one measurement hints at what the others might be. And that is the purpose of the Kalman Filter: to extract as much information as possible from our questionable measurements. In our case, Kalman Filtering is a perfect tool for updating the estimated measurements over some time to converge to the solution. Obviously, enough measurements are needed in order to utilize it.

9 Results and Discussion

Since we have introduced ourselves into the field of autonomous navigation during our literature research, we are now aware of the state of the art of this timely technology. Our supervisor Dr. Fabrizio Pinto was kind enough to reach out to people at NASA who are specialized in this field, to transfer the latest achievements and status which guided us through. As stated in Sec. 3, the DS1 mission is the first and last to successfully utilize Auto-Nav technology, therefore it is quite contemporary and up-to-date. The most recent mission planned to travel through a targeted asteroid is "Near-Earth Asteroid Scout (NEA Scout)" which is going to be launched as a part of the Artemis 1 mission planned due on March 2022. NEA Scout is a solar-sail propelled CubeSat class spacecraft, designed to target the asteroid 2020 GE (which may be changed due to the date of launch), and aims to explore the asteroid with robotic devices [52], which is going to be using ground-based navigation, not Auto-Nav. Thanks to Dr. Shyam Bhaskaran, we have found out the software package "MONTE" which was designed to be a general-purpose astrodynamic library under Python environment, to be used in deep-space navigation, and is going to be used for navigation of the NEA Scout mission. MONTE was initially used for navigating the spacecraft of Mars Science Laboratory in 2012. It is developed by JPL where they used a FORTRAN-based software called "DPTRAJ/ODP" back in the 1990s for the DS1 mission. And, recent developments of MONTE was importing the library into Python environment to further improve and develop astrodynamic features of MONTE [53]. Yet, there are still no missions announced to associate both Auto-Nav and solar-sailing technologies together.

The Fig. 54 below displays a flow diagram for the whole procedure of the project.

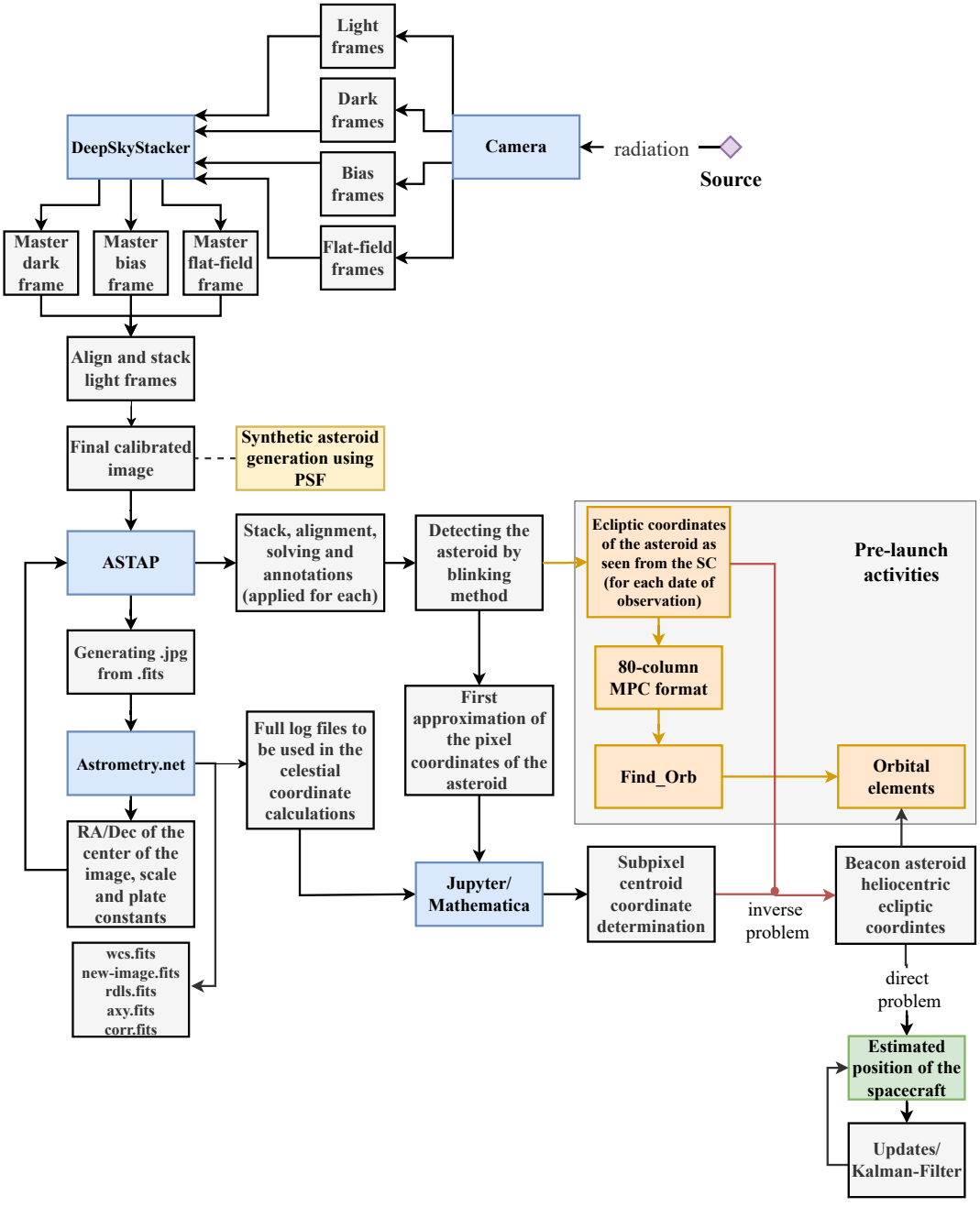

Figure 54: General workflow block diagram, sketched via diagrams.net

10 Conclusion

In this project, we introduced a detailed procedure for the application of optical navigation. The procedure includes the following: Stellar field observation with a camera produces calibration frames and raw frames for DeepSkyStacker to generate the master frames, align and stack the light frames to obtain a calibrated image at the end. Feeding that calibrated image to Astrometry.net generates log files including the RA/Dec of the center of the image, scale and plate constant for the given stellar field which are used in ASTAP to stack and solve the image, aiming to detect the asteroid by blinking technique using three observations of the same stellar field. The first approximation of the pixel coordinates of the detected asteroid then becomes a sub-frame in the Jupyter Notebook, coded in Mathematica, to be isolated out of the whole image frame that allows us to determine its centroid coordinate. Then, either the synthetically generated or the physically observed asteroid centroid pixel coordinates are now converted into ecliptic coordinates as seen by the spacecraft which are going to be utilized in the determination of the heliocentric ecliptic coordinates of the beacon asteroid. Finally, the estimated position of the spacecraft can be obtained by conducting the given direct problem. With enough measurements, the position would converge to true value utilizing Kalman Filtering as the updating method.

We have also discussed how the Auto-Nav technology can be beneficial in terms of what current and future space mission needs. The hustling of the DSN is starting to become an obstacle to expanding missions, meaning that it will eventually be unable to acknowledge the requests and meet the demands. Especially, the deep-space/interplanetary missions need to evolve into onboard navigation, rather than ground-based navigation in order to both allow near-Earth missions to appropriately use DSN. And, to be able to operate by itself since they cannot rely on ground-based navigation systems due to their distance from the Earth. The groundbreaking solution in increasing the traveling distance has been, of course, the solar-sail technology, which makes it possible for the spacecraft to explore through deep-space without the need of conventional propulsion systems. We have introduced some of the cutting-edge technologies and missions throughout the paper, such as Deep Space 1, IKAROS, Voyager, and LightSail missions. However, there is not any mission that has combined Auto-Nav and solar-sail technologies, which is what we aim to prove the concept of.

References

[1] Y. Akan, D. L. Demirbağ, H. Karaaliler, I. Macit, "Autonomous optical and inertial navigation of solar-sail propelled CubeSat class spacecraft during targeting missions to asteroids and minor moons", Preliminary final thesis report (FENG-498), Faculty of Engineering, Izmir University of Economics (IEU) in Izmir, Türkiye. Presented at the 1st Workshop on Open Source Space Mission Design Tools hosted online on 1 March 2022 by the IEU Department of Aerospace Engineering. https://youtu.be/01s-HVKDHGE

[2] D. Wang, M. Li, X. Huang, X. Zhang, Spacecraft Autonomous Navigation Technologies Based on Multi-source Information Fusion Space Science and Technologies Series Editor: Peijian Ye, Springer International Publishing, Beijing.
URLhttp://www.springer.com/series/16385

[3] P. T. Chen, J. L. Speyer, D. S. Bayard, W. A. Majid, Autonomous navigation using X-ray pulsars and multirate processing, Journal of Guidance, Control, and Dynamics 40 (9) (2017) 2237–2249. doi:10.2514/1.G002705.

[4] W. contributors, Radio beacon — Wikipedia, the free encyclopedia, [Online; accessed 21-December-2021] (2021).
URLhttps://en.wikipedia.org/w/index.php?title=Radio_beacon&oldid=1037300686

[5] Y. Akan, D. L. Demirbağ, H. Karaaliler, I. Macit, Response of a capacitive accelerometer. Free and dampened harmonic oscillators, unpublished AE-420 project reports (Instructor: Fabrizio Pinto), Department of Aerospace Engineering, Izmir University of Economics (2021).

[6] S. Berrabah, Y. Baudoin, GPS data correction using encoders and inertial navigation system (INS) sensors, Using Robots in Hazardous Environments (2011) 269–282 doi:10.1533/9780857090201.2.269.

[7] W. contributors, Inertial navigation system — Wikipedia, the free encyclopedia, [Online; accessed 21-December-2021].
URLhttps://en.wikipedia.org/w/index.php?title=Inertial_navigation_system&oldid=1052239500

[8] M. A. Paluszek, J. B. Mueller, M. G. Littman, Optical navigation system, AIAA Infotech at Aerospace 2010 (April) (2010). doi:10.2514/6.2010-3462.

[9] M. W. D. Kenneth R. Spring, Thomas J. Fellers, Introduction to charge-coupled devices (CCDs)
URLhttps://www.microscopyu.com/digital-imaging/introduction-to-charge-coupled-devices-ccds

[10] The MathWorks Inc., What is camera calibration?, (2021).
URLhttps://www.mathworks.com/help/vision/ug/camera-calibration.html

[11] N. B. Stastny, D. K. Geller, Autonomous optical navigation at jupiter: A linear covariance analysis, Journal of Spacecraft and Rockets 45 (2) (2008) 290–298. doi:10.2514/1.28451.

[12] G. M. Levine, A method of orbital navigation using optical sightings to unknown landmarks, AIAA Journal 4 (11) (1966) 1928–1931. doi:10.2514/3.3820.

[13] S. Li, R. Lu, L. Zhang, Y. Peng, Image processing algorithms for deep-space autonomous optical navigation, Journal of Navigation 66 (4) (2013) 605–623. doi:10.1017/S0373463313000131.

[14] L. A. Soderblom, T. L. Becker, G. Bennett, D. C. Boice, D. T. Britt, R. H. Brown, B. J. Buratti, C. Isbell, B. Giese, T. Hare, M. D. Hicks, E. Howington-Kraus, R. L. Kirk, M. Lee, R. M. Nelson, J. Oberst, T. C. Owen, M. D. Rayman, B. R. Sandel, S. A. Stern, N. Thomas, R. V. Yelle, Observations of comet 19P/Borrelly by the miniature integrated camera and spectrometer aboard Deep Space 1, Science 296 (5570) (2002) 1087–1091. doi:10.1126/science.1069527.

[15] D. G. Hoag, The history of Apollo onboard guidance, navigation, and control, Journal of Guidance, Control, and Dynamics 6 (1) (1983) 4–13. doi:10.2514/3.19795.

[16] R. Park (Website manager), NASA/JPL, What does SSD do?
URLhttps://ssd.jpl.nasa.gov/about/

[17] Fabrizio Pinto, CCDs in the Mechanics Lab-A Competitive Alternative? (Part I), The Physics Teacher, 33 (7) 6. doi:https://doi.org/10.1119/1.2344260.
URLhttps://aapt.scitation.org/doi/10.1119/1.2344260

[18] C. Kittel, Berkeley Physics Course, 1973. doi:10.1002/9783527664986.app8.

[19] A. R. Davoyan, J. N. Munday, N. Tabiryan, G. A. Swartzlander, L. Johnson, Photonic materials for interstellar solar sailing, Optica 8 (5) (2021) 722. doi:10.1364/optica.417007.

[20] NASA Science, Solar system exploration, 4 vesta (2019). URLhttps://solarsystem.nasa.gov/asteroids-comets-and-meteors/asteroids/4-vesta/in-depth/

[21] N. T. Redd, Vesta: Facts about the brightest asteroid (2018). URLhttps://www.space.com/12097-vesta-asteroid-facts-solar-system.html

[22] H. Karaaliler, Asteroid Detection by Blinking Technique and Discovery of Pluto, unpublished AE-451 project report (Instructor: Fabrizio Pinto), Department of Aerospace Engineering, Izmir University of Economics (2020).

[23] H. Karaaliler, Stellar Photometry from DSLR Images, unpublished AE-451 project report (Instructor: Fabrizio Pinto), Department of Aerospace Engineering, Izmir University of Economics (2020).

[24] M. Richmond, The HertzsprungRrussell (HR) diagram. URLhttp://spiff.rit.edu/classes/phys230/lectures/hr/hr.html

[25] N. Strobel, Color and temperature. URLhttps://www.astronomynotes.com/starprop/s5.htm#:~:text=The%20%60%60B%2DV%20color%20index,the%20green%2Dyellow%20band%20through.

[26] Fabrizio Pinto, Synthetic centroid and CCD frame generation (2022, August 23). https://doi.org/10.5281/zenodo.701654. See also https://osf.io/gdt3a/

[27] Fabrizio Pinto, 10 Hygiea (2022-04-13, 14, and 15) (2022, August 18). https://osf.io/pu5g9/

[28] S. Ozkan, E. Tola, M. Soysal, Performance of star centroiding methods under near-real sensor artifact simulation, RAST 2015 - Proceedings of 7th International Conference on Recent Advances in Space Technologies (2015) 615–619doi:10.1109/RAST.2015.7208417.

[29] D. Ford, The Observer's Guide to Planetary Motion (2014). doi:10.1007/978-1-4939-0629-1. URLhttp://link.springer.com/10.1007/978-1-4939-0629-1

[30] M. Bolte, Optical and Infrared Imaging and Astrometry 1–22.
URLhttp://ircamera.as.arizona.edu/Astr_518/imaging3.pdf

[31] D. Jacobsen, CCD Image Calibration Page, Image (Rochester, N.Y.) (2014) 1–4.

[32] W. contributors, Bias frame — Wikipedia, the free encyclopedia, [Online; accessed 29-June-2022]
URLhttps://en.wikipedia.org/wiki/Bias_frame

[33] W. contributors, Flat-field correction — Wikipedia, the free encyclopedia, [Online; accessed 29-June-2022]
URLhttps://en.wikipedia.org/wiki/Flat-field_correction

[34] R. Suszyński, K. Wawryn, Stars' centroid determination using PSF-fitting method, Metrology and Measurement Systems 22 (4) (2015) 547–558. doi:10.1515/mms-2015-0047.

[35] O. Montenbruck, T. Pfleger, Astronomy on the personal computer, 4th Edition, Vol. 38, Springer Berlin Heidelberg, 2001. doi:10.5860/choice.38-3875.

[36] J. Tatum, Standard coordinates and plate constants (2022).
URLhttps://phys.libretexts.org/Bookshelves/Astronomy_Cosmology/Celestial_Mechanics_(Tatum)/11%3A_Photographic_Astrometry/11.02%3A_Standard_Coordinates_and_Plate_Constants#:~:text=The%20constants%20a%E2%80%93f%20are,coordinates%20can%20therefore%20be%20calculated

[37] B. E. W. Paul R. Wolf, Bon A. Dewitt, Elements of photogrammetry with applications in GIS, 4th edition (2014).
URLhttps://www.accessengineeringlibrary.com/content/book/9780071761123/back-matter/appendix2

[38] Fabrizio Pinto, Introduction to asteroid detection, centroid characterization, and orbit determination (2022, August 18). https://doi.org/10.5281/zenodo.7006675. See also https://osf.io/pwmtr/ and observational data at https://osf.io/pu5g9/

[39] C. Fosu, B. Eissfeller, G. W. Hein, Determination of centroid of ccd star images.

[40] H. Wang, E. Xu, Z. Li, J. Li, T. Qin, Gaussian Analytic Centroiding method of star image of star tracker, Advances in Space Research 56 (10) (2015) 2196–2205. doi:10.1016/j.asr.2015.08.027.

[41] W. contributors, Center of mass — Wikipedia, the free encyclopedia URLhttps://en.wikipedia.org/w/index.php?title=Center_of_mass&oldid=1086253732

[42] R. Buchheim, 2007, The Sky is Your Laboratory: Advanced Astronomy Projects for Amateurs doi:10.1007/978-0-387-73995-3.

[43] Fabrizio Pinto, Elements of optical navigation (2022, August 29). https://doi.org/10.5281/zenodo.7032245. See also https://osf.io/5u9qe/.

[44] A. G. V. de Brum, C. M. Schuindt, A Proposal of Optical Navigation for Deep Space Mission ASTER to Explore NEA 2001-SN263, Journal of Aerospace Technology and Management 14 (2022) 1–14. doi:10.1590/jatm.v14.1246.

[45] A. Roy, Orbital Motion, Fourth Edition, Orbital Motion, Fourth Edition (2004). doi:10.1201/9781420056884.

[46] J. Meeus, Astronomical Algorithms, 2nd Edition, Willmann-Bell, Inc., Richmond, Virginia, 1998.

[47] S. Hurley, Explaining Science, Stellar aberration (2019). URLhttps://explainingscience.org/2019/05/28/stellar-aberration/

[48] H. Karaaliler, Aberration Phenomena and Interstellar Navigation, unpublished PHYS-314 project report (Instructor: Fabrizio Pinto), Department of Aerospace Engineering, Izmir University of Economics (2010).

[49] M. Ulusoy, The MathWorks Inc., Kalman filter virtual lab (2022). URLhttps://www.mathworks.com/matlabcentral/fileexchange/105525-kalman-filter-virtual-lab

[50] M. Ulusoy, The MathWorks Inc., Insight into kalman filtering-probability distribution fnc (2022). URLhttps://www.mathworks.com/matlabcentral/fileexchange/69003-insight-into-kalman-filtering-probability-distribution-fnc?s_eid=PSM_15028

[51] Bzarg, How a kalman filter works, in pictures (2015). URLhttps://www.bzarg.com/p/how-a-kalman-filter-works-in-pictures/

[52] NASA, Page Editor: Erin Mahoney, NASA Official: Brian Dunbar, Advanced Exploration Systems (2021).
URLhttps://www.nasa.gov/content/nea-scout

[53] Evans, S., Taber, W., Drain, T., Smith, J., Wu, H. C., Guevara, M., Sunseri, R., & Evans, J., (2018). MONTE: the next generation of mission design and navigation software., CEAS Space Journal, 10(1), 79–86. https://doi.org/10.1007/s12567-017-0171-7.